DEPARTMENT OF PHYSICS
UNIVERSITY OF JYVÄSKYLÄ
RESEARCH REPORT No. 4/2006

DETECTION OF CHARGED KAONS USING THE DECAY TOPOLOGY IN ALICE TPC

BY
MARIANA BONDILA

Academic Dissertation
for the Degree of
Doctor of Philosophy

To be presented, by permission of the
Faculty of Mathematics and Natural Sciences
of the University of Jyväskylä,
for public examination in Auditorium FYS-1 of the
University of Jyväskylä on May 22, 2006
at 14 o'clock

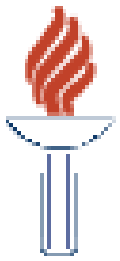

Jyväskylä, Finland
May 2006

ISBN 978-951-39-3169-8

URN:ISBN:978-951-39-3169-8

Eight Gluons for the Universe
To set her gauge.
Six Quarks for Humankind
Search for the truth.
One Plasma with superstrength
One Plasma to bind them.
Through Dark Energy
One Plasma to quench them.
And from the Big Bang
One Plasma To shape them all.

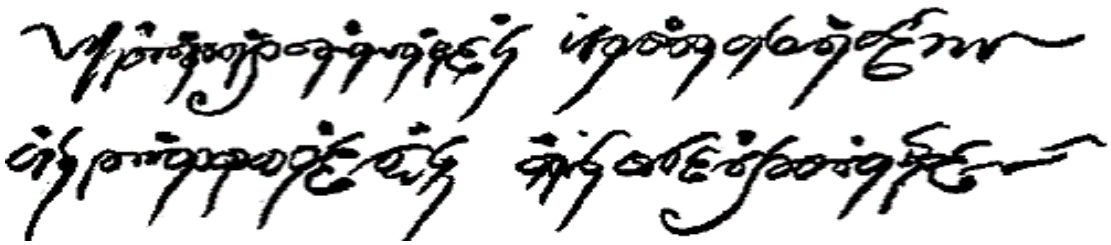

One plasma, verse in the style of J.R.R. Tolkien
T.D. Lee

To my family

Contents

Outline

In the present work, I focus on strange particle physics. The goal is to study the capabilities of ALICE, the dedicated heavy-ion experiment at the LHC, of measuring on a track-by-track basis charged kaons in a high multiplicity environment. In particular, I address the question of whether the identification range we achieve allows us to use charged kaons, which are the dominant carriers of strange quarks, to get insight into the properties of the deconfined matter.

The thesis is organized as follows:

- The physics framework is outlined in Chapter 1 where I introduce the strangeness production measurements with special emphasis on strange particles as probes to characterize the dynamics of the matter formed in heavy ion collisions. Considering that the production of strangeness through partonic interactions, mainly $gg \rightarrow s\bar{s}$, is expected to dominate over that by hadronic scatterings and given that at LHC energies the initial gluon density is expected to be higher than in the lower-energy heavy ion collisions, strange particles are expected to be sensitive to the dynamics of the plasma phase.

- The ALICE experiment is presented in Chapter 2. The tracking detectors and in particular the main tracker, the Time Projection Chamber (TPC), are described in more detail as these are the main detectors used for the measurement of charged kaons using the decay topology. The basic principles and the functionality of the off-line framework are very briefly described in Section 2.5.

- The charged track reconstruction is presented in Chapter 3. First, I discuss the tracking requirements, the general track reconstruction strategy and the Kalman filter as method of choice for the track reconstruction. Then, in Section 3.4.2 I focus on the track reconstruction algorithm in the TPC. In Section 3.5, special attention is given to the track reconstruction performance. I focus on the behaviour of track reconstruction parameters like track quality, efficiency and momentum and angular resolutions, that are relevant for reconstruction of decay topologies.

- The strategy and the specific algorithms I developed for charged kaon identification using the decay topology are described in Chapter 4. The main selection parameters are discussed briefly in Section 4.2.

- The evaluation of the performance of the algorithm and estimations for the p_T range over which statistically significant numbers of kaons can be reconstructed on a track-by-track basis during the first year of data taking are presented in Chapter 5. The strategy I adopted for realistic simulations of the signal and of the background is introduced in Section 5.1.2. I present the results of a systematic study of the reconstruction efficiency and precision, and of the background which might be expected, for different charged particles densities with different tracking detectors configurations, in Section 5.1.3. The estimates for the p_T range are given in Section 5.2.3.

- A brief summary of the general picture emerging from this study concludes the thesis.

Chapter 1

Motivation

Understanding the physical world does not mean only establishing its fundamental constituents; it means, mostly, understanding how these constituents interact and bring to existence the entire variety of phenomena and physical objects composing the Universe. The primary motivation for colliding heavy ions is to investigate the dynamics of strong interaction in matter at extremely high temperatures and densities, which are thought to have existed in a few-μs old Universe. It is belived that under such extreme conditions, the symmetries of quantum chromodynamics (QCD) will reveal themselves: color will be deconfined and chiral symmetry restored. The deconfined state of quarks and gluons is commonly referred to as the quark-gluon plasma (QGP).

The phase transition from hadronic to deconfined matter at high temperatures is the only phase transition among those predicted by the Standard Model that can be reached with laboratory experiments. First evidence of its existence stemmed from a series of experimental observations at the Super Proton Synchrotron (SPS) at CERN [1, 2]. The experiments with Pb–Pb collisions at a center-of-mass energy per nucleon pair, $\sqrt{s_{NN}} = 17.3$ GeV, at the SPS showed a significant strangeness enhancement [3, 4, 5, 6], a suppression in the production of the J/Ψ which grows with the centrality of the collision [7, 8, 9], and an enhancement of low-mass dilepton production below the ρ^0 resonance, presumably caused by an in-medium modification of the ρ-meson spectral function in the dense matter [10, 11, 12]. Further experimental investigations at the Relativistic Heavy Ion Collider (RHIC), at about one order of magnitude higher center-of-mass collision energy, confirmed the SPS results and added to this picture new observables, such as the particle flavor dependence of the elliptic flow (see Appendix A.1 for definition) which appears to derive from a universal partonic flow pattern [13, 14, 15, 16], the high-p_T particle suppression [17, 18, 19, 20, 21] and medium-induced modifications of jets [22, 23, 24, 25, 26, 27, 28]. The dynamical evolution of the matter created at RHIC appears to be hydrodynamically driven, implying that the produced medium is strongly coupled [29, 30, 31, 32, 33, 34, 35].

In the context of saturation physics[1] [38], the dynamics of the interaction in the

[1]The basic idea is that the growth of parton distribution functions at small x, observed in deep inelatic scatterings at HERA [36], should become limited by density effects. At some point, gluon

forward region ($\eta \sim 3$) in d–Au collisions at RHIC appears to indicate the onset of saturation in the gluon structure function [39, 40, 41]. For a detailed evaluation of the results obtained by the experiments at RHIC, see [42, 43, 44, 39].

The properties of the de-confined matter are, however, not well known. The Large Hadron Collider (LHC), with Pb beams collided at a center of mass energy per nucleon pair, $\sqrt{s_{NN}} = 5.5$ TeV, may allow a significative qualitative improvement with respect to the previous programmes. The nearly 30-fold increase in the center-of-mass energy over RHIC will presumably lead to a much higher initial density and to an even faster equilibration. Higher energy density and larger lifetime [45, 46] will enhance the role of the QGP phase over final state hadronic interactions and widens the time window available to probe it experimentally. Furthermore, the cross section for hard processes will increase considerably. High momentum jets and hadrons with transverse momenta of 100 GeV/c and more will become available [47]; their large transverse momentum ensures that the medium effects are calculable in a perturbative QCD (pQCD) approach. Heavy quark production is also copious at the LHC [48]. The $b\bar{b}$ bound states and the Υ family, will be produced with high statistics for the first time in heavy ion collisions (see, for instance [49]). In addition, the energy increase at LHC will make accessible the regime where small x effects such as gluon density saturation and the nonlinear Q^2 evolution of the parton distributions will be prominent[2]. For reviews of the heavy ion physics potential at LHC we refer to Refs. [49, 50, 51, 52, 47, 53].

Detailed theoretical studies of the properties of this new state of matter show that one of the distinctive features of the QGP is that it is rich in gluons [54] and strangeness [3, 55, 56, 57]. The enhanced production of strange particles is one of the predicted signals for the formation of a plasma of quarks and gluons in heavy-ion collisions.

1.1 What is interesting about strangeness production?

The argument for studying strange particle production in heavy-ion collisions as evidence of quark-gluon plasma formation is very simple and was first suggested in 1982 by Rafelski and Müller [3]. The idea relies on the difference in production rates of strange particles in a hadron gas compared to strange quarks in a QGP. The argu-

fusion must balance the growth caused by gluon splitting. The low-x saturation physics is formulated in the theory of Color Glass Condensate (CGC) which is based on first principles from QCD and should give the appropriate description of the initial conditions of the collisions. A validation or invalidation of the theory is an important step as the theory deals with some of the unsolved problems of QCD, such as the computation of the total cross section for hadronic scattering at asymptotic energy [37].

[2]Note that in the long term, for the study of the small x effect there will be a dedicated e–A experimental program (eRHIC) at RHIC.

ments for a strangeness enhancement in a QGP phase are basically twofold[3]. First, due to chiral symmetry restoration, the threshold for strangeness production in the QGP phase is considerably smaller than the one in ordinary hadrons [3]. Second, the timescale at which strangeness abundance saturates[4] (equilibration time) in a QGP is considerably smaller than that for a hadronic gas. In the latter case, the strangeness equilibration time exceeds the reaction time of the heavy-ion collisions.

The first argument is fairly easy to see. Since the net strangeness content of the colliding nuclei in the initial state is zero, all strange particles in the final state, e.g. kaons and Λs, have to be generated in the collision. As strangeness is a conserved quantity, each particle containing a strange quark must be accompanied by a corresponding particle containing an anti-strange quark. In a hadron gas, the energy threshold for strange particle prodction is high. The creation of a Λ for instance is predominantly through the reaction $\pi + N \rightarrow K + \Lambda$, with a threshold energy requirement of ~ 530 MeV (that of a $\bar{\Lambda}$ requires ~ 1420 MeV). Moreover, multi-strange particle creation not only needs a large amount of energy but is also a multi-step reaction as first a singly strange particle and then a multi-strange one must be created. In a deconfined matter, the associated production of a strange-antistrange quark pair can proceed by the fusion of two gluons or two light quarks and thus, due to chiral symmetry restoration the threshold for the production of a $s\bar{s}$ pair is only about twice the strange quark bare mass ~ 300 MeV.[5] The production of the pairs will be enhanced even more because of the high density of gluons. Given that, for large energies ($\sqrt{s} > 0.6$ GeV [61]), the quark annihilation $q\bar{q} \rightarrow s\bar{s}$ has a much smaller cross section and the expected gluon richness increases $gg \rightarrow s\bar{s}$ significantly, the gluon fusion is the dominant process ($85\% - 90\%$ of the total rate) capable to populate, within the reaction time, the strange quark phase space [3, 55, 62], up to, and even above the chemical equilibrium value in the QGP phase [62]; the rate of the light $q\bar{q} \rightarrow s\bar{s}$ alone would not suffice for strangeness equilibration in QGP [63]. It should also be noted that the cross section for $gg \rightarrow s\bar{s}$ is much larger than the cross section for $s\bar{s}$ creation in a hadronic gas. Thus, not only is creation energetically favourable but the probability is larger in the case of QGP formation. The greatest enhancement in yields is expected to be for multi-strange baryons which can be produced by statistical combination of strange (and nonstrange) quarks [58]. The strangeness relative production rate in equilibrium compared to $u\bar{u}$ and $d\bar{d}$ depends on temperature and baryochemical potential, but also on the quark masses [64, 65, 66].

For the second argument, a more elaborate and detailed calculation via rate equations has to be considered (see [56, 67] and references therein). Here, we only note that

[3] An additional argument for strangeness enhancement, relevant for central nuclear collisions at SPS energies where the baryon number density is large, is that in a baryon rich environment when the quark chemical potential is greater than the mass of the strange quark, a strange antibaryon, compared to nonstrange antibaryons, enhancement is expected [58].

[4] The strangeness abundance cannot grow forever; at some point in time, annihilation reactions will deplete the population of the already produced strange quarks. See the discussions in [3, 59].

[5] Present estimates for the current strange quark mass ranges from $m_s = 60 - 170$ MeV [60].

the equilibration time depends strongly on the temperature in the plasma. For $T = 300$ MeV, a time of about 3 fm/c seems to be enough to fully equilibrate strangeness production in the plasma, while at a temperature of $T = 160$ MeV, something like 20 fm/c is needed. Note that these estimates assume that the QGP is thermally equilibrated and the nonperturbative effects are not taken into account. Attempts to include nonperturbative effects find that the equilibration timescale is shifted upwards (above 10 fm/c) close to the dynamical scale of heavy-ion collisions (see [68] and discussions in [69]). For the case of the production of strange particles in a hadronic gas, one has to rely on detailed numerical computations which include all known resonances and their cross sections, some poorly known if known at all, in hot matter (see [65]). In a purely hadronic scenario, it has been shown that the strangeness equilibration time for (anti)hyperons at finite baryochemical potential exceeds the reaction time of the heavy-ion collisions by at least one order of magnitude [65]. For detailed discussions see for instance Refs. [69, 67].

1.1.1 Strangeness enhancement

Experimental data are available for a large range of energies, collision centralities, system sizes and various particle species, see e.g. [2, 70, 71, 72, 73]. At all center-of-mass energies a strangeness enhancement is observed in A–A as compared to p–A and pp. Two of the representative experimental results are shown in Fig. 1.1 and Fig. 1.2.

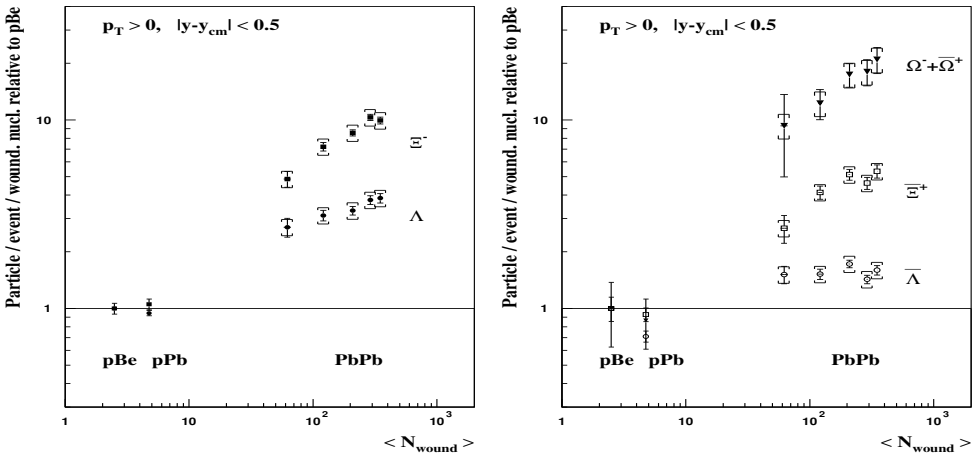

Figure 1.1: Strange baryon production in Pb–Pb per wounded nucleon, normalized to the ratio from p–Be, as a function of the number of wounded nucleons, i.e. the number of nucleons taking part in primary collisions, as measured by NA57 at the CERN-SPS at $\sqrt{s}$=158 A$\cdot$ GeV/c [4].

In Fig. 1.1 one can see that the production of strange and multi-strange baryons increases up to 10 times and more (up to 20 times for the Ω) in central Pb–Pb collisions in comparison to p–Be, where the QGP is not expected. As predicted, the

enhancement ε, defined as the ratio of the number of strange baryons per wounded or participant nucleon produced in Pb–Pb collisions to the the number of strange baryons per wounded or participant nucleon produced in p–Be collisions, is increasing with the strangeness content of the particle: $\varepsilon_\Lambda < \varepsilon_\Xi < \varepsilon_\Omega$.

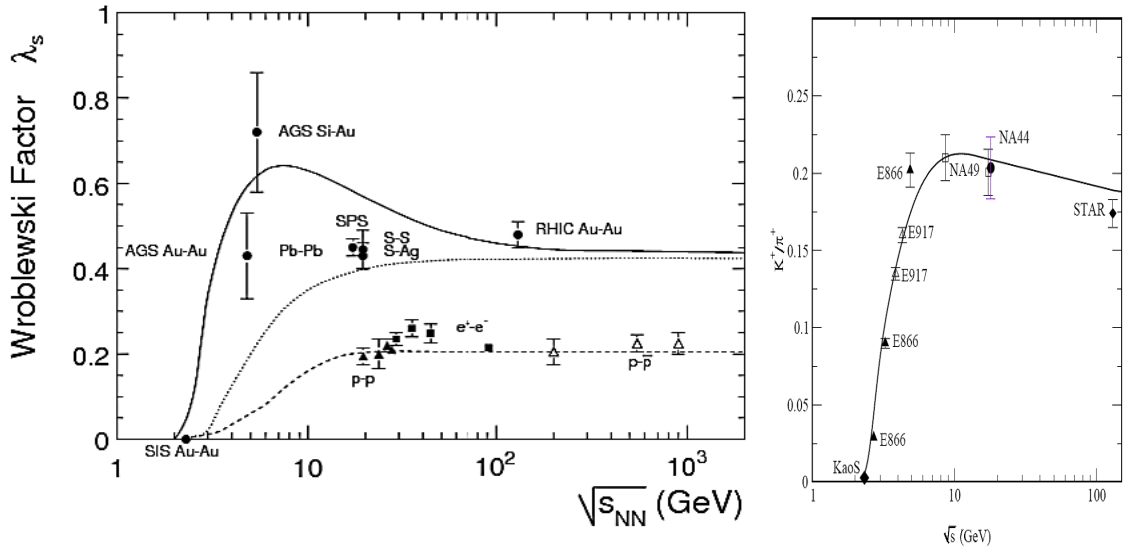

Figure 1.2: The Wróblewski factor (left) and K^+/π^+ ratio (right) as a function of $\sqrt{s}$. The solid lines in the left and right panels exhibit the trends given by the statistical model calculations using the T, μ_B parameters along the unified chemical freeze-out curve (the mean energy per particle drops below 1 GeV at all collision energies) [74]. The dotted line in the left panel shows the calculations with the same T as for the solid line but with $\mu_B = 0$. This demonstrate that the maximum is caused by finite baryo-chemical potential. The dashed line has been calculated with the statistical model in a canonical formulation using a correlation volume with a radius of 1.2 fm, keeping $\mu_B = 0$ and taking the energy dependence of T as determined previously. Note that the exact conservation of quantum numbers, i.e. the canonical approach, is known to reduce severely the phase space available for particle production [75].

Figure 1.2 (left panel) summarizes the results for the strangeness content of the system at equilibrium, defined here by the Wróblewski ratio [76], $\lambda_s \equiv 2\langle s\bar{s}\rangle/\langle u\bar{u}\rangle + \langle d\bar{d}\rangle$, of newly produced strange quark pairs to newly created non-strange quark pairs as a function of the collision energy for e^+e^-, pp, $p\overline{p}$ and heavy-ion collisions. The triangles for elementary pp reactions are consistent with 'color string snapping' process which yields strangeness pairs with about 22% abundance of the light quark pairs, and nearly independent of $\sqrt{s}$. In heavy ion collisions (circles) there are two important differences in the behavior of λ_s compared to elementary collisions. Firstly, the strangeness content is higher by a factor of two. Secondly, the relative strangeness content reaches a clear and well pronounced maximum at around 30 A·GeV lab energy. The appearance

of the maximum in heavy ion collisions can be traced to the specific dependence of μ_B and T on the beam energy (more details can be found in [77]). These differences in the behavior of λ_s seem to indicate that a new strangeness production process occurs, which could well be the thermal production of strangeness in QGP.

For high $\sqrt{s}$, λ_s reaches a saturation value of ≈ 0.43 in the hadron-gas approach [77], reflecting the situation at $T = 170$ MeV and a vanishing baryon chemical potential, $\mu_B = 0$. For an ideal QGP a value of λ_s of about 1 is expected at infinite temperature. However, recent lattice calculations demonstrate that due to the quark-mass difference of s and u, d in the QGP phase, λ_s also reaches ≈ 0.45 when approaching the critical temperature T_c with $\mu_B = 0$ [78]. This is a first hint as to why the observed strangeness reflects the value corresponding to an equilibrated hadron gas, since it is equal to that for a QGP at T_c. Ideally, one would like to pin down the $s/d, u$ ratio at the hadronization point before the hadronic decays take place. This is difficult because secondary decays increase the number of u, d quarks significantly while the number of s quarks remains almost unaffected. Alternatively, one can study how the behavior of the Wróblewski ratio is reflected in specific particle yields. Of particular interest is the K yield which at high energies is responsible for almost 80% of the total strangeness production.

The energy dependence of the K^+/π^+ ratio measured at midrapidity is shown in the right panel of Fig. 1.2. The measured K^+/π^+ ratio [79, 80] is a very rapidly rising function of $\sqrt{s}$. It reaches a maximum and gradually decreases up to RHIC energy [81]. In microscopic transport models [82, 83] the increase of the kaon yield with the collision energy is qualitatively expected as a result of a change in the production mechanism from associated production of K^+ with strange baryons ($N + N \rightarrow N + K + \Lambda$, $\Delta + N \rightarrow N + K + \Lambda$) to direct K^+K^- pair production ($N + N \rightarrow N + N + K^+ + K^-$). However, the transport models do not provide a quantitative explanation of the experimental data in the whole energy range [84] and the drop can only be reproduced using a statistical model which introduces a strangeness phase space occupancy parameter γ_s of about 0.75 [85] or by a generalized statistical hadronization model which describes not only strange but also light quarks off chemical equilibrium at hadronization [86]. The strangeness phase space occupancy, γ_s, measures the deviation from a completely chemically equilibrated hadron gas; the production of particles containing n valence strange quarks is suppressed by a factor ${\gamma_s}^n$.

1.1.2 Strangeness and chiral symmetry restoration

Lattice QCD: numerical indications for chiral symmetry restoration

Based on the asymptotic freedom, QCD predicts a phase transition [87] at high temperatures, around $T_c = 173 \pm 8$ MeV,[6] as seen numerically on lattice gauge calculations [89, 90, 91, 92].

[6] New calculations suggest $T_c = 186 \pm 3$ MeV [88].

For the phase transition of pure gluon matter at finite temperature, lattice simulations demonstrate that at the critical temperature for deconfinement, the approximate chiral symmetry[7] of QCD, which is spontaneously broken at low temperatures, is restored (see [93, 94, 95, 96, 97]). Given that one can assign an order parameter for the deconfinement phase only for the pure gluonic part of QCD [98, 99], chiral symmetry plays a crucial role in describing the phase transition predicted by QCD in hot and dense, strongly interacting matter.

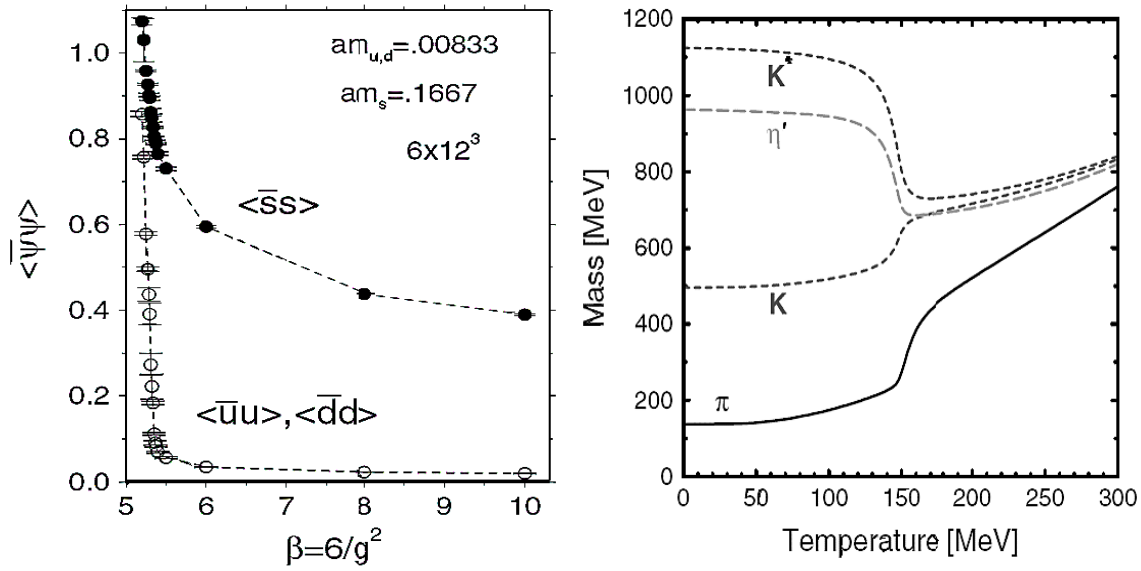

Figure 1.3: Lattice QCD calculations. Left: lattice data for light and strange quark condensate as a function of bare coupling strength β; increasing β corresponds to decreasing lattice spacing and increasing temperature ($\beta \sim T^{-1}$). The plot on the right shows that the chiral transition leads toward a mass degeneracy of the kaon with scalar meson K* mass. Note that the modifications of the hadronic states shown above happen in the vicinity of the phase transition temperature; for details see [100].

The left panel of Fig. 1.3 depicts the light and strange quark condensate as a function of the bare coupling strength β used in the lattice calculations. One sees that the drastic drop of the light quark condensate at high temperatures (larger values of β) is accompanied by a moderate (due to the larger current mass of the strange quark [97]) drop of the strange quark condensate. Thus, also strange particles will be moderated by the chiral or equivalently the deconfinement phase transition. Therefore, strange hadrons can in principle be used as a signal for the chiral phase transition. The advantage of using strange hadrons rather than light nonstrange ones is that strange

[7] Chiral symmetry is related to the helicity of the quarks. If the quark fields are decomposed into left-handed and right-handed components, the QCD Lagrangian with 3 massless quarks is invariant under the independent transformations of right- and left-handed fields ('chiral rotations'). Thus, in the limit of massless quarks, QCD possesses chiral symmetry.

particles can carry information from the high density state as strangeness number is conserved in strong interactions (e.g. the grand canonical count of s quarks in hadrons equals $\bar{s}$ count at each rapidity unit [101, 102]).

The reduction in the chiral condensate with the increase of temperature leads to significant changes of the hadron mass spectra at finite temperature [103, 100], as shown in Fig. 1.3. Note that the change of hadronic masses in a hot medium is confirmed both by experimental data [12] and by lattice calculations [104, 105].

Experimental evidence

As mentioned previously, the reduction in the chiral condensate with the increase of temperature leads to significant variations in in-medium hadron masses. Thus, one expected signal of the restoration of chiral symmetry is a change of properties of various resonances [106, 107, 108, 109, 110]. A change in the effective mass of daughter particles (kaons in the case of $K^\star$ and ϕ mesons) [111, 112] can change the effective lifetime, and consequently the observed width of the parent particle that decays in medium. Hence, the ratio of the decay widths in the lepton and kaon decay channels of the ϕ meson[8] are thought to be sensitive to changes in parton or kaon masses [114].

The predictions are that for both cold and hot nuclear matter there could be a decrease of the ϕ mass value by tens of MeV and an increase of the ϕ width up to a factor 10 [115, 116, 117, 110, 109, 118, 119, 120, 114] Thus far, no significant change of the ϕ mass has been observed at RHIC and SPS experiments [121, 122, 123, 124]. While CERES data for central Pb–Au collisions at $\sqrt{s} = 17.3$ GeV, rule out a possible enhancement of the ϕ yield in the leptonic over hadronic decay channel [125], recent PHENIX analysis for Au–Au colllisions at $\sqrt{s} = 200$ GeV (left panel of Fig. 1.4) seem to indicate that the ϕ yield in the e^+e^- decay channel is larger than in the K^+K^- decay channel, albeit large statistical and systematical errors in the e^+e^- channel [126]. It is noteworthy that strangeness enhancement is clearly seen in the ϕ-meson yield. The right panel of Fig. 1.4 shows a relative enhancement of the ϕ/π ratio compared to pp collisions when the energy of the collision increases [123, 127].

From the current theoretical models it seems, however, that an observed change in the ϕ width would not be itself indicative of a QGP formation. The ϕ width may increase due to ϕ's interactions with partons in the QGP phase but also due to its interactions with hadrons. One would first have to constrain the cold nuclear medium effects on the ϕ from d–Pb collisions for example, or by comparing peripheral Pb–Pb collision data results with central collision data.

One might expect the appearance of a double peak in the mass distribution of the measured ϕ signal [115, 128, 129] at the LHC energies. This effect could be due to the

[8]Note that we restrict our discussion only to the ϕ meson for few reasons: i) ϕ seems to be a more interesting probe given the large variation of its in-medium lifetime as a function of temperature [113] ii) a comparison of the $\phi \to KK/\phi \to ee$ rate is a particularly sensitive measure of a mass modification of either the ϕ or the kaon [112] iii) it is a strange hadron and one of its dominant decay channels, $\phi \to K\bar{K}$, involves kaons.

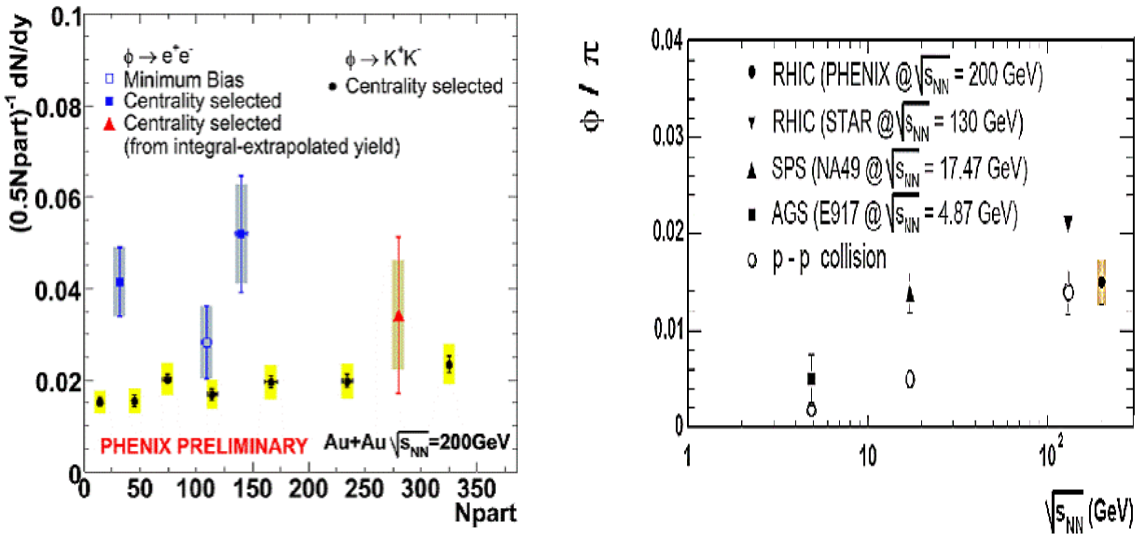

Figure 1.4: Left: Multiplicity dependence of the ϕ yield for e^+e^- and K^+K^- decay channels [126]. Right: ϕ/π ratios as a function of collision energy. The data points are from the $\phi \rightarrow K^+K^-$ channel [123].

rapid decrease of the ϕ's lifetime with rising temperature [113] and due to the non-negligible duration time ($\simeq$ 10 fm/c) of the plasma phase compared to the lifetime of the ϕ in vacuum ($\simeq$ 45 fm/c). In such a case the contribution to dilepton (dikaon) pairs from decays of ϕ-mesons with reduced in-medium mass at phase transition becomes comparable to that from ϕ decays at freeze-out. The mass of a ϕ meson decaying near the phase transition threshold is expected to be lower than the nominal one as a result of partial restoration of chiral symmetry. The value of the mass shift, subject to considerable theoretical uncertainty, depends on various factors, among which, one is the value of the critical temperature [129]. Changes in the relative branching ratio between kaon and lepton pais with respect to the values given in Particle Data Group are predicted [113] as well.

1.1.3 Strange probes to characterize the partonic medium

Strange particles are particularly good probes to investigate the dynamics of the medium produced in collisions [130, 131, 132, 133]. The usefulness of strange particles as probes for the physics of a nuclear collision arises from the fact that they carry a new quantum number not present in the incoming nuclei, and from certain characteristic features in their production and kinetic evolution. In contrast to pions, for example, which are the most efficient carriers of entropy and whose final abundance is thus more or less determined already in the very first, hard collision stage of the reaction where most of the entropy is produced [134], the abundance of strange quarks continues to

evolve until the very end of the collision fireball.

Another important advantage of strangeness is the large variety of strange particle species and the fact that their topological reconstruction allows us to measure identified spectra over a large transverse momentum range with minimal contamination as we shall see in Chapter 5 for the case of the charged kaons. Strange particles can thus be used to determine particle-antiparticle, baryon-meson, parton flavour and simple particle mass dependences as a function of the transverse momentum. Given that particles produced in the collision carry information about the dynamics and the entire space-time evolution of the system from the initial to the final stage of the collision, these measurements characterize the medium in a more specific way (see discussions below), which goes beyond the initial unidentified particle measurements of in-medium modification effects. Being the lightest strange hadrons, kaons dominate the strange particle production.

In the following, we will review recent results directly connected with open questions regarding the dynamics and the relevant degrees of freedom of the matter produced in collision. We shall focus on measurements and observables for which detection of charged kaons is relevant.

An overview of recent results

Contrary to the naive expectations of weakly interacting plasma, RHIC data hint at an equilibrated, collective medium [31, 135, 136, 42, 43, 32] which could be described as an ideal fluid, with minimum viscosity, but still strongly interacting. The observed hadron spectra and correlations reveal three transverse momentum ranges with distinct behaviour: a soft range ($p_T < 2$ GeV/c) containing the remnants of the bulk for which hydrodynamic considerations play an important role, an intermediate range ($2 < p_T < 6$ GeV/c) where hard processes compete with the soft ones, and a hard-scattering range ($p_T > 6$ GeV/c) providing partonic probes of the early stage of collision. For comprehensive reviews of data and extensive discussions we refer to Refs. [73, 42, 43, 44, 39]. The results presented below follow the evolution of the system from the kinetic freeze-out[9] backwards to the earliest stages of the collision.

A lower limit on the lifetime of the fireball between hadronization and kinetic freeze-out can be inferred from the measurement of hadronic resonances by comparing resonance over non-resonance particle ratios for resonances with small regeneration cross-section [137, 138, 139, 140, 65]. The underlying idea is that the interaction of the resonance decay particles with the medium will affect both our detection probability (a resonance decay particle which scatters ellastically in the fireball no longer reconstructs properly to the invariant mass of the initial resonance) and the measured yield (regeneration of resonances in the hadronic phase via coalescence of comoving hadrons is a component of the actual measured resonance yield).

Figure 1.5 shows the relative enhancement/suppression of resonance production as compared to non-resonance production in Au–Au collisions as a function of centrality

[9] At this point all elastic collisions among hadrons cease.

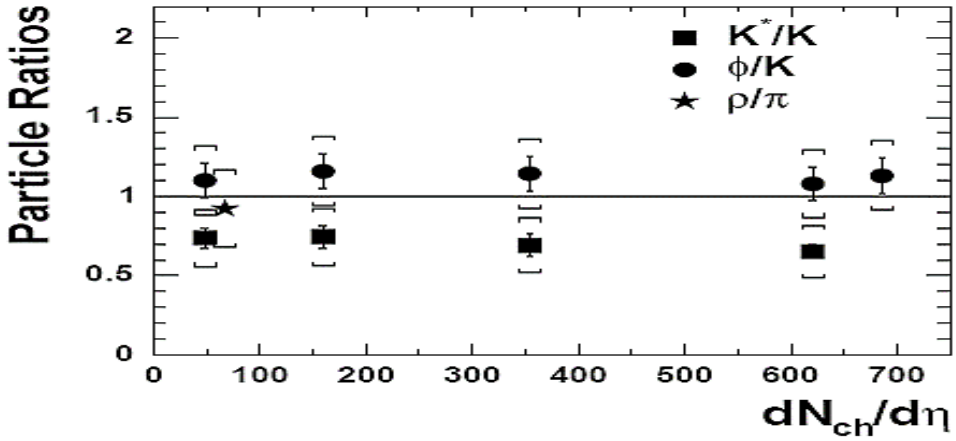

Figure 1.5: The K*/K$^-$, ϕ/K$^-$, and ρ^0/π^- yield normalized to the pp ratios as function of centrality for Au–Au collisions at $\sqrt{s} = 200$ GeV [141].

at $\sqrt{s} = 200$ GeV. Note that all yield ratios are normalized to minimum bias pp. The centrality dependence of the resonance/non-resonance yield ratios depicted in Fig. 1.5 suggests that the ϕ regeneration and the re-scattering of the ϕ decay products are negligible, and the re-scattering of the K* decay products is dominant over the K* regeneration and therefore the reaction channel K$^\star \rightarrow K\pi$ is not in balance.[10] Thus, the K$^\star/K$ yield ratio can be used to estimate the time between chemical and kinetic freeze-outs. The lower limit between chemical and kinetic freeze-outs was estimated to be at least 2 ± 1 fm/c [141] (in accordance with simple entropy-based estimates based on stable particle ratios [142]). Note that the measurements for both K$^\star \rightarrow K\pi$ and $\phi \rightarrow$ K$^+$K$^-$ decays require clean kaon identification in order to reduce the systematic uncertainty due to misidentified correlated pairs (see [141, 123].).

The characteristics of the system at kinetic freeze-out, after elastic collisions among hadrons have ceased, can be inferred from the analysis of transverse momentum distributions of the particles produced[11]. Figure 1.6 shows a compilation of kinetic freeze-out temperature, T_{fo}, and mean transverse velocity, $\langle\beta_t\rangle$, for different hadron species at different centralities. The T_{fo} and $\langle\beta_t\rangle$ parameters have been extracted independently for each particle species from spectra using hydrodynamical fits. Data show that the evolution of the system between chemical freeze-out, when inelastic collisions cease,

[10] In other words, $(\mathrm{K}^\star/K)_{kinetic} = (\mathrm{K}^\star/K)_{chemical} \times e^{-\Delta t/\tau}$, where τ is the K* lifetime of 4 fm/c and Δt is the time between chemical and kinetic freeze-outs. Under the assumptions that i) all the K*s which decay before kinetic freeze-out are lost due to rescattering and ii) there is no regeneration, the minimum bias pp measurement of the K$^\star/K$ yield ratio can be used as $(\mathrm{K}^\star/K)_{chemical}$.

[11] Note that particle abundances at low p_T are well described by thermal models [85, 143, 144]. The values of the parameters of the thermal models, the system's chemical freeze-out temperature (T_{ch}) and baryon chemical potential μ_B, are extracted from the integrated yields of different hadron species, which change only via inelastic collisions.

and kinetic freeze-out is dominated by hadronic rescattering; T_{fo} decreases and the velocity increases for more central collisions, displaying an expected conversion of the internal energy into flow.

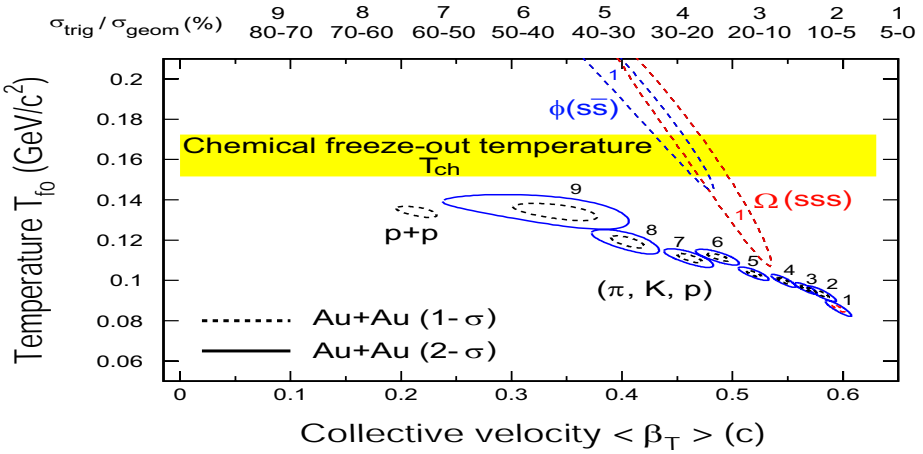

Figure 1.6: The χ^2 contours extracted from thermal+radial flow fits, for π, K, p, ϕ and Ω. On the top of the plot, the numerical labels indicate the centrality selection used in $\sqrt{s}$ = 200 GeV Au–Au collisions. The results from $p+p$ collisions are also shown. Dashed and solid lines are $1-\sigma$ and $2-\sigma$ contours, respectively. As presented in [42] (see references therein).

Results in Figure 1.6 imply that the kinetic freeze-out temperature T_{fo} of multi-strange hadrons is very close to the chemical freeze-out temperature T_{ch}. This could be an indication that these particles decouple almost instantly upon hadronization, but are already carrying a significant radial flow presumably developed in the partonic stage of the collision. This interpretation, however, assumes a low hadronic reinteraction cross section for multi-strange baryons, which has never been measured. The available data for different beam energies also suggest early kinetic freeze-out decoupling [145, 146]. By comparing both multi-strange hadrons and π, K and p behaviour, this trend can be further tested at LHC energies. It would be equally instructive to see if, at LHC energies, $\langle\beta_t\rangle$ increases or starts to saturate.

Note that the hydrodynamic-motivated fits, used to measure the radial expansion velocity, $\langle\beta_t\rangle$, of the system, appear to deviate from the measured spectra at a transverse momentum, which seems to coincide with the scale at which pQCD calculations should become valid. Similarly, the apparent ordering of the strength of the elliptic flow v_2 as a function of particle mass breaks down at a transverse momentum of about 2 GeV/c.

Figure 1.7 (left panel) shows measurements of the elliptic flow at low-p_T for different particle species [136]. Notice the agreement, for p_T below 1.5-2 GeV/c, of the observed hadron mass dependence of the elliptic flow pattern for all hadron species

with the hydrodynamic predictions of models that require a QGP phase[12] [148, 149, 150, 30]. In addition to the near perfect fluid behaviour for p_T below 2 GeV/c, Fig. 1.7 shows that hydrodynamics breaks down at high transverse momenta, $p_T > 2$ GeV/c; instead of continuing to rise with p_T in the p_T range between 2 and 6 GeV/c the elliptic asymmetry stops growing and the baryon $v_2(p_T)$ exceeds the meson $v_2(p_T)$ by a factor approximately 3/2.

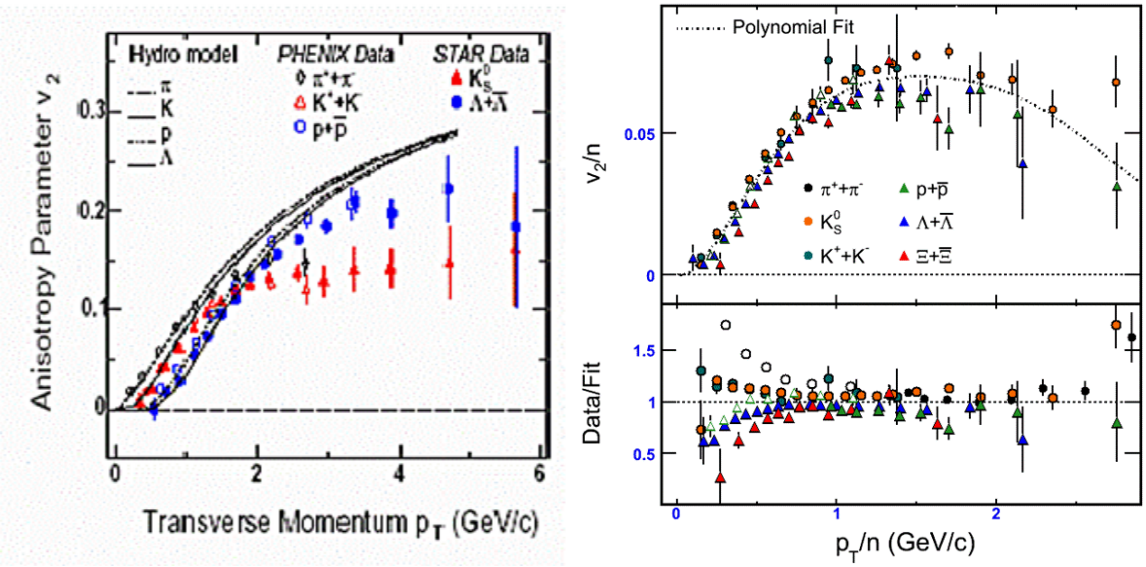

Figure 1.7: Left panel combines STAR [151, 152] and PHENIX [13, 153] measurements of the azimuthal elliptic flow $v_2(p_T)$ of π, K, p, Λ in Au–Au at 200 GeV. The predicted hydrodynamic pattern (solid and dotted lines) agrees well with observations for $p_T < 1$ GeV/c. Right: v_2/n vs p_T/n; n is the number of constituent quarks. The bottom panel shows the deviations from the constituent quark number scaling [154, 155].

An early interpretation of this result was that at these and higher values of p_T, the measured values for the elliptic flow can be accounted for by spatially anisotropic jet energy loss [156, 157, 158, 159]; within the bulk matter, hard parton-parton scatterings lead to the generation of jets, which dominate the high-momentum component of particle spectra and do not equilibrate with the bulk matter. This part of the spectrum should thus agree with pQCD calculations, and indeed the identified single particle spectra in pp collisions at RHIC exhibit the typical pQCD power-law behaviour[13]

[12]Note that due to its 'self-quenching' property, i.e. the pressure-driven expansion tends to reduce the spatial anisotropy that causes the azimuthally anisotropic pressure gradient, the elliptic flow develops earlier than radial flow and is very sensitive to the equation of state of the system. For details, see for instance [42, 147, 32] and references therein.

[13]In pp collisions, the standard picture of hadron production at high p_T involves fragmentation of energetic partons described by factorised fragmentation functions in a pQCD parton model. Because of the power-law nature of the hard scattering spectrum, most of the particles at high p_T are expected

above $p_T = 3$ GeV/c (see [160, 20]). Jet quenching and modifications to the fragmentation functions due to radiative energy loss are are expected to be universal, i.e. independent of the fragmenting parton flavor [161, 162].

At intermediate p_T, however, the results from central Au–Au collisions are inconsistent with the universality of jet quenching and the derived modifications of the fragmentation function. Figure 1.8 shows the nuclear suppression factor[14] R_{CP}, which quantifies the modification (quenching) [161, 163, 164] of these jets when traversing a plasma-like opaque medium formed in $A-A$ collisions, as a function of transverse momentum and particle species [152, 42]. Apparently, all particle species are suppressed in central collisions with respect to peripheral collisions. The data indicate a similar and strong modification factor for pions, kaons and the ϕ meson, independent of their large mass difference. It displays, however, a different suppression pattern for mesons and baryons in the p_T-range between 2 and 6 GeV/c. Apparently, the baryon production exceeds the meson production in the intermediate p_T range. It is at a maximum around 3 GeV/c and decreases back to a value common to all particle species at about 6 GeV/c. Comparisons between the R_{CP} values for baryons and mesons with similar mass, (ϕ,p) and ($K^\star$,Λ), indicate that the behaviour of these suppression patterns does not support models which depend only on the mass of the particle [123, 141].

Based on these measurements a scaling with respect to the number of constituent quarks, n, was suggested [14, 16]. When applied to the v_2 and the p_T-axis, the scaling leads to a common curve for all particles in the p_T range from 2 to 6 GeV/c as shown in the right panel of Fig. 1.7. This apparent scaling behaviour seen in this figure for $p_T/n > 1$ GeV/c is suggestive of a parton coalescence/recombination mechanism in which comoving partons coalesce into the final state hadrons. Several different models, using either thermalized partons [165] or a combination of thermalized and hard scattered partons [166], have been advocated. The lower panel of Fig. 1.7 illustrates the deviations from the quark coalescence ansatz used to scale the data shown in the top panel. The deviations are largest at low-p_T where hydrodynamic scaling was shown to work best. For intermediate-p_T, where the fluid dynamical picture breaks down, the deviations are quite small[15], suggesting that the active and relevant degrees of freedom are 'dressed up' constituent quarks rather than gluons or massless quarks.

It should be emphasized though that in this picture of hadronization, the models do not spell out the connection between the constituent quarks and the properties of the essentially massless partons in a chirally restored QGP. One may guess that the constituent quarks themselves arise from an earlier coalescence of gluons and *current* quarks during the chiral symmetry breaking transition back to hadronic matter, and that the constituent quark flow is carried over from the partonic phase. However, alternative guesses are conceivable. Many recent publications postulate different types

to be leading hadrons.

[14] The nuclear suppression factor R_{CP} is given by the binary-scaled ratio of hadron yields for the most central vs. a peripheral bin, corrected by the expected ratio of contributing binary nucleon-nucleon collisions in the two centrality bins.

[15] Final state effects on the elliptic flow in the hadronic phase have been shown to be small [167].

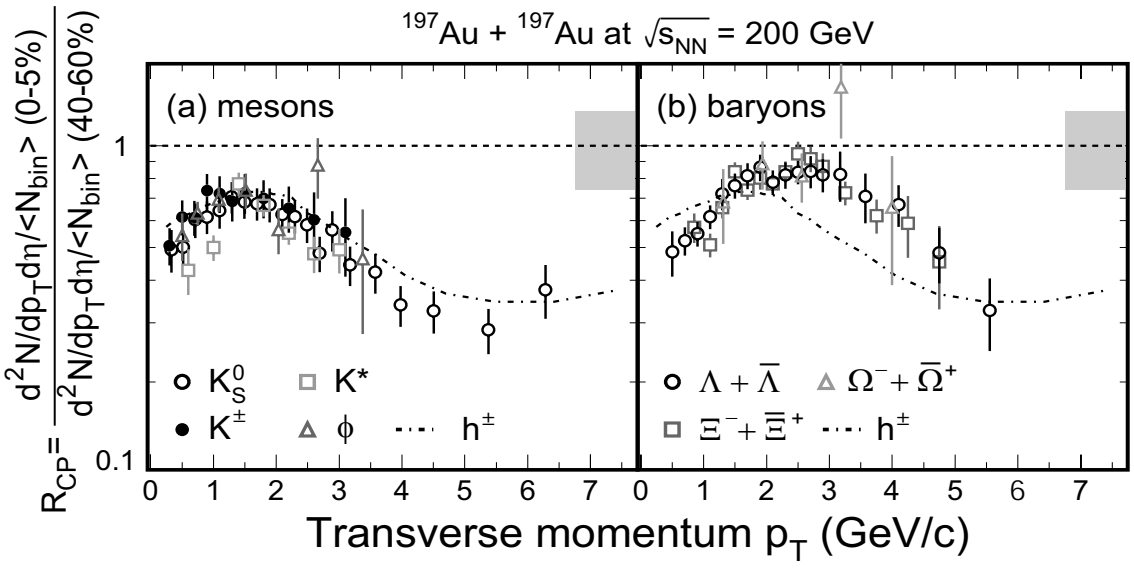

Figure 1.8: Binary scaled ratio R_{CP} of hadron yields for the 0-5% centrality (most central) bin divided by the 40-60% bin at RHIC for 200 GeV Au–Au collisions [42]. The spectra are normalised to the number of binary nucleon-nucleon collisions N_{bin} for each centrality range. Left and right panels show meson and baryon R_{CP} respectively. In each panel, the ratio corresponding to all charged hadrons is shown as the dash-dot line for reference.

of degrees of freedom above T_c that preserve chirality, such as quasi-particles [168], gluonic bound states [169] and quasi-resonances [170]. Another caveat of the recombination models is that at low momentum, energy and entropy conservations become a serious problem for quark coalescence placing an effective lower limit on the p_T range over which the models can be credibly applied. In order to extend this limit down to very low p_T, one has to make specific assumptions about the internal wavefunction of the emitted hadrons [171].

It is interesting to note that the R_{CP} and to a lesser degree, the v_2 plot also suggest that at higher p_T ($p_T >$ 6 GeV/c) the suppression factor is common to all particle species, which could mean that the competition between the recombination and fragmentation hadronization processes gives way to the fragmentation at sufficiently high-p_T. The disappearance of the away-side jet [21, 172] and the R_{AA} nuclear modification factor (difference between the A–A and pp yields) [18, 19] indicates that the jet fragmentation at any measured $p_T > 2$ GeV/c is quenched [173, 174].

As already mentioned, the baryon-meson difference for the nuclear suppression factor and for the v_2 in the intermediate-p_T region, indicates that the fragmentation hadronization process is modified inside the hot and dense medium. The influence of parton-medium interaction on jet fragmentation is one of the open questions that can potentially be answered by measuring flavour dependences in high-momentum two

particle azimuthal correlations and jet topologies [27, 26, 25, 51, 175].

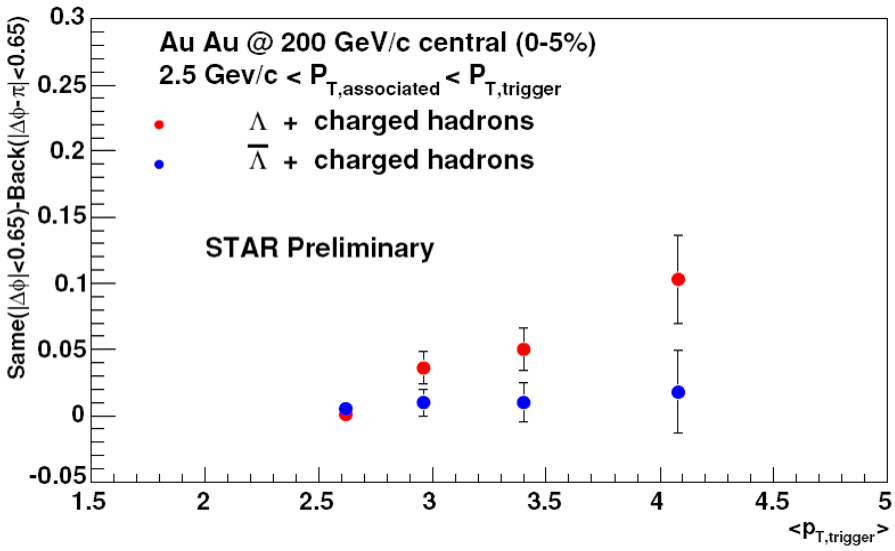

Figure 1.9: Forward-backward difference in correlated yield as a function of transverse momentum of the trigger particle [176].

Figure 1.9 [176] shows a comparison between the Λ and $\bar{\Lambda}$ triggered correlations for sufficiently high-p_T trigger as a function of the p_T of the trigger particle. Plotted here is the dependence of the differences between the associated particle yield in the same side and away side jet cones at intermediate p_T. One expects to see differences in the two particle dependencies that could be attributed to the different production mechanisms of certain particles species, e.g. preferred production of anti-baryons through gluon jet fragmentation rather than quark jet fragmentation. Figure 1.9 shows that the trends of the suppression of the correlations for Λs are different from those for $\bar{\Lambda}$s, which could indicate sensitivity of identified particle jet studies to quenching or production mechanism effects. It is likely that these p_T ranges are still too 'contaminated' by collective effects such as parton recombination and thermal bulk matter production.

By combining the information contained in the R_{CP}, v_2, and two particle correlation measurements one can construct a momentum ordering of different hadronization mechanisms. While thermal bulk matter production appears to dominate at low momenta ($p_T < 2$), in the region up to $p_T \sim 6$ GeV/c, parton recombination and medium modified fragmentation seem to be the dominating production mechanisms. At $p_T > 6$ GeV/c, medium modified fragmentation becomes the dominant production mechanism. At large enough p_T ($p_T > 30$) jet fragmentation should dominate and should at least fix the normalization of the hard parton production. The problem is that the transitions from mechanism to mechanism as a function of momentum are not clearly defined and for many momenta several of these production mechanisms can

contribute. For example, the quenching of jet will push high p_T fragments into the momentum domain presumably dominated by parton recombination.

1.2 What is different at LHC?

In the remainder of this chapter we shall dwell on the key aspects that differentiate the LHC from SPS and RHIC experiments.

The next step in the center-of-mass energy of heavy ion collisions will be taken at the Large Hadron Collider (LHC) scheduled to start operation in 2007 where Pb nuclei will collide with a center-of-mass (cms) energy per nucleon pair $\sqrt{s} = 5.5$ TeV, 30 times higher than at RHIC. In increasing the cms-energy of A–A collisions, it is expected that the system becomes initially denser and hotter, it forms faster and stays collective for a longer time, i.e. its lifetime grows and volume increases. Higher energy density and increased lifetime will enhance the role of the QGP phase over final state hadronic interactions.

1.2.1 Experimental running conditions at LHC

Like the former SPS and ongoing RHIC programme, the heavy-ion programme at the LHC will be based on two components: the use of the largest available nuclei at the highest possible energy and the variation of system sizes (pp, p–A A–A) and beam energies. The ion beams will be accelerated in the LHC at a momentum of 7 TeV per unit of Z/A, where A and Z are in turn, the mass and atomic numbers of the ions. Thus, an ion (A, Z) will aquire a momentum $p(A, Z) = (Z/A) \cdot p_{\rm p}$, where $p_{\rm p} = 7$ TeV is the momentum of the proton beam. Neglecting masses, the center-of-mass energy per nucleon-nucleon pair in a collision of two ions (A_1, Z_1) and (A_2, Z_2) is given by

$$\sqrt{s_{\rm NN}} = \sqrt{(E_1 + E_2)^2 - (\vec{p_1} + \vec{p_2})^2} \simeq \sqrt{4 p_1 p_2} = 2\sqrt{\frac{Z_1 Z_2}{A_1 A_2}} p_{\rm p}. \qquad (1.1)$$

The running programme [177, 53] of ALICE (A Large Ion Collider Experiment), which is dedicated to heavy-ion collisions at the LHC, initially foresees:

- Regular pp runs at $\sqrt{s} = 14$ TeV;
- Runs with Pb–Pb beams at $\sqrt{s} = 5.5$ TeV during 1-2 years;
- Runs with p–Pb (or d–Pb or α–Pb) beams at $\sqrt{s} = 8.8$ TeV during 1 year;
- Runs with Ar–Ar beams at $\sqrt{s} = 6.3$ TeV during 1-2 years;

As we have seen for SPS and RHIC, the proton-proton and proton-nucleus runs are compulsory as they provide the reference system for comparison of the results obtained with A–A collisions in which QGP is expected to be formed. The runs with

lighter ions, e.g. argon, will allow to vary the energy density and the volume of the produced system.

For Pb–Pb collisions the maximum (initial) luminosity is $\mathcal{L} = 10^{27}$ cm^{-2}s^{-1}. The situation is different in the case of pp running conditions of ALICE at the nominal LHC cms energy of $\sqrt{s} = 14$ TeV. In pp collisions, the maximum machine luminosity that ALICE can tolerate is about $\mathcal{L}^{max} = 5 \cdot 10^{30}$ cm^{-2}s^{-1} [53], three orders of magnitude below the design value for the other experiments. This limitation is imposed by the maximum number of pile-up events we can tolerate in the slow drift detectors.

For total rate estimates, all LHC experiments have agreed to use an effective time per year of 10^7 s for pp and 10^6 s for heavy-ion operation, since the LHC is expected to run essentially in the same yearly mode as the SPS (starting with several months of pp running followed by several weeks of heavy-ion collisions at the end of each year).

1.2.2 Discussions and expectations at LHC energies

The emerging picture from RHIC shows that many physics analyses which are essential for model validations and experimental cross-checks will be largely improved upon or even rely on particle identification at intermediate and high p_T, in particular on identification of strange particles as they are more sensitive to early stages of collision.

We have seen that hydrodynamic calculations are best able to reproduce RHIC results for hadron spectra and the magnitude and mass-dependence of elliptic flow by using an equation of state (EoS) containing a soft point[16] inspired by lattice-QCD predicted phase transition from QGP to hadron gas [179, 150, 148]. However, the calculations exhibit comparable sensitivity to other a priori unknown features like the details of the hadronic final-state interactions and the time at which thermal equilibrium is first attained. Therefore, it is not yet clear if the experimental results truly demand an EoS with a soft point [147]. Also it is not obvious whether the hydrodynamic limit for collective flow will prove to be relevant to heavy-ion collisions at LHC energies as well [42]. If this should be the case, at LHC the elliptic flow should follow the hydrodynamical (mass-dependence) behaviour over a p_T range, p_T up to $p_T < 4 - 5$ GeV/c, that is almost twice as wide as that at RHIC [180]. Evidently, the particle identity information will be vital for a quantitative analysis and interpretation of the results.

In the intermediate-p_T range, while the quark recombination models can provide a reasonable account for the systematics of the meson-baryon differences, it is yet to be demonstrated that the coexistence of coalescence and fragmentation processes is quantitatively consistent with azimuthal dihadron correlations observed over p_T ranges where coalescence is predicted to dominate. As already discussed, the relation between the constituent quarks and the properties of the essentially massless quarks and gluons in a chirally restored QGP cannot be yet inferred from the recombination models.

[16] The slope $\partial P/\partial \epsilon$ (giving the square of the velocity of sound in the matter) exhibits high values for the hadron has and, especially, the QGP phases, but has a minimum at the mixed phase [178]; P denotes the pressure and ϵ the energy density.

Including gluons in recombination, B. Müller predicted recently systematic baryon-meson violations of the constituent quark number scaling at the few-percent level [181, 182]. However, another source of such deviations from the scaling law can be caused by the internal momentum distribution of constituent quarks [183]. Extrapolations to the LHC energies [184, 47] show that at LHC the intermediate-p_T region will extend to higher momenta than at RHIC. The transition point between recombination and fragmentation dominance is up to about 8 GeV for pions (4 GeV at RHIC) and up to 10 GeV for protons (6 GeV at RHIC) when assuming a hadronization temperature of 175 MeV and a transverse radial flow of $v_T = 0.75c$. Particle identification in this transition region is crucial for a confirmation of the recombination model and to disentangle the contributions from different particle production mechanisms, e.g. recombination versus jet fragmentation. An important observable, similar as at RHIC, will be the species dependence of the elliptic flow, which is predicted to derive from a universal partonic flow pattern.

At even higher momenta, it will be interesting to study both inclusive spectra and jet fragmentation with identified particles. Both observables are related to the energy loss of hard scattered partons in the surrounding hot and dense matter. By identifying the leading hadron, one may be able to enrich the jet sample with either quark or gluon jets [185], which suffer different amounts of energy loss in matter owing to the different colour charges of the scattered parton. The hadron composition in the soft part of the spectrum of the hadrons associated with the jet may contain information about the interaction between the energy radiated into low momentum gluons and the surrounding matter.

At LHC a new situation will occur both in A–A and in pp collisions, see Fig. 1.10. The dominance of jets and minijets will raise new questions since the final hadronic yields will originate from two different sources: a source reflecting the equilibrated (grand) canonical ensemble (soft physics) and on the other hand the fragmentation of jets whose contribution will differ from the behavior of an equilibrated ensemble. Due to the large number of the newly produced particles, a 'chemical analysis' (i.e., the freeze-out parameters can be extracted for single events) of the collisions will be possible. By triggering on events with one, two or more jets, a possible correlation between intial and freeze-out phase may be extracted. This very new opportunity allows to study whether the occurrence of hard processes will influence the distribution of the 'soft physics' part. Particularly interesting in this context is the behaviour of strange and multi-strange particles, e.g. the K/π or Ω/π ratio in combination with extremely hard processes. More details can be found in [186].

Measurements that are of particular interest and will only be possible at LHC (or RHIC-II) include: a) the measurement of identified particle fragmentation functions in up to 30 GeV/c γ–jets; b) measurements of inter-jet correlations of high-p_T strange particles out to $p_T > 6$ GeV/c of the associated particle momentum ($K^{\pm} - K^{\pm}$, $K^{\pm} - \Lambda$, $K^{\pm} - \bar{\Lambda}$, $\Lambda - \bar{\Lambda}$), in order to measure the contribution of gluons and sea quarks to the hadronization and the quenching behaviour as a function of parton flavor and in order to see whether a $s - \bar{s}$ correlation exist; c) the measurement of

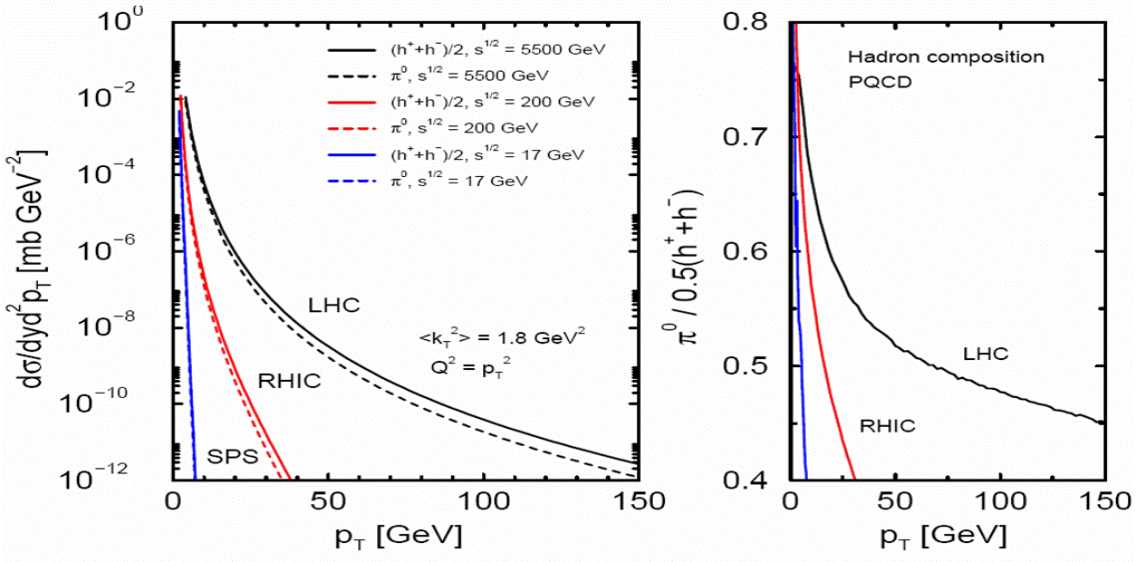

Figure 1.10: The predicted leading order (LO) differential cross section for neutral pion and charged hadron production for pp collisions at $\sqrt{s}$ =17, 200, and 5500 GeV. The predicted hadron composition in pp is plotted in the right pannel.

flavor particle production in order to identify differences between gluon and quark fragmentation.

Let us now turn to strangeness as signature of QGP. RHIC results show clearly that strange quark production in hot QCD is far from being settled. Most fits to the RHIC data yield an almost perfect abundance equilibration of strange hadrons (the strangeness phase space occupancy $\gamma_s = 1$) [187, 143]. However, other high-quality fits of hadron yields [188, 86] invoke a significant over-saturation of strangeness[17]. In the Statistical Hadronization Model (SHM) of Rafelski and Letessier [189, 101] it is argued that because in the QGP and the hadron gas phase the carriers of strangeness have different masses, the value of γ_s does not have to remain the same during the transition; γ_s grows with decreasing chemical freeze-out temperature [190, 191]. This suggests that at LHC strangeness may be further enhanced relative to RHIC given that at LHC we reach greater initial temperatures and more explosive transverse flow which can lead to supercooling and pushes the chemical freeze-out temperature to lower values [190]. The exact value of γ_s for LHC energies is not known, but values much larger than 2 might be expected. As mentioned above, a specific property of this approach is a decrease of the temperature T for increasing γ_s as shown in the upper part of Fig. 1.11 left. The particle ratios vary strongly with γ_s, see right panel of Fig. 1.11 for two ratios of strange-over-non-strange particles. This variation is even

[17] Note that the phase space occupancies considered are those arising from hadron yields, the excess above chemical equilibrium does not imply that the underlying state, e.g., deconfined QGP is not chemically equilibrated.

stronger when studying multi-strange particles [190]. It should be noted that in the SHM model, for $\gamma_s = 1$ lower values are obtained compared to the case in which calculations assume chemical equilibrium (crosses). If, as expected by Rafelski and Letessier, values of γ_s around 5 – 10 will be reached at LHC energies the particle ratios will differ strongly from the equilibrium situation.

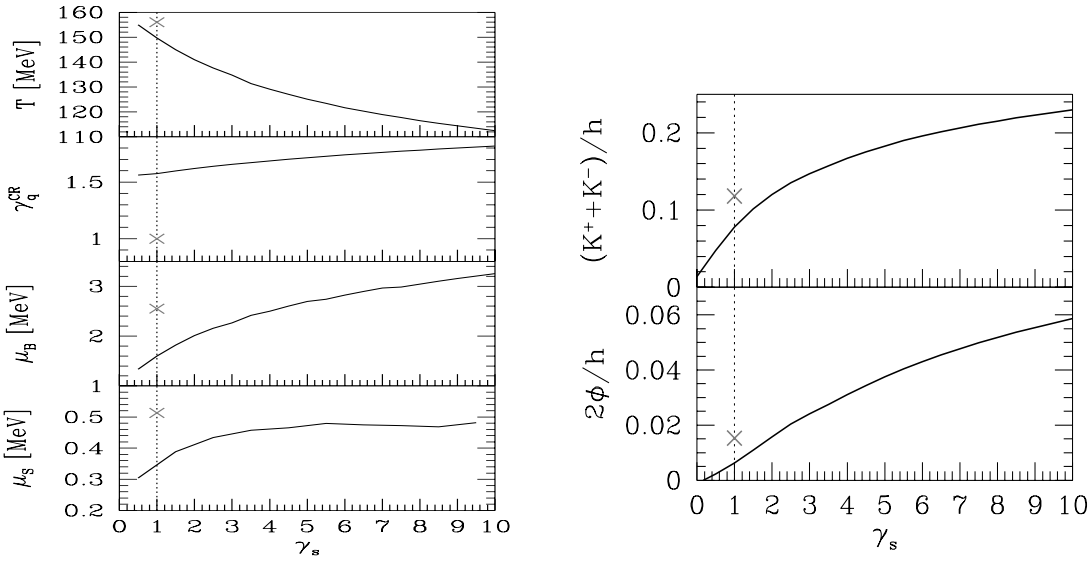

Figure 1.11: Left: The values of hadronization temperature, T, maximum quark phase space occupancy, ${\gamma_q}^{CR}$, and baryon, μ_B, and strange, μ_S, chemical potentials, as a function of γ_s as obtained in the hadronization model [190]. Right: Particle ratios of $K^+ + K^-/h$ and $2\phi/h$ as a function of γ_s. The crosses indicates chemical equilibrium model predictions. From [190].

Given that kaon production will dominate the strange sector, one question that arises naturally, and the main focus of this study, is what is the kaon identification range we can achieve on a track-by-track basis. Does this identification range allow us to use kaons to get insight into phenomena related to each of the transverse momentum ranges and the open questions mentioned above?

As our study is performed for the ALICE experiment, in the next chapter we will introduce the ALICE setup with particular emphasis on the main tracking device, the Time Projection Chamber, which constitutes practically the fiducial volume within which we try to reconstruct the charged kaons using the decay topology.

Chapter 2

The ALICE experiment

ALICE (A Large Ion Collider Experiment) is conceived as a general-purpose experiment whose detectors measure and identify hadrons, electrons, photons and muons. The ALICE detectors are optimized for the study of heavy-ion collisions up to the highest energy available. As such, the detector system has been designed to be capable of measuring *simultaneously* properties of the bulk (soft hadronic, large cross-section, physics) and of rare probes (hard, small cross section, physics). In particular, ALICE has to be able to track and identify particles from very low, ~ 100 MeV/c up to fairly high, ~ 100 GeV/c transverse momenta in an environment of extreme particle density.[1]

2.1 Layout of the detector system

The ALICE setup in its final layout, together with the physics objectives, design considerations and a summary of the present status of the ALICE sub-systems, is described in Ref. [53]. The individual sub-systems of the ALICE setup are described in detail in technical design reports and addenda [195, 196, 197, 198, 199, 200, 201, 202, 203, 198, 204, 205, 206, 207, 208].

As shown in Fig. 2.1, the ALICE setup combines three major components:

- The central barrel, contained in the large L3 magnet and composed of detectors devoted to the study of hadronic signals, electrons and photons. It covers the pseudorapidity range $|\eta| < 0.9$ over the full azimuth angle;

- The forward muon spectrometer for detection and identification of muons or muon pairs from the decay of quarkonia in the interval $-4.0 \leq \eta \leq -2.4$;

[1] Theoretically founded predictions for the multiplicity in central Pb–Pb collisions at the LHC range at present from 2000 to 6000 charged particles per rapidity unit at mid-rapidity [192, 193] (for a review, see for instance [194]). The ALICE detectors are designed to cope with multiplicities up to 8000 charged particles per rapidity unit, a value which ensures a comfortable safety margin.

- The forward detectors ($-3.4 \leq \eta \leq 5.1$), for a determination of the photon multiplicity and a measurement of the charged particle multiplicity, also to be used as a fast trigger on the centrality of the collision.

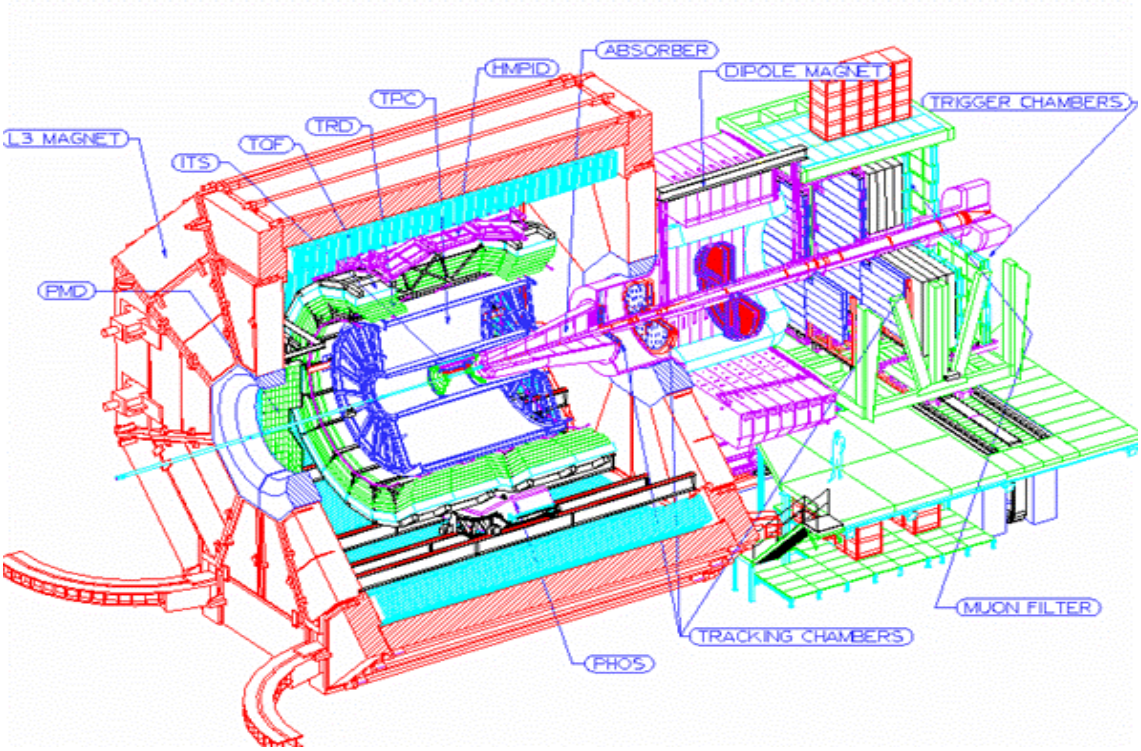

Figure 2.1: The ALICE setup in its final layout. For the sake of visibility the HMPID detector is shown in the 12 o'clock position instead of the 2 o'clock position at which is actually located.

The central system is embedded in a large solenoidal magnet which generates a weak field of ≤ 0.5 T, parallel to the beam axis. It consists, from the interaction vertex to the outside, of six layers of high-resolution silicon detectors (Inner Tracking System - ITS), the main tracking system of the experiment (Time-Projection Chamber - TPC), a transition radiation detector for electron identification (Transition Radiation Detector - TRD), and a particle identification array (Time Of Flight - TOF). The central system is complemented by two small-area detectors: an array of ring-imaging Cherenkov detectors ($|\eta| \leq 0.6, 57.6°$ azimuthal coverage) for the identification of high-momentum particles (High- Momentum Particle Identification Detector - HMPID), and a single-arm electromagnetic calorimeter ($|\eta| \leq 0.12, 100°$ azimuthal coverage) of high density crystals (PHOton Spectrometer - PHOS). The large rapidity systems include a muon spectrometer ($-4.0 \leq \eta \leq -2.4$) designed to measure the complete spectrum of heavy quark resonances, a photon counting detector (Photon Multiplicity

Detector - PMD, on the opposite side), and an ensemble of multiplicity detectors (Forward Multiplicity Detector - FMD) covering the large rapidity region (up to $\eta = 5.1$). A system of scintillators (V0 detector) and quartz counters (T0 detector) will provide fast trigger signals, and two sets of neutron and hadron calorimeters, located at 0° and about 90 m away from the interaction vertex will measure the centrality(Zero-Degree Calorimeter - ZDC). The muon spectrometer consists of a warm dipole magnet providing an integral field of 3 Tm, five tracking stations, an iron wall (muon filter) to absorb the remaining hadrons, and two trigger stations behind the muon filter. It is shielded by an absorber positioned very close to the vertex (≈ 90 cm).

The magnetic field strength is a compromise between momentum resolution, acceptance at low-momentum, and tracking and trigger efficiency. The momentum cut-off should be as low as possible (≈ 100 MeV/c), in order to detect the decay products of low-p_T hyperons and reject the soft conversion and Dalitz background in the lepton-pair spectrum. At high p_T, the magnetic field determines the momentum resolution, which is essential for the study of jet quenching and high-p_T leptons. The ideal choice for hadronic physics, maximising reconstruction efficiency, is around 0.2 T; for the high-p_T observables ALICE will run with the maximum field the L3 magnet can produce, 0.5 T.

The beam pipe has the smallest possible thickness in terms of radiation length (0.3%) to minimize multiple scattering and nuclear interactions undergone by the particles produced in the collision. It is built from beryllium and it has an outer radius of 3 cm.

In central barrel, charged particle tracking is provided through ITS, TPC and TRD, TPC being the main tracking detector of the experiment. For a large part of the phase space, the identification of particles is performed using $\mathrm{d}E/\mathrm{d}x$ measurements and topology information from the ITS and TPC, the time of flight information from the TOF detector [198, 199] and the Cherenkov radiation in the HMPID [200]. Electron identification above 1 GeV is obtained exploiting the e/π separation provided by the transition radiation in TRD. Prompt photon and neutral meson identification through the two-photon decay channel is provided by the PHOS detector. In order to extend the coverage for the electromagnetic calorimeter, the addition of a large lead-scintillator sampling Electromagnetic Calorimeter (EMCAL) has been proposed [200, 209]. The detector, which is foreseen to cover $\Delta\eta \times \Delta\phi = 1.4 \times 2\pi/3$, will be positioned next to the HMPID and opposite to PHOS. It will be optimized for the detection of high-p_T photons, neutral pions and electrons, and together with the barrel tracking detectors will improve the jet energy resolution.

For convenience, we will give a brief description of the tracking detectors TPC in particular, in the following sections; for details, we refer to the respective Technical Design Reports.

2.2 Inner Tracking System

The basic functions of the inner tracker [195] are: a) primary and secondary vertex reconstruction with the high accuracy that is required for the detection of hyperons and open charm and open beauty. b) particle identification and tracking of low-momentum particles which are strongly bent in the magnetic field and/or do not reach TPC. c) improvement of the momentum resolution. The ITS consists of six barrels of high-resolution silicon detectors, located at r=4, 7, 15, 24, 39 and 44 cm. It covers the pseudorapidity range of $|\eta| < 0.9$ for collisions with vertex located within the length of the interaction diamond, i.e. $-5.3 < z < 5.3$ cm along the beam direction. The innermost layer has a more extended coverage ($|\eta| < 1.98$) to provide, together with the forward multiplicity detectors, a continuous coverage in rapidity for the measurement of multiplicity of charged particles.

To cope with the high particle density, up to 80 particles per cm^2, and for good impact parameter resolution below 100 μm, silicon pixel detectors will equip the innermost two layers and silicon drift detectors the following two. The two outer layers will be equipped with double-sided silicon micro-strip detectors as the requirements in terms of granularity are less stringent. The outermost four layers will have analog readout for independent particle identification via $\mathrm{d}E/\mathrm{d}x$ in the $1/\beta^2$ region [210, 60]. The average amount of material is kept around 1% of radiation length per layer.

2.3 Time Projection Chamber

The Time Projection Chamber (TPC) [196] is the main tracking system of the detector and the main tool to investigate hadronic observables. Its task is to provide, together with the other central barrel detectors, track finding, momentum measurements and particle identification via energy loss measurements ($\mathrm{d}E/\mathrm{d}x$).

The TPC, shown in the right panel of Fig. 2.2, is a large horizontal cylinder with full coverage in azimuth and an overall active length of 500 cm covering the pseudorapidity range of $|\eta| < 0.9$. Its inner radius of about 85 cm is given by the maximum acceptable hit density and its outer radius of about 250 cm is given by the track length required for a $\mathrm{d}E/\mathrm{d}x$ resolution better than 7% which is necessary for particle identification. The TPC is placed inside the L3 solenoid magnet which generates a weak field (≤ 0.5 T) parallel to the axial electric field inside the TPC, and parallel to the beam axis. The detector is made of a large field cage built of low-density and low-Z materials to minimize multiple scattering, γ conversion and secondary hadronic interactions. It provides uniform back-to-back drift fields of 400 V/cm to transport electrons from the ionization over distances of 2.5 m towards the readout end-plates. Given the long drift path, the high voltage of the central electrode will be as large as 100kV and each of the two opposite axial potential degraders, suspended on 18 rods, consists of 166 potential steps made by aluminized Mylar strips. The large drift volume (88m^3) inside the field cage is filled with a 85%Ne +

$5\%N_2 + 10\%CO_2$ mixture optimized for drift velocity, low electron diffusion and high radiation length and hence low multiple scattering, small space-charge effect and aging properties. The overall thickness of TPC was kept below 3% of radiation length.

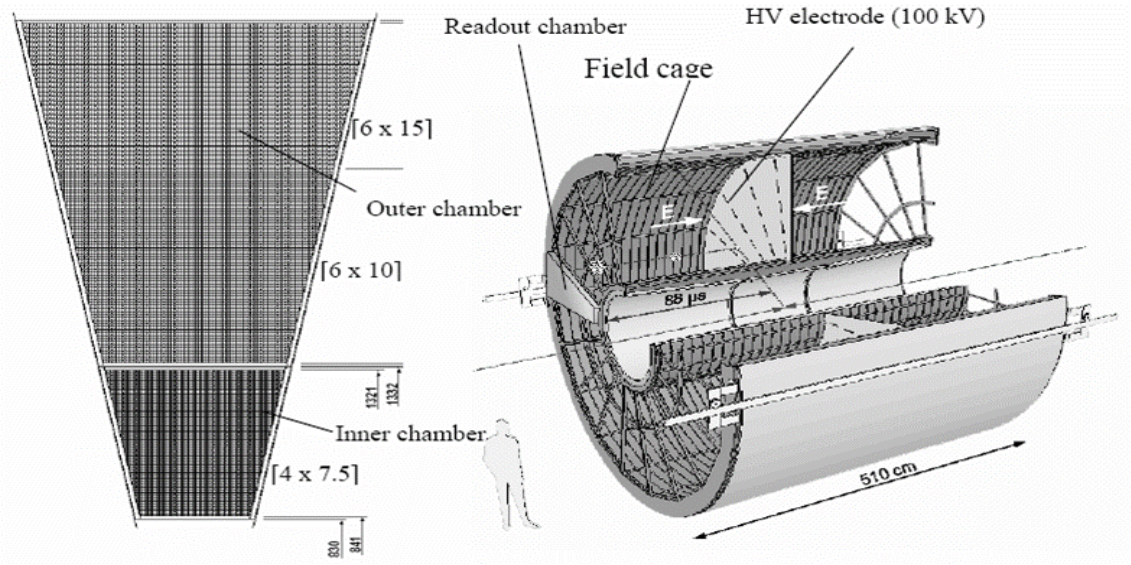

Figure 2.2: Right: The ALICE TPC showing the central electrode, the field cage and the segmented end plates on which the readout chambers are mounted. Left: Pad layout of the inner and outer readout chambers corresponding to one of the 18 azimuthal sectors of an end-plate. The numbers in brackets represent the pad sizes in mm.

Each of the two end-plates of the TPC is azimuthally segmented in 18 sectors, each covering an angle of 20°. The readout chambers are mounted into the sector cut-outs of the end-plates, see Fig. 2.2; they are conventional multiwire proportional chambers with pad readout and their design have been optimized to address additionally to the momentum and $\mathrm{d}E/\mathrm{d}x$ resolution, the questions of rate capability and two-track separation in a high track density environment. The readout plane is radially segmented and each sector consists of one inner and one outer chamber, see the left panel of Fig. 2.2, with pads radially oriented according to the average local track angle. The inactive areas (3 cm wide in the azimuthal direction) between neighboring inner chambers are aligned with those between neighboring outer chambers in order to optimize the momentum precision for high-momentum tracks. As a result, in about 10% of the azimuthal angle the detector is not sensitive.

To keep the occupancy as low as possible and to ensure the necessary $\mathrm{d}E/\mathrm{d}x$ and position resolution, there are about 570 000 readout pads of three different sizes: 4×7.5 mm^2 in the inner chambers, 6×10 mm^2 and 6×15 mm^2 in the outer chambers. In each inner chamber the pads are distributed over 63 pad rows running parallel to the wires; they are located between 84.85 cm and 132.1 cm from the beam line. The

pads in each of the outer chambers are distributed over 64 pad rows located between 134.6 cm and 198.6 cm, and 32 pad rows located between 198.6 cm and 246.6 cm. The signal picked up by pads is sampled with a frequency of about 5.66 MHz, dividing the drift time into about 500 time-bins, corresponding to a total drift time of about 88 μs. During the drift time about $3 \cdot 10^8$ 10-bit amplitudes are produced, which subsequently are processed by the TPC front-end electronics [211].

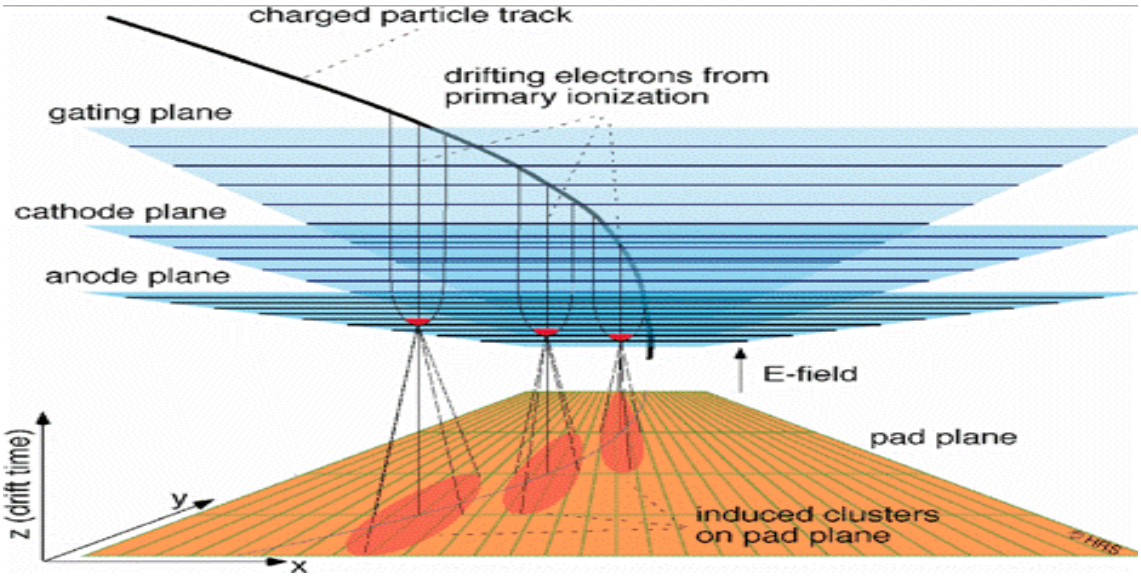

Figure 2.3: The operating principle of TPC

The TPC records the passage of all charged particles in the following simplified way, illustrated in Fig. 2.3. Charged particles traversing the TPC volume ionize the gas along their path liberating electrons and thus leave behind a trail. These electrons drift, due to the electric field applied, towards the anode wires at the end-plates of the TPC, where they produce small charge avalanches due to high electric fields around the wires. Moving from the anode wire towards the surrounding electrodes, positive ions, created in the avalanche process, induce a positive signal on the nearby pads which are read out electronically. The properly weighted barycenter of the charges distributed over the pads gives the position of the avalanche. The position of the particle in the drift direction (z-direction) is determined by sampling the time distribution of each pad signal. Provided the electric and temperature fields are uniform, the electron cloud drifts at a constant velocity towards the readout and the measured drift time is directly proportional to the distance of the impact point from the readout. Thus the TPC delivers, without ambiguities, genuine space points along a particle trajectory.

Since TPC is the main tracking detector and the performance of the TPC in terms of momentum, $\mathrm{d}E/\mathrm{d}x$ and two-track resolution is directly correlated with the performance of the readout chambers such as position resolution, we list here several effects which generate the measurement error:

- The loss of ionization electrons due to the electron capture;
- The broadening of the electron cloud due to lateral diffusion during drift. This contribution to the variance is proportional to the drift length. It is the dominant effect for large drift distances.
- Exponential fluctuations in the gas amplification of single electrons, which effectively enhance the de-localization caused by diffusion approximately by a factor $\sqrt{2}$.
- The stochastic behavior and energy/space distribution of the primary electrons including outliers from energetic electrons (δ-rays). This contribution is constant for a fixed gas mixture, but can depend on the angle between the anode wire and the magnetic field.
- The stochastic character of secondary electron production (Landau fluctuations). This contribution enters only when the track is inclined with respect to the pad orientation.
- Different path lengths for different primary electrons due to inhomogeneities in the drift field and the field near the anode wire.
- Effects of digitization and threshold.

The stochastic proceses responsible for some of these effects, and their contributions to the accuracy of the local coordinate position measurement and error parameterizations are described in detail in [196, 212] and references therein.

The track reconstruction strategy and performance of the TPC in the high-multiplicity environment of heavy ion collisions will be discussed in the next chapter.

2.4 Transition Radiation Detector

The main goal of the TRD [197] is to provide electron identification in the central region at momenta in excess of 1 GeV/c where the pion rejection via energy loss measurement in the TPC is no longer sufficient. The TRD consists of six layers of radiator fiber stacks followed by time expansion chambers filled with Xe/CO_2 (85/15), providing an e/π rejection power of 100 in high multiplicity operation. There are 540 modules organized in 18 sectors matching the azimuthal segmentation of the TPC. Along the beam direction there is a 5-fold segmentation. Each module consists of a radiator of 4.8 cm thickness and a multi-wire proportional chamber. Each readout chamber consists of a drift region of 3 cm; the drift time is 2 μs. The signal is sampled in 20 time-bins. The high-granularity readout chambers are equipped with over one million electronics channels. The electronics provides the time and analog information of the clusters, and proceeds to a fast local reconstruction to produce a Level-1 trigger

within 6 μs after the collision. The TRD is used to trigger on high-p_T leptons and hadrons. The detector in its full configuration covers the central barrel region of ALICE and fills the space between the TPC and TOF detectors. Its total thickness (about 14% radiation length) is a compromise between the necessity to minimize small angle scattering, bremsstrahlung and showering for the efficient identification of the electrons, and the need to provide mechanical stiffness for the proper operation of the readout chambers.

2.5 Offline computing

The ALICE off-line framework, AliRoot [213], is based on the Object Oriented paradigm, and is developed using the C++ programming language, the ROOT system [214] being the base for this development. Its role is to allow the reconstruction and the physics analysis of data coming from simulations and real interactions in a seamless way, i.e. without the need of changing the user code. Events are generated via Monte Carlo simulation programs, including generators and detector simulation, and are then transformed into the data format produced by the detector (raw data). Here we have a minimum of the physics information since the full information (i.e. particle ID and kinematics, topology) of the particles produced by the event generators gets disintegrated and reduced to that generated by particles when crossing a detector. At this point, the raw data, real or simulated, is 'fed into' the reconstruction and analysis chain used to evaluate the detector and the physics performance. The information about the particles is thus reconstructed, and is finally compared to the generated one. A detailed description of the AliRoot framework, event generators and data processing chain, i.e. simulation of the detector response and event reconstruction, can be found in Ref. [53, 215]. Here we only mention that for the simulation of the central Pb–Pb collisions at the LHC energy we have chosen the HIJING [216, 217] generator. The choice is based on the fact that HIJING reproduces many inclusive spectra, two-particle correlations, and the observed flavor and multiplicity dependence of the average transverse momentum (see [218, 53, 219]). To simulate the pp collisions at the LHC energy we have used PYTHIA [220, 221, 222]. The main settings employed for the event generators are listed in Appendix A.2.

Chapter 3

Track reconstruction

In this chapter, after a brief note on the requirements for the performance of the tracking algorithms in ALICE and on the Kalman filter, we present the global tracking strategy and focus on the track reconstruction in the TPC, particularly on tracking performance as the latter sets the lower bounds on the reconstruction of decay topologies.

3.1 Tracking requirements in ALICE

The physics program of ALICE [53] dictates the design considerations for the experimental setup and imposes a set of requirements on the reconstruction performance. These requirements are detailed in the ALICE technical proposal [223] and in technical design reports and addenda [195, 196, 202, 198, 199, 200, 201]. Here, we give only a brief summary of the requirements imposed on reconstruction algorithms:

- **Tracking efficiency**: We aim at 90% or better track finding efficiency for all transverse momenta down to $p_T = 100$ MeV/c in order to have sufficient statistics in a single event for event-by-event studies of fluctuations in observables such as the K/π ratio and for rare and/or large background signals such as lepton pairs, charm, etc. In addition, we need as good as possible efficiency for low-p_T tracks, in particular electrons and positrons, in order to suppress the background in the electron pair analysis. **Fake** tracks must be kept as low as possible.

- **Transverse momentum resolution**: The relative momentum resolution should be about 1% for momenta around the average value (~ 2 GeV/c) and should not exceed few % for the high momentum tracks in order to achieve the required effective mass resolution for different particles and resonances (e.g. ϕ, ρ, ω, hyperons, D mesons, J/ψ)

- **Resolution in** d**E**/d**x**: For hadron identification on a track-by-track basis in the relativistic region $\beta\gamma > 5 - 6$, a dE/dx resolution better than 7% is desirable.

- **Angular and impact parameter resolution**: The impact parameter resolution should be significantly better than 100 μm for the charm measurements. The angular precision should be of the order of 1 mrad.

- **Two-track resolution**: The two-track resolution should be such that HBT measurements[1] with a resolution in relative momentum of a few (< 5) MeV/c can be performed.

- **Robust** towards noise in conditions of high occupancy of electronic channels. We have about 50% occupancy in the inner sectors of the TPC for the maximum expected track multiplicity.

- **Fast** in order to be able to cope with the amount of collected data. The typical size for a Pb-Pb event is of about $\sim$ 87 MB and the statistics required for certain physics, like charm physics, is of the order of 10^7 events.

- **Flexible** so that the reconstruction program is able to deal with any required combination of individual detector modules, still of a simple architecture.

Performance studies with different track-finding methods have led to the choice of the Kalman filter method for track reconstruction in ALICE. Some features and the main steps of the Kalman-filtering approach for track finding are mentioned very briefly in the next section. There is a rather vast literature on pattern reconstruction and track fitting methods, and Kalman filter in particular. For a comprehensive review the reader is referred to [224, 225, 226] and references therein.

3.2 Kalman filter

The purpose and virtue of a Kalman filter (KF) [227] approach is to integrate in an efficient and compact way both the track finding and track fitting steps [228, 229]. Space points from the various detectors must be associated to particle trajectories, and fitted to determine the curvature, and more generally, the momentum and species identity of the particle.

The Kalman filter and its associated smoother are least-squares estimators which are specially adapted to sequential measurements. The track is regarded as a dynamic system. The state of the system at a given surface defined by the shape of the detector (pad rows in the case of TPC) is described by the track parameters[2] at the

[1] The Hanbury-Brown and Twiss effect (HBT) is any of a variety of correlation and anti-correlation effects in the intensities received by two detectors or at two different positions in a detector from a beam of particles. In heavy-ion collisions, this two (or more) identical particle interferometry technique is used to study the dynamical evolution and the space-time structure of the emitting source at freeze-out.

[2] There are five parameters which describe the track uniquely in each point of its trajectory: the intersection points and the direction angles of the trajectory with the surface where the measure-

intersection point. The Kalman filter includes the information of each additional measurement, thus improving iteratively the information on the current track parameters. The information is added by the means of the least squares method in four steps:

1. Given an estimate of the state vector (the vector of track parameters) on detector surface k the trajectory is extrapolated to surface $k+1$ by means of track model.

2. The covariance matrix of the extrapolated state vector is computed by error propagation.

3. The covariance matrix of the process noise (multiple scattering and energy loss) between surface k and surface $k+1$ is added to the propagated covariance matrix.

4. The optimal estimate of the state vector at position $k+1$ is computed by the weighted mean of the extrapolated state vector and the detector measurement at surface $k+1$. The information contained in this estimate can be passed back to all previous estimates by means of a second filter running backwards or by the smoother.

The smoother enables the optimal estimation of track parameters anywhere along the track, not only at some reference surface. It is implemented by a weighted mean of two filters running forward and backward, with the filter running firstly in the direction towards vertex. In the second filter, the same corrections, but with opposite sign, and the same variances, are used in the respective prediction steps. This allows to avoid inconsistencies between the two filters. For convenience, the basic mathematical formalism of the filter is given in Appendix A.3.

The filter is very powerful in several aspects:

- It supports estimations of the past, present and even future states, and it can do so even when the precise nature of the modeled system is unknown. Thus, the linear approximation of the track model does not need to be valid along the entire trajectory, but only from one surface/detector to the next one.

- As mentioned above, the Kalman filter with its associated smoother gives optimal estimates anywhere along the track and not only at a reference surface (which is often chosen to be close to vertex). This makes it easy to obtain optimal predictions in the outer detectors or detectors lying somewhere in between the tracking detectors. Thus, KF provides a natural way to prepare for the track matching between two neighboring detectors (in our case, TPC-ITS, TPC-TRD matching).

ments are available. There are different ways to parameterize the trajectory. However, one needs to choose a parameterization such that the track model can be approximated in the neighbohood of the measurement vector by a linear model sufficiently close to the real track from one surface/detector to the next one. See Section 3.4.2.

- The ability to obtain smoothed predictions at any detector layer enables KF to efficiently resolve and remove outliers, i.e. measurements not belonging to the track to be fitted.

- The KF formalism allows one to perform a geometrical fit to a charged track, in such a way that the measurements are included one after another along the trajectory. This feature may be used to merge in an unique recursive algorithm the track finding and the least-squares fit of the geometrical parameters (coordinates, angles, curvature).

- In the case of substantial multiple scattering (which is the case for most of the low-momentum tracks), track measurements are correlated, and therefore large matrices (of the size of the number of measured points) need to be inverted during a global fit. This is not the case for the Kalman filter which requires the inversion of 5 x 5 matrices (although in many cases their number of inversions is equal to the number of measured points), and thus renders the algorithm much faster.

- The formalism includes in a natural way the effects of multiple scattering and energy loss.

However, the Kalman filter relies on sophisticated space point reconstruction algorithms (including unfolding of overlapped clusters) and on the determination of good seeds to start a stable filtering procedure. Moreover, its efficiency cannot be better than the efficiency of the initializing algorithm.

We have seen that in ALICE we require good reconstruction efficiency and reconstruction precision. Given that some of the ALICE tracking detectors (ITS, TRD) have significant material budget, one can neglect neither the energy loss nor the multiple scattering. There are also rather big dead zones between the tracking detectors and this complicates finding the continuation of the same track in the next detector.

The implementation of the Kalman filter in the TPC will be introduced in more detail in Section 3.4.2. In the next section we will present the general strategy for track reconstruction in ALICE.

3.3 Track reconstruction strategy in ALICE

As mentioned previously, the baseline for the track reconstruction in ALICE is the Kalman filter. As such, the reconstruction begins with cluster finding in all of the ALICE detectors. It is worth mentioning that both cluster finding and track finding procedures have some detector specific features. Moreover, within a given detector, due to high occupancy a big number of clusters from different tracks overlap. As a result, the cluster finding and the tracking are not completely independent. As we shall discuss in Section 3.4.1, the cluster unfolding is done at the tracking step when knowledge of the parameters of the tracks that produced the clusters is available.

The overall tracking strategy starts with seeding in the outermost pad rows of our main tracker, the TPC, where tracks are better separated. As we need to reconstruct both particles coming from the initial collision and particles that are result of decays, seeding is done by searching with or without vertex constraint all sets of compatible points in different combinations of pad rows. Typically, more than one pass is done, starting with a rough vertex constraint, imposing primary vertex with a resolution of few cm, and then relaxing it. By imposing primary vertex with resolution of few cm (size of beam pipe), we make sure we account for multiple scattering and do not lose the tracks coming from decays inside the beam pipe. Relaxing the constraint allows us to seed the tracks from decays that took place far from the interaction point. Because of the small number of clusters assigned to a seed, the precision of its parameters is not enough to safely extrapolate it to the other detectors. Therefore, we propagate the track candidates towards the smaller TPC radii and, whenever possible, new clusters are associated with the track candidate in a 'classical'[3] Kalman filter way which will be detailed in the following sections. Once the inner limit of TPC is reached, tracks are extrapolated to the outer ITS layers and tracking in the ITS takes over. During a first pass in the ITS, we impose a rather strict vertex constraint with a resolution of the order of ~ 100 μm or better. The position of the primary vertex is reconstructed from space points in the two pixel layers of the ITS [233, 234]. The second pass in the ITS is done without vertex constraint in order to reconstruct the tracks coming from the secondary vertices well separated from the interaction point. Tracking proceeds layer by layer through the ITS until all the layers are used. At each layer a choice has to be made regarding which point to include next. Often more than one point satisfy the selection criteria, and choosing the best point in the next layer is not always the best strategy, as this can lead the process astray due to misidentified cluster. Therefore, a small number of choices has to be considered in parallel so that in the end we select only the one that, when all layers have been considered, gives the best fit. Thus, the algorithm builds a hypothesis tree before the final decision is taken. For details, see Section 5.1.4 in [186].

At this point we have the best estimates of the track parameters and their covariance matrix in the vicinity of the interaction point. According to well-known statistics theorems (see [235]), the uncertainties on the parameters of the track, i.e. correlation matrix, diminish as more points are added. This means that the track parameters are best known at the vertex and the uncertainty is highest in the outer layers of the TPC where we started. This is why at this point we proceed with the Kalman filter in the opposite direction, i.e. outwards. During this second propagation we remove from the track fit the space points with a large χ^2 contribution. In this way, we obtain the track parameters and their covariance matrix at the outer TPC radius. For the tracks labelled by the ITS tracker as potentially primary, several particle mass dependent time-of-flight hypotheses are calculated. These hypotheses are then used

[3] In its robustified version, the Gaussian-sum filter, both the measurement error and process noise are described by a sum of two Gaussian components, the mean value of each component being given by a Kalman filter. For details, see [230, 231, 232].

for particle identification with the TOF detector [186]. Once the outer radius of the TPC is reached we continue the Kalman filter into the TRD detector and then we propagate the tracks towards the outer detectors: TOF, HMPID and PHOS. Tracking in TRD is done in a way very similar to the one in TPC. After the matching with the TOF, HMPID and PHOS, the tracks acquire additional particle identification (PID) information.

Finally, all the tracks are refitted with the Kalman filter inwards to the primary vertex or to the innermost possible radius for the case of the secondary tracks. Tracks that passed the final refit pass and meet certain selection criteria are used for the secondary vertex (V^0, cascade, kink) reconstruction. The possibility to reconstruct the secondary vertices 'on the fly' during the tracking itself is implemented as well. The potential advantage of this latter option consists in the fact that tracks coming from a secondary vertex are not extrapolated beyond the vertex, thus minimizing the risk of picking up a wrong track prolongation.

The ITS has also a standalone tracking capability, which is very important for high momentum tracks going entirely inside the dead zones between the TPC sectors, tracks decaying between the ITS and the TPC, and for the low momentum tracks that do not reach the inner layers of the TPC. The standalone tracking algorithm in the ITS removes from the pool the points assigned to tracks found by the combined TPC-ITS tracking and starts the seeding from the two innermost layers (pixel layers) using a vertex constraint. A Riemann fit [236, 237] which takes into account the multiple scattering in the beam pipe will then provide the initial estimate for the state vector and covariance matrix. Once a seed is found, tracking proceeds towards the outer layers with a Kalman filter. For high-p_T tracking in ITS standalone mode, a neural network algorithm is also in place [238].

The tracking algorithm for the MUON spectrometer, which is another important tracking system in ALICE that measures precisely the muon momenta downstream the front absorber, is based on a Kalman filter as well [239]. Due to the dense front hadron absorber, the angular information is practically lost, and we have to impose a vertex constraint in order to obtain the angles.

The reconstructed tracks (together with the PID information), kink, V^0 and cascade particle decays are then stored in the Event Summary Data (ESD).

3.3.1 Implementation strategy

As we have mentioned in Section 3.1, the reconstruction algorithms need to be flexible. The tracking algorithms, written in C++ in the AliRoot framework, use common interfaces for different detectors. The design of the reconstruction program is modular in order to exchange and test easily various parts or versions of the algorithm. This modularity also allows us to use the same reconstruction program with different data: real data and MonteCarlo data, be it the detailed simulated detector response or just smeared positions of the hits in the detector as given by the GEANT transport code [240, 241] (the latter one is very useful for testing and debugging the reconstruc-

tion code). It is worth mentioning that exactly the same software is to be used for reconstructing both pp and Pb–Pb events. However, some of the program parameters can be tuned to a given track multiplicity.

The reconstruction software for the ALICE central tracking detectors shares a common convention on the used coordinate system. All clusters and tracks are always expressed in some local coordinate system related to a given sub-detector (TPC sector, ITS module, etc.). This local coordinate system is defined as following:

- It is a right handed Cartesian coordinate system;
- Its origin and the z-axis coincide with the ones of the global ALICE coordinate system[4];
- The x-axis goes perpendicular to the sensitive planes of the sub-detector (e.g. TPC pad row).

Such a choice reflects the symmetry of the ALICE setup and therefore simplifies the reconstruction equations. It also enables the fastest possible transformations from a local coordinate system to the global one and back, since these transformations become simple single rotations around the z-axis.

3.4 Track reconstruction in TPC

3.4.1 Cluster finding

As we have chosen a classical approach for track reconstruction, before tracking itself can start, two-dimensional clusters in the pad-row time planes need to be found. The reconstructed positions of the clusters are interpreted as the crossing points of the tracks and the centers of the pad rows. Typically, a region of 5×5 bins in z (drift) and y (pad) directions around the central bin with maximum amplitude is investigated. This region is bigger than the typical size of a cluster, which is $\sigma \sim 0.75$ bins in both directions.

Reconstruction of the cluster position: The position of a cluster is reconstructed as its center of gravity (COG). As discussed in Section 2.3, the COG of a cluster, as well as the cluster width, is affected by several stochastic processes and systematic distortions induced in turn by the charge threshold value (for details, see [212]). To correct for the threshold effect, the signals below threshold are replaced by a virtual charge according to some interpolation (which takes into account the pad response function of the readout chamber). If the virtual charge is above the threshold value, the amplitude of the signal is set to the threshold value. The COG position thus obtained is less sensitive to gain fluctuations. The cluster width is then used for

[4]The global frame is defined as a right handed Cartesian system with the origin in the center of the L3 magnet, z-axis along the beam and in direction opposite to the MUON arm, and y-axis going up.

the calculation of the cluster position errors and for tagging clusters that potentially overlap. For details, see [212].

Parametrization of the cluster position errors: The main contribution to the measurement errors is given by diffusion, gas gain fluctuations, angular effect and secondary ionization fluctuations. For details on the quantitative description of these effects on the accuracy of position measurement, we refer to Ref. [212].

Here we only mention that the errors of the cluster position depend on parameters (e.g. the track inclination angles) which require knowledge about the track. Therefore, the calculation of the clusters position errors is done during the track finding. An additional correction for the cluster shape and the relative distortion caused by cluster overlaps is also applied during the track finding. Details can be found in [242].

Cluster unfolding: As the expected occupancies reach 50% in the inner sectors of the TPC and about 20% in the outer sectors, clusters from different tracks may overlap. As a result, a certain number of clusters is lost and the others can be significantly displaced. These displacements are strongly correlated depending on the distance between the tracks and they are very hard to take into account.

To reduce the impact of the overlapped clusters on the track reconstruction we try to unfold the clusters having several local maxima. We use a fast spline method for this and require the charge to be conserved. Overlapped clusters are assumed to have the same r.m.s., which is equivalent to same track angles. If this assumption is not fulfilled tracks diverge very rapidly. As additional criterion for unfolding one can use the cluster asymmetry. The unfolding algorithm is described in [242]. Here, we note only that in order to trigger the unfolding using the shape information, additional knowledge about the track and the mean cluster shape over several pad-rows is needed. This information is available only during the track finding procedure which is introduced in the next section.

3.4.2 Track finding

In this section we discuss the track reconstruction in the TPC. First, we introduce the track model and the Kalman state vector, and then we detail the seeding algorithm and present briefly the track following procedure. For the interested reader, the transport of track parameters is being discussed in detail in Appendix A.4, see A.4.1-A.4.4.

Track model

The track model is, in general, the set of solutions of the equations of motion which describe the influence of the Lorentz force that is exerted by the magnetic field on a moving charge. In the Kalman filter, the track model is the linear expansion of this set of solutions; it maps the state vector space into the measurement space.

Equations of motion The trajectory of a charged particle in a static magnetic field is described by the following equation of motion:

$$d^2\vec{x}/ds^2 = (kq/p) \cdot (d\vec{x}/ds) \times B(\vec{x}(s)), \tag{3.1}$$

where s is the path length, k - a constant, q - the signed charge of the particle, p - the absolute value of the momentum of the particle and B the static magnetic field.

Since the TPC is placed inside an almost homogeneous magnetic field with the main magnetic field component along the z-axis parallel to the beam direction, the general solution is a helix with the axis parallel to z.

Choice of track parameters At a given location along the track, the helix can be factorized in two components: a circle in the transverse plane and a straight line in the path length vs. z plane. Obviously, for many purposes it is useful to parameterize the helix in terms of track parameters. The y and z dependent variables are thus most conveniently expressed as coordinates of the intersection point of a track and a pad row at a given x coordinate and are given by the equations:

$$y(x) = y_0 - \frac{1}{C}\sqrt{1-(Cx-\eta)^2} \tag{3.2}$$

$$z(x) = z_0 - \frac{\tan\lambda}{C}\arcsin(Cx-\eta), \quad \eta \equiv Cx_0, \tag{3.3}$$

where C (see Fig. 3.1) is the curvature of the track projection on the pad plane, λ is the 'dip' angle between the track and the pad plane, (x_0, y_0) are the coordinates of the center of the curvature of the track projection on the pad plane, and $z_0 \equiv z(x_0)$. The track 'state vector' x^{T} used in the Kalman filter calculations is then chosen as

$$\mathbf{x}^{\mathrm{T}} = (y,\ z,\ C,\ \tan\lambda,\ \eta)$$

With this choice of track parameterization, only two of five components of the state vector, namely the local track position y and z, change as the track is propagated from one pad row to another. When a track is leaving a sector and enters another one, the coordinate system is rotated and three components (y, z, and η of the state vector have to be changed. However, in the worst case this happens 2-3 times per track and the majority of tracks, being contained entirely within the same sector, do not require this transformation at all (see Fig. 3.1).

The track model assumed for the first stage of the reconstruction in TPC corresponds to the one of the pion, i.e. calculation of energy loss and multiple scattering effects assumes the pion mass.

Starting tracks

As mentioned in Section 3.2, Kalman filter relies on the determination of good initial approximation for the track parameters and their covariance matrix (track seeds). Since none of the other detectors have so far been able to provide seeds for the track reconstruction in TPC, the seed finding is done using the TPC data. Given that this is a very important part of the whole reconstruction chain, particularly kink reconstruction, we give a detailed description of the seeding procedure.

The seed finding strategy follows the necessity to reconstruct not only primary particles which cross the whole TPC but also particles which decay, like V^0 and K. Therefore two different seeding strategies are used, namely seeding with primary vertex constraint and seeding without any vertex constraint. Obviously, the direction of the filter runs from the outermost pad rows where the tracks are better separated, towards the innermost pad rows. We recall that the occupancy reaches 50% in the innermost pad rows. The smallest sets of points, compatible to the shape of the trajectory, needed to start the tracks are triplets of points in three different pad rows. As it will be shown below, they are first built using rough compatibility criteria and next selected with a helix fit.

The first seed finding is done with vertex constraint. It begins with a search of all pairs of points at a pad row i and a pad row j closer to the interaction point ($i-j=20$ at present), which can project to the primary vertex. For each point at the outer pad row i, points at the inner pad row j are checked only within a certain window in the (x,y)-plane, defined by some p_T cut-off, and a certain window in the z-direction defined by the requirement of pointing to the primary vertex. The size of the windows was tuned to render the algorithm fast[5] and yet give good efficiency and allow the recognition of low-p_T tracks (with large angle with respect to the radial direction). A too large window would lead to an unwanted large increase in the number of possible combinations.

When a reasonable pair of clusters is found, parameters of a helix going through these points and the primary vertex are calculated, and the occurrence of a cluster near the crossing point of this helix and a 'middle' pad row $k = j + (i-j)/2$ is checked. If such a cluster is found, the parameters of this helix are taken as an initial approximation of the parameters of the potential track. The corresponding covariance matrix is evaluated using the point pair errors and applying some big uncertainty to the primary vertex position (see Fig. 3.1 for a schematic view). This is the only place where a certain (not too strong) vertex constraint is introduced. Later on, tracks are allowed to have any impact parameters at primary vertex both in the z-direction and in the (x,y)-plane.

Using the calculated helix parameters and their covariance matrix the Kalman filter is started from the outer pad row i to the inner pad row j. We divide the interval $i-j$ into 2 subintervals. If in each subinterval at least half of the possible clusters between the initial ones were successfully associated with this track candidate, it is saved as a 'seed' and we continue to look for another pair of initial points. The number of possible clusters is considered to be equal to the number of track crossings with the pad rows when the track is not in a dead zone.

Being efficient for the primary tracks, the seed finding with the vertex constraint obviously penalises the secondary tracks. Thus, an algorithm for track seeding without vertex constraint is necessary. Taking into account that for low-p_T tracks the effect

[5]For the same reason, the data structures are organized such that there is a straightforward access to clusters ordered according to their z-coordinate position and belonging to the same pad row.

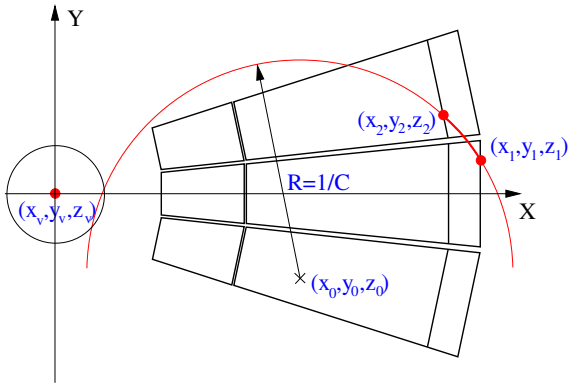

Figure 3.1: Track finding coordinate system, track parameters and the schematic view of seeding with the vertex constraint.

of cluster sharing between pad rows is non-negligible, and thus the cluster position distortions between neighbouring pad rows are correlated, the algorithm seeks to use uncorrelated clusters. For each pair of clusters selected at pad row i and within some window at the pad row j ($i - j = 7$ in this case) respectively, the algorithm tries to find a third cluster at the 'middle' pad row $k = j + (i - j)/2$ near the crossing between the pad row k and the straight line connecting the two clusters selected at the pad rows i and j. If such a cluster is found, a helix is fit to the cluster triplet. Using the calculated helix parameters and their covariance matrix the Kalman filter is started from the outer pad row i to the inner pad row j. If at least 75% of the possible clusters were successfully associated with the track candidate, the Kalman filter is run further to the inner pad row $j - 20$. If at least half of the possible clusters were successfully associated with the track candidate, it is saved as a 'seed'.

For both seed finding approaches the sizes of the windows are fixed such as to find the best compromise between efficiency, p_T cut-off and speed of the algorithm. With 9 measurements and 5 parameters one has 4 constraints to check whether the triplet belongs to the same helix trajectory. We cut on the z residual (checking that the points of the triplet are roughly aligned in z), which is the most sensitive quantity when the triplets belong to pad rows far apart:

$$z^{extrap} = z_1 - \frac{z_1 - z_3}{x_1 - x_3} \cdot (x_1 - x_2), \qquad |z^{extrap} - z_2| < z_{max}, \tag{3.4}$$

where the typical value of the parameter z_{max} is about 3 cm. Also, to avoid unnecessary calculations, we do not compute the helix parameters if the estimated curvature exceeds a certain value (p_T cut-off), or if the estimated angles defining the slope parameters of the helix exceed certain values. These cuts vary according to the depth of the pad row i for which the seeding procedure is initiated.

The efficiency of the seeding can be increased by repeating the procedure starting at different pad rows i. However, as some of the tracks are very close to each other on

a long path the seeding at different pad rows cannot be considered as independent. The efficiency quickly saturates at some (less than 1) value. Another problem with repetitive seeding is that occupancy increases towards the lower pad row radius and thus the efficiency of a single seeding is a decreasing function of the pad row radius. Nonetheless, to maximize the track finding efficiency for secondary tracks, particularly for kinks, it is necessary to perform almost 'continuous seeding' inside the sensitive volume of the TPC. This is mainly due to the fact that in the high track density environment it is almost impossible to start tracking of the primary particles which decay using only the last point of the secondary track because this point is not well defined. Therefore, for kink finding, seeding in the innermost pad rows should be performed. On the other hand, to find the secondaries from kinks or V^0 decays, it is mandatory to make a very efficient seeding in the outermost pad rows. Thus, to optimize the efficiency and keep the computing resources within the required limits, we have adopted the following strategy for seeding and implicitly track reconstruction:

- Reconstruction of tracks seeded with vertex constraint :

  Three seedings in the outermost pad rows in steps of 6 pad rows with a cut on curvature corresponding to $p_T > 200$ MeV/c.

  Nine seedings in the outermost pad rows in steps of 6 pad rows with a cut on curvature corresponding to $p_T > 500$ MeV/c.

  Ten seedings scanning the full TPC in steps of 10 pad rows towards the innermost pad row with a decreasing p_T cut.

- Reconstruction of tracks seeded without vertex constraint :

  Three seedings starting at the three outermost pad rows. This is done in order to maximize the kink finder efficiency.

  Six seedings is steps of 5 pad rows.

  Five seedings scanning the outer sectors in steps of 10 pad rows towards the innermost pad row with a decreasing p_T cut.

After each seeding procedure the track candidates are followed inwards to the innermost pad row of the TPC. The reconstructed tracks are classified according to their quality. The quality parameter is defined by the normalized χ^2 and the ratio of the number of found clusters to the number of possible clusters. The mean value and the sigma of the distribution of the quality parameter are then calculated. The clusters assigned to a track are marked if the track quality parameters do not deviate from the mean value by more than 3 sigmas. The marked clusters are not used in the subsequent seedings but they still can be assigned to other tracks during the track following.

Following tracks

The procedures described below are repeated for all track candidates, for each seeding procedure, until the innermost pad row of the TPC is reached or the track is lost.

Extrapolating tracks. Having the current estimation of the track parameters on the k-th row, its vector state and covariance matrix are extrapolated to the next (i.e (k+1-th) pad row according to the Kalman equations A.3 by means of track model and by error propagation respectively. Details of calculations are given in Appendix A.4.1. During this step, the effects of multiple scattering and energy loss are taken into account at the new track position.

From time to time it happens that the track leaves a TPC sector and enters another. In this case we recalculate the track parameters and the covariance matrix so that they are always expressed in the local coordinate system of the sector within which the track is at the moment.

Selecting a measured point on the $(k+1)$-th pad row. Once the track was extrapolated to the $(k+1)$-th pad row, we define a window around the extrapolated point, along the pad row direction, inside which we look for a cluster to be associated with the track. The width of the window, now much narrower than in step 3.4.2, is set typically to $\pm 4\sigma$, where σ is calculated taking into account the track position errors given by the track parameter covariance matrix and the expected cluster position errors, and some safety factor to account for possible cluster overlapping (see discussion in Section 3.4.1 and [242]).

After the window is defined we check all clusters which appear within it and select[6] the point nearest in the $y-z$ projection to the extrapolated track position. If no point exists in the window, a missing point is counted and the track will be extrapolated to the next, i.e. $(k+2)$-th, pad row. Otherwise, once the nearest cluster is found, we use a set of filtering conditions deduced from practical experience to decide if the point will be accepted or not. Thus, we first estimate cluster position errors with some additional correction for the cluster shape and to account for possible cluster overlapping (see again discussion in Section 3.4.1 and [242]). The cluster is accepted if the residuals in both directions are smaller than 3σ of the estimated uncertainty, and then the track parameters and their covariance matrix are updated according to the filtering equations A.4-A.5. Evidently, if the residuals exceed 3σ a missing point is counted and the search for a new point continues inwards.

If points are missing on too many pad rows in the sensitive region of the TPC the track is stopped, else these steps will be repeated until the innermost pad row. During the backward following, if a point was missing on this pad row, the newly selected point is added under the same filtering conditions as above.

[6] All clusters are ordered according to their z-coordinate and the clusters within the window are quickly selected with a binomial search.

Closing tracks

If there are no clusters associated to the track candidate trajectory on several pad rows in the sensitive region of the TPC, the track hypothesis should be removed. Given that it is not known a priori if a given track is primary or secondary, this criterion is not the optimal choice. A different selection criterion, the local cluster density, was defined as the ratio of the number of accepted clusters to the number of possible clusters in a region of several pad rows. Since secondary tracks may have low cluster density, tracks with low local cluster density are not completely removed. They are removed only if the local cluster density corresponding to a certain length interval measured from the point where the track was started is below a specified value (typically 0.8); otherwise they are only marked and left for subsequent analysis. Very short tracks (with fewer than 15 clusters) are removed as well.

Since the same track can potentially be seeded many times, an additional value, the track overlap factor, is defined as the ratio of the clusters shared between two track candidates and the total number of clusters on the track. If for two track candidates the overlap factor is bigger than some value (currently 0.6), the track candidate with higher χ^2 or lower number of assigned clusters is removed. This is a compromise between the maximal track finding efficiency and the minimal number of multiply found tracks.

3.5 Tracking performance

In this section we shall address the behaviour of some parameters of the track reconstruction in TPC that are relevant for reconstruction of decay topologies, and we will show how these parameters change when we include the information from the other tracking detectors (ITS, TRD) in the barrel. More details and results of the tracking performance are to be found in Ref. [186].

3.5.1 Performance of the TPC track finding

Track finding quality. To check the effect of particle density on the tracking performance we inspect the ratio of the number of clusters associated to a track to the number of pad rows crossed by this track and the pulls in the transverse momentum as a function of particle transverse momentum.

Figure 3.2 shows the ratio of the number of clusters associated to a track to the number of pad-rows crossed by this track for pp and central Pb–Pb ($\mathrm{d}N_{\mathrm{ch}}/\mathrm{d}\eta = 6000$) collisions. One can see that due to cluster overlaps, for high track densities the tracks start losing clusters. However, the percentage of associated clusters is still rather high and as shown in Fig. 3.3, the pulls[7] in the transverse momentum are distributed

[7] The pull of a track parameter is defined as the difference between the reconstructed and the true (generated) value of the parameter divided by the estimation of the corresponding error. Under ideal conditions the pulls are distributed normally (i.e. with zero mean and sigma equal to 1).

practically normally.

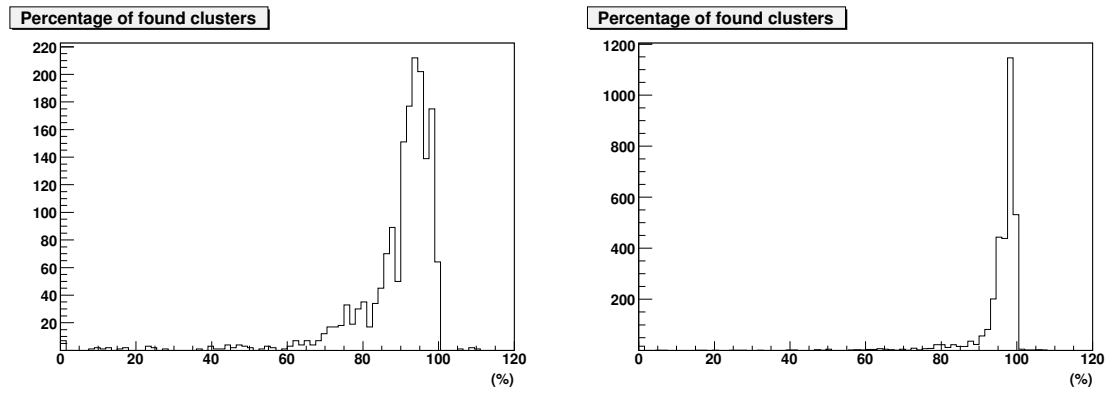

Figure 3.2: Ratio of the number of clusters associated to a track to the number of pad-rows crossed by this track. Left: central Pb–Pb collisions ($\mathrm{d}N_{\mathrm{ch}}/\mathrm{d}\eta = 6000$). Right: pp collisions.

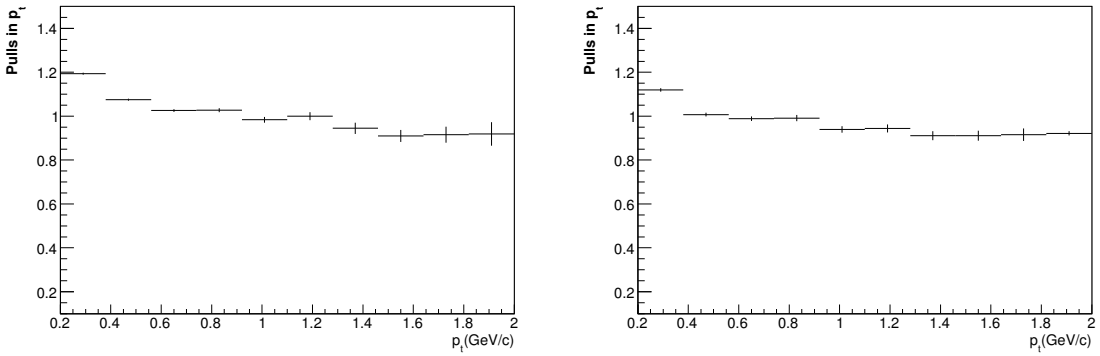

Figure 3.3: Pulls in track momentum as a function of particle transverse momentum. Left: central Pb–Pb collisions ($\mathrm{d}N_{\mathrm{ch}}/\mathrm{d}\eta = 6000$). Right: pp collisions.

Track finding efficiency We define two types of track finding efficiency: the track finding efficiency of the software algorithm and the 'physical' efficiency. The latter one includes also all the other factors like dead zones in the detectors, inefficiency of the electronics, decays, energy loss and interactions with the material, that are not included in the definition of the efficiency of the algorithm.

The software track finding efficiency is defined as the ratio of the number of 'good found' tracks to the number of trackable or 'good generated' tracks, while the probability to produce a fake track is expressed by the number of 'fake tracks' normalized in the same way. For TPC, we are using the following definitions:

- A 'good generated' track is a track which crosses at least 50% of all pad rows.
- A 'good found' track is a track with the number of assigned clusters larger than 50% of the number of crossed pad rows. In addition, we require that more than 90% of the assigned clusters belong to this track and at least half of the innermost 10% of clusters are assigned correctly.
- If the requirement on the number of assigned clusters is satisfied but the requirements on the number of correctly assigned clusters are not satisfied, the track is considered as 'fake found'.

The physical track finding efficiency is defined as the ratio of the number of tracks reconstructed with the pulls in momentum and the two emission angles less than 4 to the number of tracks that were generated within the beam pipe and emitted within the TPC acceptance. Here we show only the dependence of the physical track finding efficiency on the azimuthal angle ϕ within a TPC sector (left panel of Fig. 3.4) and the dependence on the radial position of the particle vertex (right panel of Fig. 3.4) for central Pb–Pb collisions.

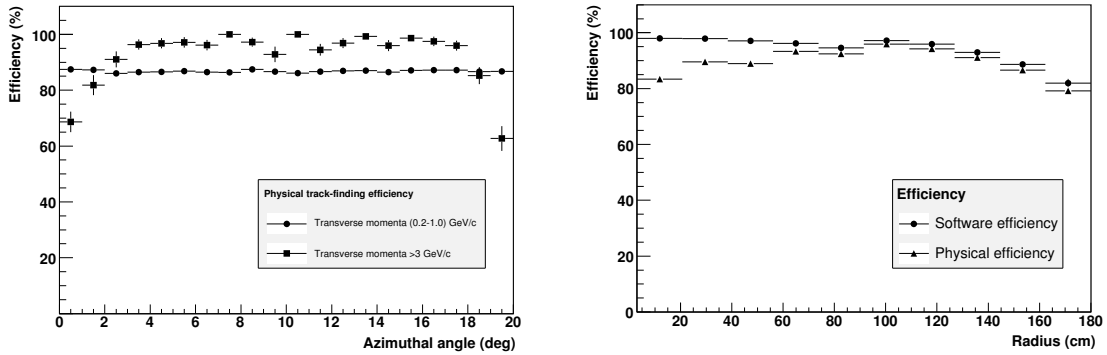

Figure 3.4: Physical TPC track finding efficiency as a function of the track azimuthal angle within a TPC sector (left) and as a function of particle vertex position (right) for central Pb–Pb collisions ($\mathrm{d}N_{\mathrm{ch}}/\mathrm{d}\eta = 6000$).

When a high momentum track goes near the edge of a sector a big part of the track is hidden in a dead zone. Thus, the probability to miss such a track is high. The low momentum tracks are less affected by dead zones because in this case only a small part of the track becomes lost in a dead zone. However, the situation is a bit different for tracks that are products of decays in the TPC. One can see from the right panel of Fig. 3.4 that starting with $R \sim 100$ cm the efficiency goes down as the vertex position of the charged decay product goes up. For a short track, the part of the track hidden in the dead zone between the TPC sectors can represent a significant part of its length. It is noteworthy that starting from $R \sim 85$ cm corresponding to the TPC

lower radius, the tracking efficiency follows the physical efficiency. The drop of the physical track finding efficiency towards the smaller radii is due to energy loss and interactions in the material between the TPC and ITS. We recall that the outermost layer of the ITS is at R=44 cm.

No significant dependence of the software track finding efficiency on particle transverse momentum has been found, see Fig. 3.5. Even in the high track-multiplicity environment, the efficiency is close to 100% practically everywhere and goes down only in the low momentum region $p_T < 0.2$ GeV/c. More details can be found in [186].

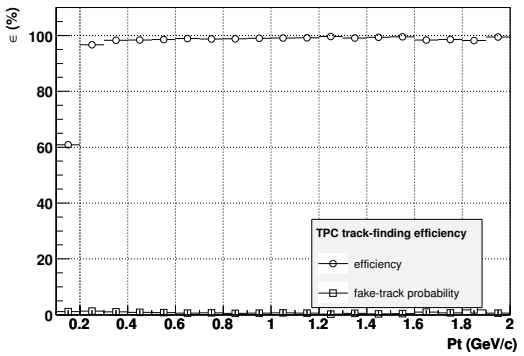

Figure 3.5: Efficiency of the TPC track finding software as a function of particle transverse momentum for central Pb–Pb collisions ($\mathrm{d}N_{\mathrm{ch}}/\mathrm{d}\eta = 6000$).

Momentum and angular resolutions As we shall discuss in Chapters 4 and 5 the angular and momentum resolutions are important parameters for the selection of decay topologies and for the measurement of p_T distribution of the decaying particle. Moreover, given that before decaying the meson will cross only a fraction of the pad rows of the TPC, the momentum resolution discussed here represents the lower bound for the momentum resolution of the decaying mesons reconstructed with TPC standalone.

Figure 3.6 shows the relative transverse momentum (left) and dip angle (right) resolutions, as a function of the transverse momentum for central Pb–Pb collisions. The dependence is shown for the low-momentum region where the contribution from multiple scattering is dominating. We can mention that the difference in resolutions for the two limiting cases of pp and Pb–Pb collisions is negligible, see [186].

Considering the importance of momentum resolution, it is useful to cross-check the theoretical expectation for the momentum resolution with the result coming from the detector simulation in the case of pp collisions. The transverse momentum resolution can be approximated as a quadratic sum of a contribution due to the multiple scattering and a contribution due to the detector resolution. If the relative resolution is considered, the first contribution is a constant and the second is proportional to

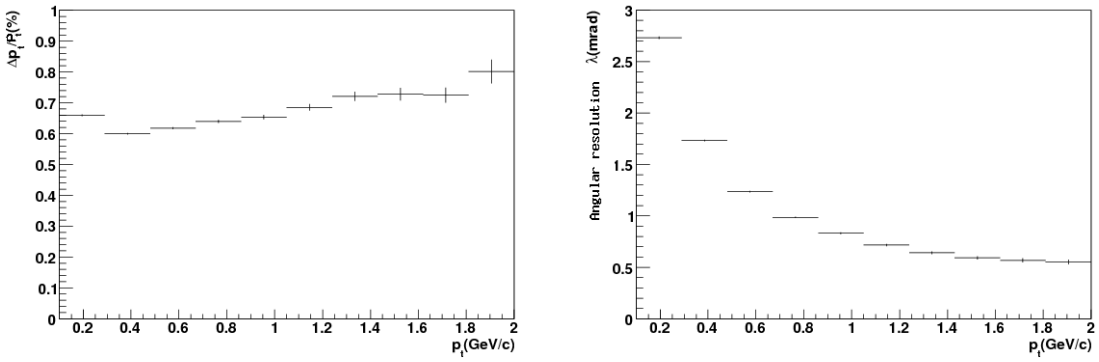

Figure 3.6: Momentum (left) and dip angle (right) resolutions as a function of particle transverse momentum for central Pb–Pb collisions ($\mathrm{d}N_{\mathrm{ch}}/\mathrm{d}\eta = 6000$).

the transverse momentum itself [60]:

$$\frac{\sigma(p_T)}{p_T} = K_{scatt} \oplus K_{meas} \cdot p_T \equiv \sqrt{K^2{}_{scatt} + K^2{}_{meas} \cdot p_T}. \tag{3.5}$$

If p_T is measured in a solenoidal magnetic field B, with uniformly distributed points having the same spatial resolution, the term K_{meas} should be [235]:

$$K_{meas} = \frac{\sigma_{r\phi}}{0.3BL^2}\sqrt{\frac{720}{N+4}} \tag{3.6}$$

where N is the number of space points on the trajectory, $\sigma_{r\phi}$ is their spatial resolution in the transverse plane and L is the total visible track length. For our TPC, the value of K_{meas} calculated using $\sigma_{r\phi} = 0.8$ mm [196], $N = 100$, L= 1.6 m and $B = 0.5$ T, is about 0.548%. Note that in the TPC the spatial resolutions of the space points can be assumed constant only in the case of pp collisions. In the high-multiplicity environment of heavy ion collisions, the clusters overlap in the inner part of the detector and the resolution is worse than in the outer part [196].

The contribution due to the multiple scattering can be approximated as [243]

$$K_{scatt} = 0.045\frac{1}{B\sqrt{LX_0}} \tag{3.7}$$

where X_0 is the radiation length of the material crossed by the particles.

Assuming for simplicity that the drift volume of the TPC is filled with 100% Ne gas[8] (X_0=345 m), we obtain a value of 0.38% for K_{scatt}. Thus, for a particle with p_T=1 GeV/c, the relation 3.5 predicts a relative transverse momentum resolution of 0.66% which is in good agreement with the value 0.64% coming from the detector simulation.

[8] We recall that the drift volume of the TPC is filled with a $85\%\mathrm{Ne} + 5\%\mathrm{N}_2 + 10\%\mathrm{CO}_2$ mixture.

3.5.2 Performance of the combined track finding

Overall track finding efficiency The reconstruction quality of a track, notably the momentum resolution, improves with the addition of every detector which contributes to the reconstruction of this track. However, the track matching to the ITS and the TRD detectors is difficult because the distance between TPC and the sensitive elements of each of these two detectors is rather large and the tracks are crossing big amounts of material. Since a significant fraction of tracks which interact with this material either scatter and lose significant amounts of energy or may even be absorbed, the requirement for a track to be reconstructed in all the tracking detectors reduces the statistics of such tracks.

Although the overall software track finding efficiency is still rather high (about 90% practically at any p_T), the physics track finding efficiency is much more dependent on the number of the contributing detectors. From Fig. 3.7, one can see that the biggest loss of combined tracking efficiency happens in the TRD. This is true both for the case of high-multiplicity events (Fig. 3.7 left) and the case of pp events (Fig. 3.7 right). The reason is that, as discussed above, the physical efficiency is mainly defined by particle decays, the presence of the dead zones and the interactions with the material. We recall that the material budget of TRD is 14% of radiation length.

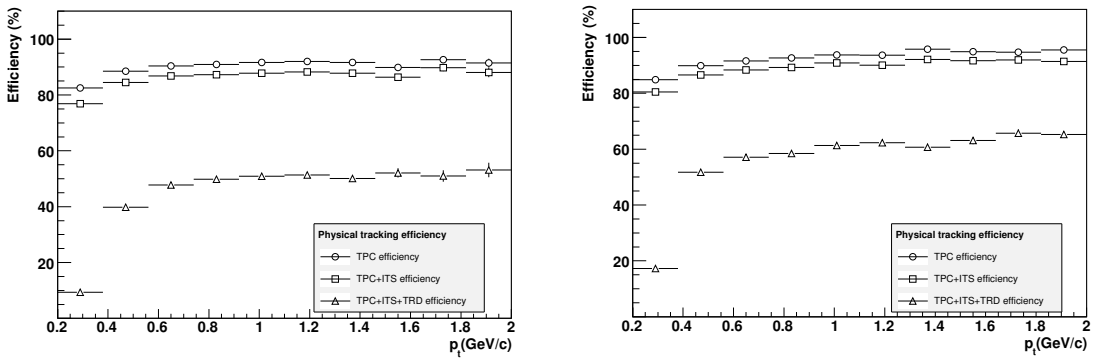

Figure 3.7: Physical track finding efficiency for different combinations of tracking detectors as a function of particle transverse momentum. Left: central Pb–Pb collisions ($\mathrm{d}N_{\mathrm{ch}}/\mathrm{d}\eta = 6000$). Right: pp collisions.

Obviously, due to the presence of dead zones, energy loss and the interactions with the material, the statistics of kaon decay topologies for which both mother and charged daughter can be tracked outside the TPC volume is diminished as well.

Overall momentum and angular resolutions Figure 3.8 shows the momentum resolution for different combinations of the tracking detectors. One can see that, despite the drop in efficiency, TRD improves the overall momentum resolution, especially at higher momenta.

The best overall momentum resolution is achieved for low track multiplicity events (pp collisions) and can be as good as $\sim 3\%$ at 100 GeV/c. This will, however, require very accurate corrections for the energy losses in the material and precise alignment of the TRD with respect to the TPC (see Fig. 3.8 right). It is noteworthy that the ITS+TPC curve sets the lower bound on the momentum resolution for the charged kaons identified via their kink topology with the combined tracking as, already mentioned, in the latter case kaons' total visible track length is shorter .

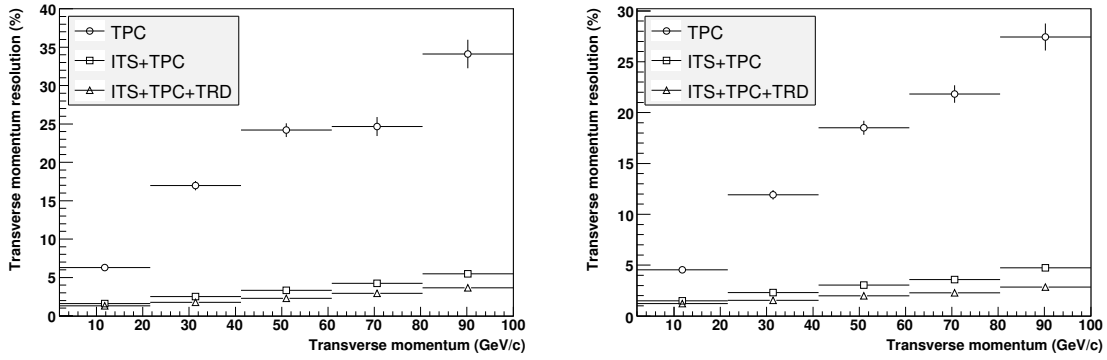

Figure 3.8: Transverse momentum resolution for combined track finding as a function of particle transverse momentum. Left: central Pb–Pb collisions ($\mathrm{d}N_{\mathrm{ch}}/\mathrm{d}\eta = 6000$). Right: pp collisions.

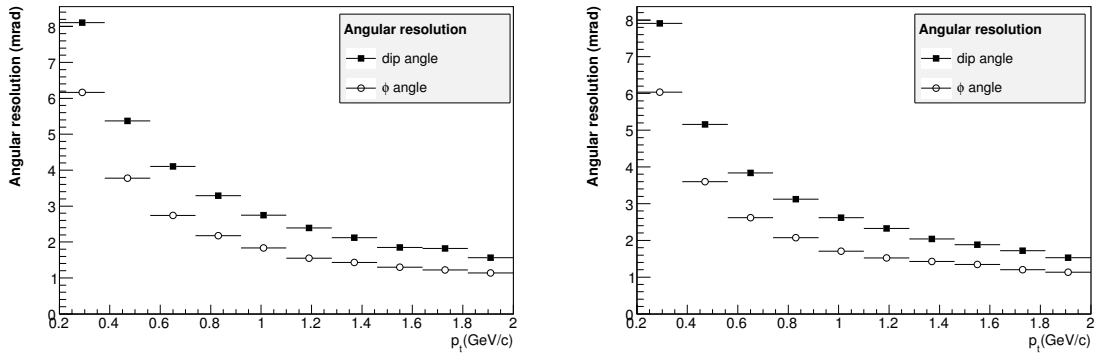

Figure 3.9: Angular resolution for combined track finding as a function of particle transverse momentum. Left: central Pb–Pb collisions ($\mathrm{d}N_{\mathrm{ch}}/\mathrm{d}\eta = 6000$). Right: pp collisions.

The overall angular resolution is shown in Fig. 3.9 for the central Pb–Pb events (left) and pp events (right). There is no significant dependence on the track multiplicity. The angular resolution is defined by the multiple scattering on the material

between the last space point assigned to a track and the primary vertex. The obtained resolutions are in good agreement with the ones that can be estimated from the thickness of the inner pixel ITS layer and the beam pipe. Note that for TPC stand-alone, at low-momenta, the angular resolution is better due to the fact that between the last space point assigned to a track and the primary vertex there is only the beam pipe material (the inner pixel layer adds about 1% radiation length of additional material).

At higher momenta, where the influence of multiple scattering becomes negligible, the angular resolution is defined by the space point precision of the contributing tracker detector. Given the high-resolution of the ITS detectors, the best results are achieved by combining the TPC and ITS together.

We demonstrate in Chapter 5 that the best kink parameters are achieved when we include in the reconstruction chain all the tracking detectors as well.

Chapter 4

Kink reconstruction

Kinks are topological signatures of 1-prong decays. The kink reconstruction technique is only used when the lifetime of the decaying particle is long and there is a high probability of the decaying particle leaving a signal in the tracking detectors. After a brief review of the basic ideas behind the kink reconstruction, we introduce the kink finder algorithm and discuss some of the main reconstruction requirements.

4.1 Kaons identification using the kink topology

There are various particle identification (PID) techniques employed so far for kaon identification over different p_T ranges, namely PIDs using in turn, measurements of specific ionization in the TPC and ITS at low momentum in the non-relativistic region where the energy loss curves for different particle species are well separated (see Fig. 4.1), time-of-flight with the TOF detector, Cherenkov angle with the HMPID detector. The TOF array and the HMPID detector can identify individual charged hadrons up to $\beta\gamma \approx 5-6$, i.e. kaons up to $p_T \approx 3$ GeV/c, where the energy loss curves cross each other and the $\mathrm{d}E/\mathrm{d}x$ information is ambiguous. In the relativistic region, i.e. $\beta\gamma > 5-6$, only pions and protons can be identified on a track-by-track basis with good efficiency and purity using $\mathrm{d}E/\mathrm{d}x$; kaons can only be measured indirectly on a statistical basis [186]. For details of the PID methods and results, we refer to Ref. [186]. Here only the results of charged kaons identification using the PID signals from the ITS, TPC and TOF as stand-alone detectors together with the result for the combined PID signals are shown in Fig. 4.2 to illustrate the kaon identification efficiency, purity and the momentum range achieved by combining PID signals from different detectors. The only way we can extend this momentum range is to try to identify the kaons through their decay topology.

With a significant kaon production at the LHC energies, owing to kaon's high branching ratio to the muonic decay channel (branching 63.26%) and to the large angular acceptance of the central part of ALICE, we will show that the reconstruction of the kink topology is a key technique for identifying kaons over a momentum range much wider than the one achieved by combining PID signals from different detectors.

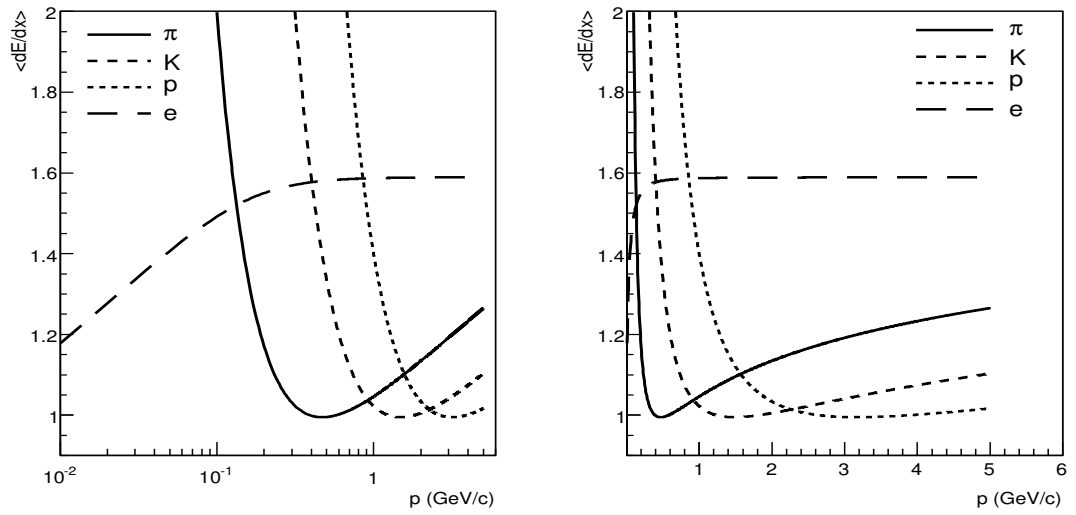

Figure 4.1: Momentum dependence of the mean energy loss ($\mathrm{d}E/\mathrm{d}x$) for pions, kaons, protons and electrons according to the parametrisation of the Bethe-Bloch formula adapted for the TPC [186]. The mean energy loss is normalized to unity for minimum ionizing hadrons.

4.1.1 Outline of the method

Kinks recognition relies on two effects rooted in the basic laws of momentum and energy conservation: first, it relies on the angle formed between the tracks of the decaying particle (parent) and of the emerging charged particle (daughter); secondly, it relies on the momentum difference between the parent and the daughter (the latter has nearly always a smaller momentum). Thus, if a decay occurs between detection elements k and $k+1$, we may expect that the state vector at k obtained from the track segment behind the decay is significantly different from the back extrapolation at k of the track segment in front of the decay. Obviously a kink can be reconstructed only if both track segments are detected in the tracking system and the decay vertex is found. Therefore we perform almost continuous combinatorial seeding with and without vertex constraint throughout the TPC. Details concerning the seeding strategy and the seeding algorithms themselves are given in Section 3.4.2.

The most frequent sources of kinks are the muonic decays of charged π- and K-mesons: $\pi \rightarrow \mu\nu$ (branching 99.98%), $\mathrm{K} \rightarrow \mu\nu$ (branching 63.39%). It is worthwhile mentioning that the $\mathrm{K} \rightarrow \pi\pi^0$ decay channel (branching 21.03%) is also a non-negligible source of kinks.[1] For simplicity, however, we shall limit our discussion

[1] Other sources of kinks are the $\mathrm{K} \rightarrow e\nu_e\pi^0$ (branching 4.93%), $\mathrm{K} \rightarrow \mu\nu_\mu\pi^0$ (branching 3.3%) and $\mathrm{K} \rightarrow \pi\pi^0\pi^0$ (branching 1.75%) decay channels. In order to identify the decay type one may use a kinematical fit method.

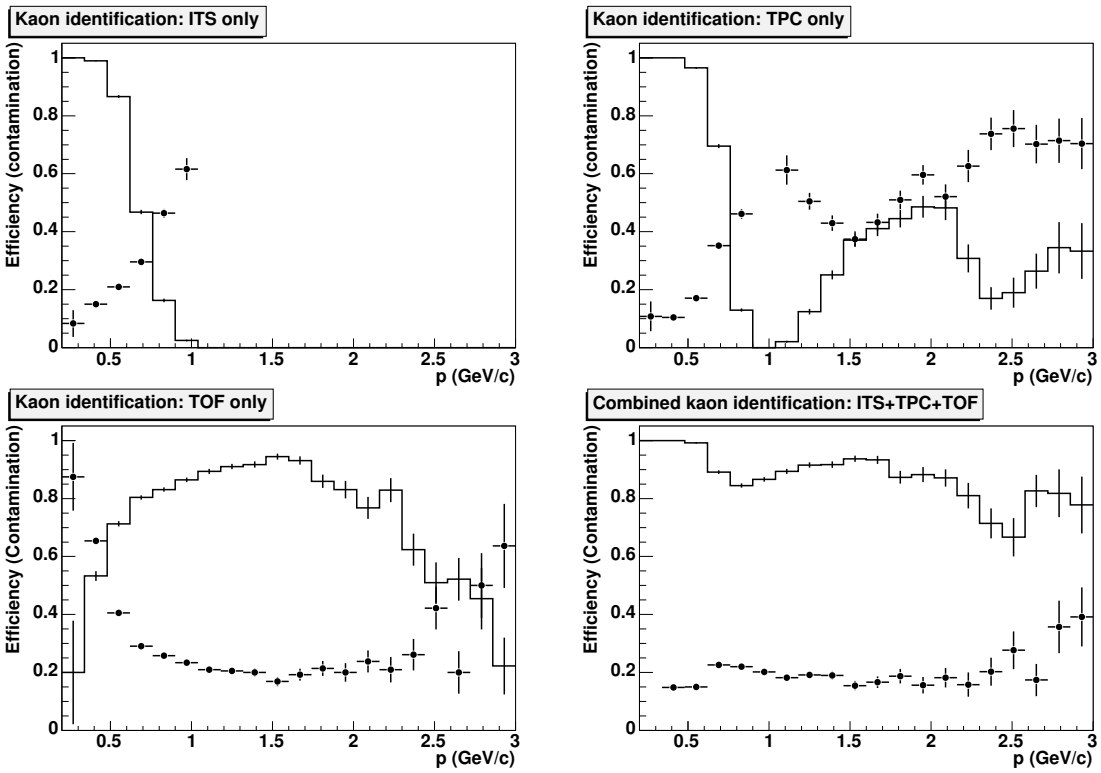

Figure 4.2: Single-detector efficiencies (solid line) and contaminations (points with error bars) of the charged kaon identification with the ITS, TPC and TOF stand-alone and the combined efficiency and contamination using all the detectors working together.

to the muonic decay channels as the method and the calculations given below can be extended in a straightforward manner to the case of $K \to \pi\pi^0$ decay.[2]

For a two-body decay like the π- and K-decay under consideration, there is a simple method of determining the decay angle and the momentum of a decay product, in this case a muon. In the rest system of the meson the decay is isotropic, which means that there is no privileged direction for either of the decay products. Thus, in this frame, the momentum vector $\mathbf{p}$ of the muon lies on a circle of radius p. Because of momentum conservation, the momentum vector of the neutrino equal $-\mathbf{p}$, and assuming the neutrino to be massless, from the law of energy conservation:

[2]Our tests showed that for the $K \to \pi\pi^0$ decay channel, the performance of the kink finding algorithm is similar to the one obtained for kinks produced by muonic decays. In this thesis, however, we shall present only the results for $K \to \mu\nu$ decay channel due to the fact that we do not have yet sufficient simulated data for the $K \to \pi\pi^0$ decay channel in order to estimate the total yield of reconstructed decays after one year of LHC data taking. The present study will thus give the estimate on the lower bound for the p_T-range over which we get usable statistics of identified kaons.

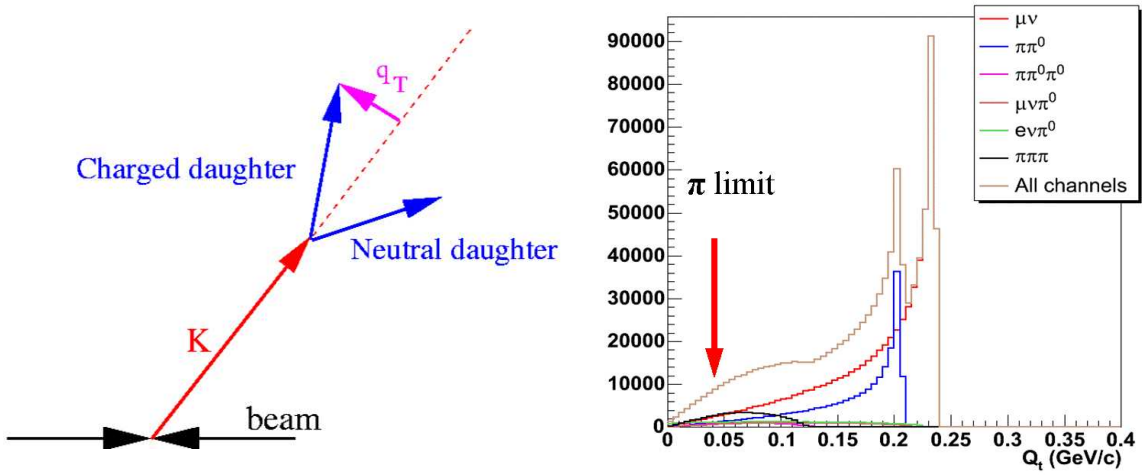

Figure 4.3: Left: Definition of the q_T-value of the charged daughter. Right: The q_T-value distributions of charged daughters for different kaon decay channels. The branching ratios were taken into account. The arrow indicates the q_T limit of the pion decays (30 MeV/c).

$$p = \frac{M^2 - m^2}{2M}, \tag{4.1}$$

where M is the meson mass and m is the muon mass. p can be expressed in terms of components of the muon momentum in the rest frame

$$p = \sqrt{q_T^2 + q_L^2}, \qquad \text{where} \qquad \begin{aligned} q_T &= p \sin\theta \\ q_L &= p \cos\theta \end{aligned}, \tag{4.2}$$

with θ being the decay angle in the rest frame, and q_L, q_T the components of $\mathbf{p}$ parallel and respectively orthogonal to the momentum vector $\mathbf{P}$ of the meson.

From Eq. (4.2) and Eq. (4.1) it is easy to see that due to their different masses, the maximum value of the transverse momentum of the daughter in the rest system of the decay, $(q_T)_{\max}$, differs strongly for K and π mesons. To be more specific, it is 30 MeV/c in the case of π-decay compared to 236 MeV/c in the case of K-decay. Therefore, we can use the q_T variable (see left panel of Fig. 4.3) as selection parameter to distinguish between K- and π-decays once we have reconstructed the kink topologies. The right panel Fig. 4.3 shows the q_T distributions of charged daughters for different kaon decay channels and the q_T limit for pion decays.

In the laboratory system, the components of $\mathbf{p}$ and the decay angle can be computed in a straightforward manner from the Lorentz transformation:

$$p_T^{lab} = q_T = p\sin\theta, \tag{4.3}$$
$$p_L^{lab} = \gamma q_L + \beta\gamma E = \gamma p\cos\theta + \beta\gamma E, \tag{4.4}$$
$$\tan\theta^{lab} = \frac{p_T^{lab}}{p_L^{lab}} = \frac{p\sin\theta}{\gamma p\cos\theta + \beta\gamma E}, \tag{4.5}$$

with:

$$\gamma = \frac{\sqrt{P^2+M^2}}{M}, \beta = \frac{P}{\sqrt{P^2+M^2}}, E = \frac{M^2+m^2}{2M}. \tag{4.6}$$

We recall that P is the momentum of the decaying meson. It is evident that the circle is transformed into an ellipse, its centre being at $\beta\gamma E$, and its half-axes being equal to p and γp respectively. Since the decay is isotropic in the rest system, $cos\theta$ is a random variable uniformly distributed in the interval $[-1, 1]$. One can notice from the above equations that the kink angle, θ^{lab}, is a function only of the $cos\theta$ and the momentum P of the decaying meson. To give an idea of the kink angle and momentum difference to be expected from the decay of a K meson, Fig. 4.4 shows the kink angle θ^{lab} and the momentum ${p_\mu}^{lab}$ of the muon as a function of $cos\theta$, for two values of the momentum of K: 2 GeV/c (top panel) and 30 GeV/c (bottom).

The maximum kink angle for a given momentum of the decaying meson can be calculated by maximising the equation for θ^{lab} given above with respect to θ. Thus, by imposing

$$\frac{d}{d(\cos\theta)} = 0, \tag{4.7}$$

we obtain:

$$(\theta^{lab})_{max} = \frac{p}{\gamma E}\frac{1}{\sqrt{\beta^2 - p^2/E^2}}. \tag{4.8}$$

where $(\theta^{lab})_{\max}$ is the maximum decay angle observed in the lab. In the equation above, the only variable is the momentum of the decaying meson. It is easy to see that for a given momentum of the decaying meson, for π-decays the maximum kink angle is much smaller than for K-decays due to the small mass difference between the π and the muon. Hence, we can use the kink angle as additional selection parameter to distinguish between K- and π-decays. In Fig. 4.5 we show the maximum kink angle distributions for K- and π-decays as a function of the momentum of the decaying meson.

We have seen that both the kink angle and the momentum difference are random variables and their distributions depend on the parent mass, on the daughter mass and on the momentum of the parent. We envisage thus two types of situations for which the kink finder algorithm has to provide adequate strategies. One such type is the case of what we call large kink angle decays where the track segments in front of and behind the decay are reconstructed by the tracking algorithm as two distinctive tracks. The other type of situation occurs when the charged decay product is emitted at small

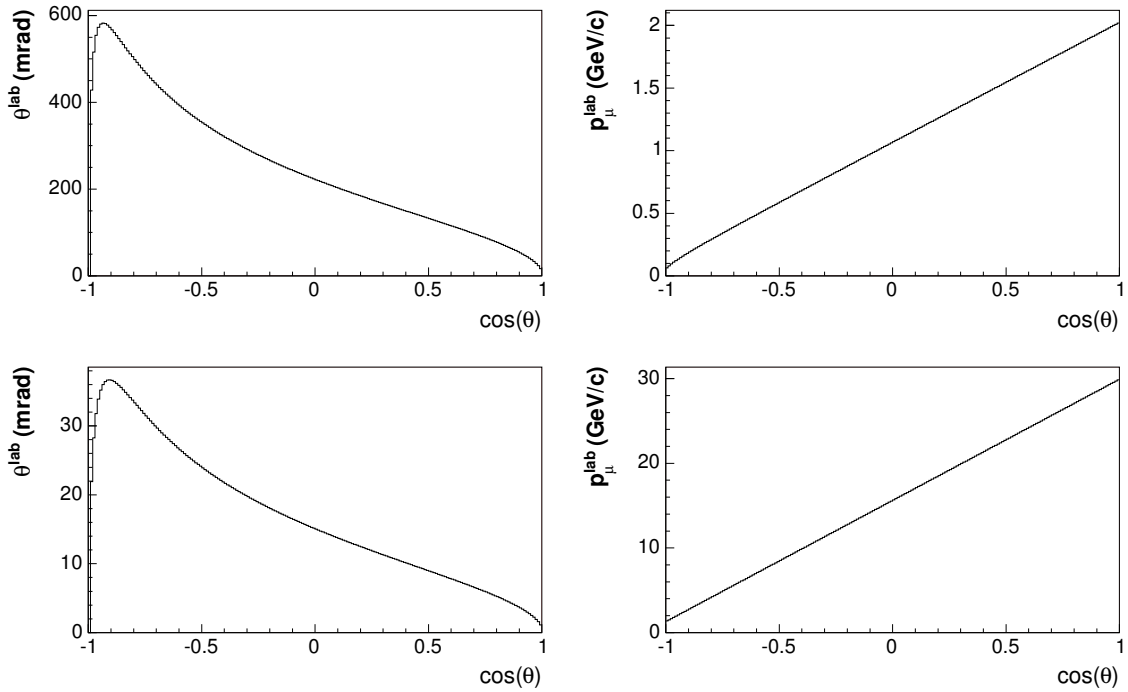

Figure 4.4: Distribution of the kink angle and the momentum of the muon as a function of the $cos\theta$ for the decay $K \rightarrow \mu\nu$. Top panel: $P = 2$ GeV/c; bottom panel: $P = 30$ GeV/c.

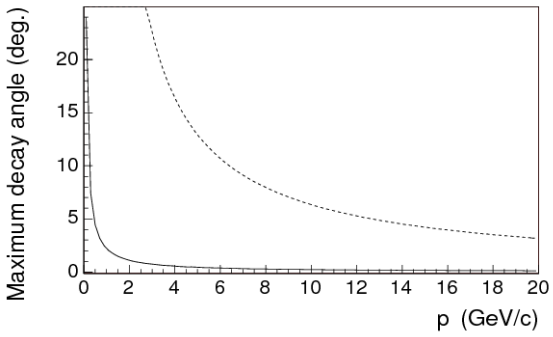

Figure 4.5: Distribution of the maximum decay angle as a function of the transverse momentum of the decaying meson. The dashed upper curve: K, the solid curve: π.

angle and its track and the track of the decaying particle are misinterpreted by the track search as a single track. If the track is regarded as a discrete dynamic system such a small angle kink is nothing else but a sudden change of the state vector, a change both in direction and in momentum (or curvature). The strategy here is to use

the wealth of by-product information of the Kalman filter to obtain trial breakpoint fits at every hit away from the ends of the track, which we then use to search for and characterize track breakpoints defined as locations where one or more of the track parameters are discontinuous. Clearly, when both the kink angle and the momentum difference are close to zero the chances of detecting the decay are rather small.

Given that both π- and K-mesons have a large $c\tau$, 780.4 cm and 371.3 cm respectively, and momentum in the central region of ALICE in a range from few MeV/c to few tens of GeV/c, we concentrate our search for kinks inside the volume of the TPC. Alternatively, we could aim to extend the search in the regions above and below TPC. However, in the region outside above TPC we cannot seed and/or determine sufficiently well the momentum of the charged decay product in the TRD. As a result, kinks cannot be recognized unambiguously and we would have to rely mostly on the breakpoint analysis. In the volume outside below the TPC most of decays come from low-momentum particles; due to their broad kink angle distribution, a search in the volume outside below the TPC would require seeding for the decaying particles in the ITS detector as well. Considering the penalties involved by an extension of the search region outside the TPC versus the overall gain in the high density environment, we decided to limit our search for kinks to the TPC volume.

Evidently, the performance of the kink finder will be improved by including the information from the other two tracking detectors in the central barrel, ITS and TRD. In order to include new information and minimize the track parameters errors, the tracking for the mother and daughter particles is an iterative process and consists of forward track propagation TPC-ITS towards the primary vertex, followed by back propagation ITS-TPC- TRD, and refit inward TRD-TPC-ITS.

4.1.2 The kink finding algorithm

As previously mentioned, the kink finding algorithm proceeds in two main steps. First, it reconstructs the large kink angle decays, then it searches for breakpoints in high-p_T track candidates to resolve the small kink angle decays. Each of these steps is split further and the selective requirements are gradually refined in order to speed up the algorithm without losing in performance.

The kink finding algorithm (large decay angles). Large decay angle kinks are reconstructed by associating pairs of tracks that intersect (within some tolerance) in space and have the same charge. The tracks that cross the entire TPC volume are rejected. Each of the tracks left is paired with all the other tracks passing a set of selection criteria: the tracks should not pass far from each other (i.e. should pass through the same or one of the neighbouring sectors and closer than 60 cm in the z-projection), should have the same charge and the summed number of clusters associated to the two tracks should be within certain boundaries.

For each track pair we find the distance of closest approach (DCA) in the bending plane (or the intersection points) and, if it does not happen inside a specified fiducial

region in R, such a pair is rejected (see Fig. 4.6) for the possible configuration). The fiducial volume at this step may exceed the TPC coverage. Then one calculates analytically in linear approximation the distance in space between the tracks at the position of the DCA found in the previous step, and imposes stronger constraints on the fiducial region and the newly calculated value of the DCA. Next, the decay vertex is reconstructed by a numerical minimization of the distance in space between the two helices representing the tracks. The algorithm allows minimizing a "normalized DCA" which takes into account the possible difference in the precision of the track position reconstruction in the transverse plane and along the beam direction. This increases a bit the precision of the reconstructed position of the decay vertex. The position of the decay vertex is supposed to be on the line corresponding to the DCA, and its optimum is given by the weighted mean of tracks positions, i.e. the distance between each of the two tracks and the decay vertex is proportional to the norm of the covariance matrix of the track parameters.

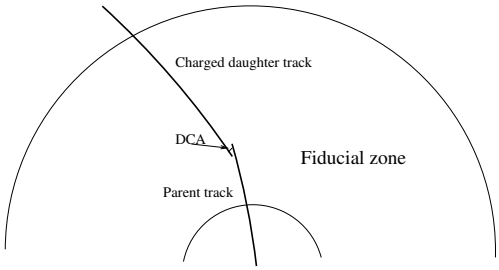

Figure 4.6: Geometrical selections in the $r\varphi$ projection used for the kink reconstruction.

Only pairs having the reconstructed kink position within the final fiducial volume are kept. This fiducial volume is limited by the track precision, which in TPC is mainly defined by the length of the track, and the tracking efficiency. The inner boundary of the fiducial zone is further limited by an increased (with respect to the outer pad rows) occupancy. One can see from the Fig. 4.7 that the fiducial area can hardly be extended outside the $R = 120 - 220$ cm range.

In order to further decrease the number of wrong track pairs, the track cluster densities, before and after the DCA position, are calculated for each track in the pair and a set of cuts on these track cluster densities is applied. Further, we compare the cluster densities before the DCA position for the two tracks in order to associate the correct track to the decaying particle and apply an upper limit cut on the curvature for the decaying particle.

Finally, for all the selected kink candidates, we refit the tracks towards the decay vertex, and additional rejection of improbable configurations is achieved by applying a cut on the decay angle. If a track can potentially belong to several kink candidates, only the best combination (the longest tracks, the highest cluster density, the smallest DCA) is kept.

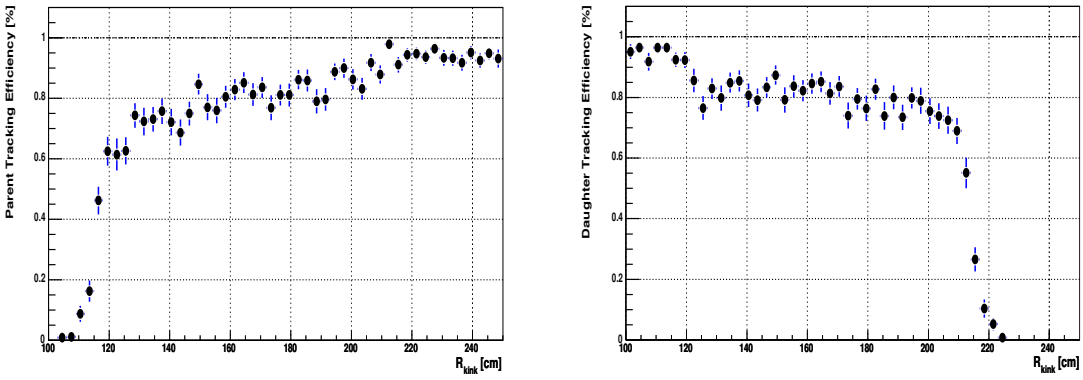

Figure 4.7: Left: Tracking efficiency for parent tracks as function of the radius of the decay vertex. Right: tracking efficiency for charged daughters as a function of the radius of the decay vertex.

The kink finding algorithm (small decay angles). The second part of the kink-finding algorithm starts with the selection of track candidates for breakpoint analysis. Low-momentum tracks ($p_T < 1.4$ GeV/c), tracks that are associated to any of the kink candidates found previously, tracks that share at least half of their associated clusters with tracks that belong to a kink candidate, and tracks which have less than a certain number (80) of associated clusters are rejected. For each of the track candidates we obtain at every hit on the track away from the ends (about 20 pad rows) three fits for the track parameters at that hit: a fit to the part of the track upstream, a fit to the part of the track downstream, and a fit to the whole track. Instead of using the classical test- statistics based on the χ^2 of the mismatch of all the forward-backward parameters at each hit (see [228, 224, 244]), we explicitly search for a change in direction.

Thus we use the upstream and the downstream parts of the track to define a kink for which we require that its decay vertex is inside the fiducial volume. We define the track breakpoint at the location of the kink for which we register the biggest change in track direction. Once the kink is thus defined, it will be stored if our selection criteria are met. These selection criteria require that the number of clusters associated to the two track segments is higher than certain values (at least 30 clusters for mother and at least 20 clusters for daughter), the decay vertex position is inside the fiducial volume and the DCA between the tracks is less than 0.5 cm, and that the p_T of the mother is not below 1.4 GeV/c.

4.2 Reconstruction cuts

The final set of cuts, aimed to reduce the number of found kinks that do not come from real decay, involve parameters that are well defined only after the last tracking pass including the information from the other tracking detectors is performed and the kink parameters are updated accordingly. They include the decay angle and its associated reconstruction error, the DCA, and the transverse momentum of the charged daughter calculated in the rest system of the decaying particle. It is noteworthy that the cuts have been optimized to minimize the level of background contamination while preserving the signal.

Figure 4.8 shows the various background sources and the q_T distribution of the reconstructed kinks in central Pb–Pb ($b < 3$ fm)[3] collisions at $\sqrt{s} = 5.5$ TeV with $\mathrm{d}N_{\mathrm{ch}}/\mathrm{d}\eta = 6000$. The empty area under the solid line represents the reconstructed kaons. The fake kinks produced by accidental track crossings and track splitting are marked by the hashed area and the pion decays by the grey filled area. Secondary kaons produced in hadronic interactions are in negligible number and therefore not visible in the figure. It is easy to see that the pion decays and the bulk of low-momentum accidental crossings between unrelated tracks will be rejected by cutting on the transverse charged daughter momentum calculated in rest system of the decaying meson, q_T (see the right panel of Fig. 4.3 for the distributions of charged daughters for different kaon decay channels and the q_T limit for pion decays).

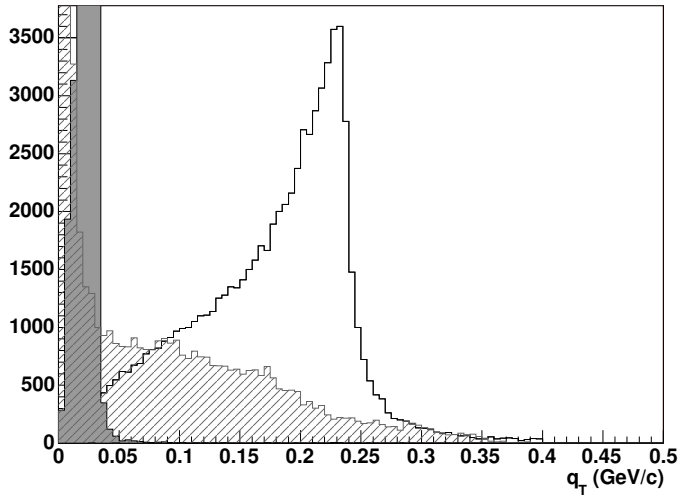

Figure 4.8: Left: q_T-distribution of the reconstructed kinks. The area under the solid line represents the signal, the hashed area the background due to random association of tracks and the grey filled area reconstructed pions.

[3] b denotes the impact parameter of the collision.

To improve further the signal-to-background ratio, one has to check for unrejected accidental crossings. We thus introduce a p_T- and event-multiplicity-dependent cut on the decay angle by requiring that the kink angle is not smaller than a certain critical angle parametrised in terms of decay angle reconstruction error. Also we require that tracks associated to the decaying particle pass through the ITS and survive the back-propagation to the TPC, both parent and daughter tracks are in the TPC acceptance and do not curl back inside the TPC, the impact parameter of the parent track is smaller than some value, and that the distance between the last hit of the parent and the kink vertex position does not exceed a given limit.

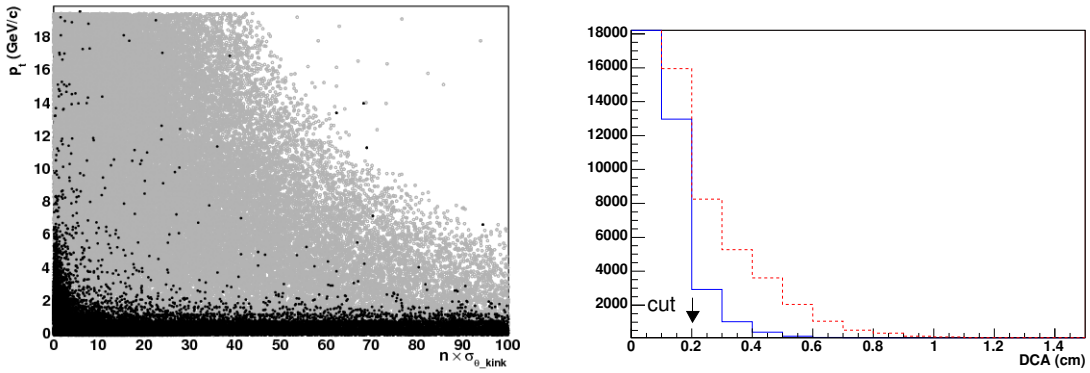

Figure 4.9: Left: Distribution of the decay angle parametrised in terms of its reconstruction error as a function of the transverse momentum of the parent track. The grey filled area represents the signal, the black dots show the background. Right: DCA distribution of the tracks associated to a kink topology. The solid line represents the DCA distribution for the signal, the dashed line shows the distribution for the background.

The left panel of Figure 4.9 shows the distribution of the decay angle quantified in terms of the reconstruction error $\sigma_{\theta_{\text{kink}}}$ as a function of the p_T of the decaying meson. The signal is marked by grey circles. The right panel of 4.9 illustrates the DCA distributions for the reconstructed signal (solid line) and for the fake kinks (dashed line).

The distribution of the impact parameter of the parent track (d_{parent}) is shown in the left panel of Fig. 4.10. Obviously, the parent track should point back to the event vertex.

Since kaons have a p_T threshold to pass through the ITS material and TPC cannot track well below 100 MeV/c, see Fig. 3.5, lower limit cuts on the p_T of the parent track and on the charged daughter momentum help to reject more background. The right panel of Fig. 4.10 shows the charged daughter momentum distribution for the signal (the empty area under the solid line) and background (filled area). The peak close to zero is mainly due to combinatorial background involving a spiraling electron

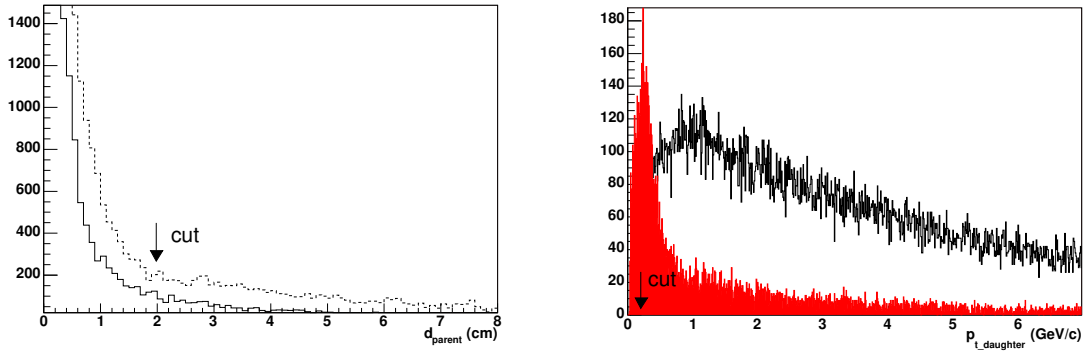

Figure 4.10: Left: The impact parameter distribution of the tracks associated to the decaying meson. The solid line represents the signal, the dashed line represents the background . Right: Momentum distribution of tracks associated to the charged daughter. The empty area under the solid line represents the signal, the dark filled area represents the background.

or close-by muons mostly decay products of pions created by inelastic interactions.

The main selection parameters and their cut values are listed in Table 4.1.

Table 4.1: Kink selection parameters and cut values.

Selection parameter	Cut value
fiducial region (R)	$120 < R < 220$ cm
q_T	> 50 MeV
distance of closest approach (DCA)	< 2 mm
decay angle	$> 3\sigma_{\theta_{\text{kink}}}$
θ_{Parent}	TPC polar angle acceptance
	$45° < \theta < 135°$
d_{parent}	< 2 cm
d_{daughter}	> 2 cm
p_{daughter}	> 100 MeV$/c$
$p_{T_{\text{parent}}}$	> 300 MeV$/c$

Chapter 5

Results

As discussed in Chapter 4, the final objective for kink reconstruction is to identify on a track-by-track basis statistically significant numbers of charged kaons over a wide momentum range. The limit is generally imposed either by the available statistics or by the quality of the reconstruction, particularly the momentum resolution. We recall that at high momenta the momentum resolution is determined by the detector's spatial precision, and this contribution increases proportionally to the particle momentum (see Eq. (3.5) in Chapter 3)[1]. Therefore, we have organized this chapter as follows. First, we define the criteria used to asses the quality of the kink reconstruction, describe the strategy adopted to simulate realistic background conditions and present the performance of the reconstruction. Then we evaluate the expected yields and background contamination in pp and Pb–Pb collisions at LHC and conclude on the momentum range over which significant statistics of kaons identified using the decay topology will be available the first year of data taking at the LHC.

5.1 Kink reconstruction performance

5.1.1 Estimation of the reconstruction quality

The quality of the reconstruction can be characterized by its precision, efficiency and probability to obtain a fake decay vertex. Precision is naturally defined as the width of the distribution of the differences between a true (simulated) parameter, such as momentum, decay angle or vertex position, and the reconstructed one. Efficiency of the kink finding and the probability to obtain a fake decay vertex is defined as:

$$\epsilon_{\text{good}} = \frac{number\ of\ \text{“}good\text{”}\ found}{number\ of\ \text{“}good\text{”}\ generated}$$

$$\epsilon_{\text{fake}} = \frac{number\ of\ \text{“}fake\text{”}\ found}{number\ of\ \text{“}good\text{”}\ generated}$$

[1] Momentum resolution depends on the magnetic field B, the track length l, and measurement error σ as $\Delta p/p \propto (p\sigma)/(B \cdot l^2)$.

In the above definitions, a 'good' ('findable') generated decay vertex fulfils the following conditions:

- it is inside the fiducial volume;
- it is inside the TPC acceptance range $45° < \theta < 135°$;
- it comes from a $K^{\pm} \rightarrow \mu^{\pm}\nu$ decay;
- the decay happens in the forward direction;

A 'good' found vertex must be

- inside the fiducial volume;
- coming from a real $K^{\pm} \rightarrow \mu^{\pm}\nu$ decay.

Finally, a found decay vertex is 'fake' if it does not come from a real decay.

The acceptance of the reconstruction chain is defined as following:

$$A = \frac{number\ of\ \text{“}good\text{”}\ generated}{total\ number\ of\ generated\ in\ 45° < \theta < 135°}$$

These estimates should be obtained using realistic background conditions and global production rates for the particles. The adopted simulation strategy is described in the next section. The results are presented in Sections 5.1.3 and 5.2

5.1.2 Signal and background simulations

The predicted kaon yields at the LHC and the acceptance of the reconstruction chain in the momentum range above a few GeV/c, see Figs. 5.6 and 5.7 respectively, have shown that the estimation of the background conditions, the efficiencies and the expected yields for reconstructed kaon decays would require the generation of a huge amount of events to get results with a reasonable statistics and consequently, significant computing resources. Hence, we performed this study making use of the event mixing technique, where pure signal events are embedded into background events at the level of summable digits[2] (for details, see chapter 4 of [53]). This choice is based on the assumption that the quality of the reconstruction and implicitly the background conditions depend crucially on the particle density and that the combinatorial background given by pairs of uncorrelated tracks dominates over other background sources. The mixing is done at the level of summable digits in order to incorporate the interference due to the detector response between the tracks.

We generated some number N of signal events consisting of 500 kaons (50% K^+ and 50% K^-) in the TPC acceptance range in intervals of 0.5 GeV/c covering a

[2]The 'summable digits' represent the signal produced by the detector in a format that corresponds to the raw data before digitisation and threshold subtraction.

wide range in transverse momentum, with p_T-momentum following the m_{t}-scaling (see Appendix A.1 for definition) and pseudo-rapidity distributions fixed by HIJING model parametrisations (for details, see [245] and Section 4.2 of [53]). The kaons were transported by GEANT through the detector set-up and forced to decay in the TPC fiducial volume ($120 < R < 220$ cm) to the $\mathrm{K} \rightarrow \mu\nu$ decay channel. This was done to increase further the statistics of findable generated signals. Apart from these pure signal events we also generated M HIJING [216, 217] background events (for the main settings of the generator, see Appendix A.2). Next, using the 'microscopic' (i.e. very detailed) simulators for the TPC and the other two tracking detectors, ITS and TRD, the detector response up to the zero suppression level is simulated independently for the pure signal and the HIJING background events. Then, the event mixing is carried out in turn for combinations of one of the N signal events (500 kaons) with one of the M HIJING background events the result being $N \times M$ signal enriched events. Finally, the full reconstruction chain was performed for each of these signal enriched events and estimations of the reconstruction efficiencies and precision, and of the background which might be expected, were obtained for different charged particles densities with different tracking detectors configurations: TPC stand-alone, ITS+TPC, and ITS+TPC+TRD.

Since the $\pi \rightarrow \mu\nu$ decay ($c\tau$ of 780.4 cm and branching ratio 99.98%) is the main competing source of kinks and the estimation of pion contamination with reasonable confidence would similarly require a big number of events especially in the hard p_T region, we have adopted the following strategy. We have fully simulated in the central barrel, samples of 3000 kaons and pions respectively, with p_T generated in intervals of 0.5 GeV/c spanning the $0.1 - 10$ GeV/c range (practically, we do not reconstruct pions with p_T above 10 GeV/c). The momentum and pseudo-rapidity distributions were fixed by HIJING model parametrisations and both pions and kaons were forced to decay uniformly in the TPC fiducial volume to the $\mu\nu$ channel. This was done in order to achieve, both for kaons and pions, a uniform population of decays in the fiducial volume of the TPC. Then we build the distribution of the K/π ratio as a function of p_T and decay radius, which later will be used to perform a normalization which takes into account the difference in the expected yields for kaons and pions, their different lifetimes and the exponential lifetime distribution for the decaying particle, and the difference in their branching ratios for the $\mu\nu$ decay channel. After performing the selection cuts the pion contamination found was below 2%.

5.1.3 Resolution of reconstructed parameters and reconstruction efficiency

We now turn to the performance of the kink reconstruction algorithm, i.e. we address the questions of kink finding efficiency, of decay vertex position, kink angle, q_T, and kaon's momentum resolutions, the question of how the efficiency of the kink finder depends on the momentum of the kaon, on the decay radius, and on the kink angle, and finally the question of pion contamination and background levels.

The kink reconstruction precision and efficiency using the TPC stand-alone for particle densities corresponding to pp and central Pb–Pb ($b < 3$ fm) collisions, i.e. the low and upper limit for the foreseeable particle densities corresponding to the running scenarios in ALICE, are summarized in Table 5.1. The results were obtained for the fiducial zone $120 < R < 220$ cm. The amplitude of the magnetic field was set to 0.5 T.

Table 5.1: Averaged over the interval $0< p_T <7$ GeV/c: The kink radial position resolution (σ_R), position resolution along the z-axis (σ_Z), kink angle resolution ($\sigma_{\theta_{\rm kink}}$), q_T resolution ($\sigma_{q_{\rm T}}$), momentum resolution of the decaying particle (σ_p), kink-reconstruction efficiency, pion contamination ($\epsilon_{\rm good}$ and $\epsilon_{\rm fake}$), and the acceptance (A) obtained using the TPC stand-alone.

	σ_R (mm)	σ_Z (mm)	$\sigma_{\theta_{\rm kink}}$ (mrad)	$\sigma_{q_{\rm T}}$ (MeV/c)	σ_p (GeV/c)	$\epsilon_{\rm good}$ (%)	$\epsilon_{\rm fake}$ (%)	A (%)
pp	3.9	1.4	1.8	8.5	2.4	72.5	0	2.4
Pb–Pb	7.1	2.8	3.3	16	4.9	47	1.9	2.4

It can be seen that efficiency and resolutions deteriorate when the track density increases. This is mainly due to the cluster overlaps which are more probable for higher particle multiplicities.

The values in Tab. 5.1 depend on the momentum of the decaying meson. This dependence is illustrated in Fig. 5.1. The curves marked by empty circles correspond to the pp low multiplicity. The full circles mark the values obtained for high particle densities expected in central Pb–Pb collisions.

Figure 5.1 (c) shows that almost over the whole p_T range the position resolution of the decay vertex is below the 1 cm limit (which is roughly the size of a TPC pads), i.e. overall, the kinks are found in the correct position. At high p_T the maximum decay angle becomes smaller and consequently, the probability to pick up clusters from the pair track increases thus leading to a decrease in parameters resolutions. The resolution of the charged daughter transverse momentum in the rest system of the decay, see q_T in Figure 5.1 (b), worsens with the increase of the p_T of the decaying particle mainly due to the decrease in resolution of the momentum of the charged daughter. The momentum resolution for the decaying particle, see Figure 5.1 (a) deteriorates far more rapidly for high particle multiplicities as it was expected. This is largely due to the cluster overlaps and a higher probability to pick up an outlier that we cannot remove later. By limiting the fiducial volume (e.g., $160 < R < 220$ cm) we can improve the momentum resolution, see Fig. 5.2. However, by doing so the overall acceptance drops by about 40%.

The slight worsening of the kink angle resolution at low-p_T see Fig. 5.1 (d), reflects the trend in the overall tracks angular resolution as shown in Fig. 3.9 in Section 3.5. We recall that the tracks angular resolution is defined by the multiple scattering on

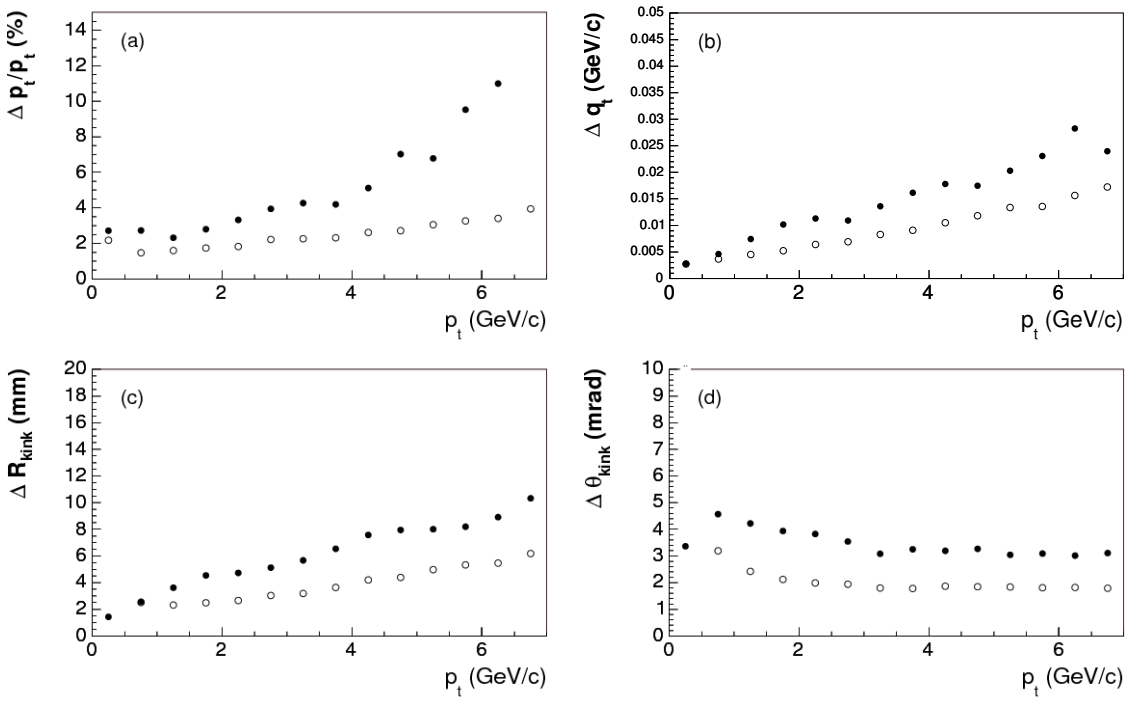

Figure 5.1: Resolutions of different kink parameters reconstructed with the TPC stand-alone as a function of the momentum: (a) momentum resolution of the decaying particle; (b) momentum resolution of the charged daughter in the rest system of the decay; (c) kink radial position resolution; (d) kink angle resolution. Full circles: central Pb–Pb collisions ($\mathrm{d}N_{\mathrm{ch}}/\mathrm{d}\eta = 6000$). Empty circles: pp collisions.

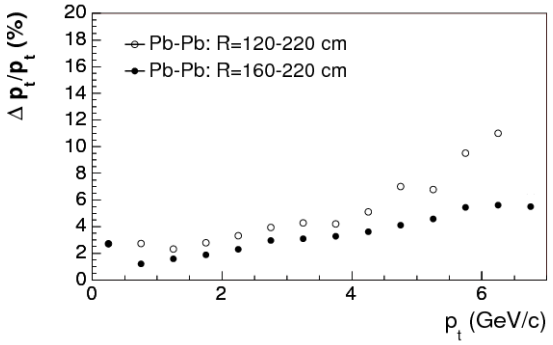

Figure 5.2: Transverse momentum resolution of reconstructed K with TPC stand-alone for different fiducial zones for central Pb–Pb collisions ($\mathrm{d}N_{\mathrm{ch}}/\mathrm{d}\eta = 6000$) . Full circles: $120 < R < 220$ cm. Empty circles: $160 < R < 220$ cm.

the material between the last space point assigned to a track and the primary vertex.

Evidently, the addition of the ITS and TRD significantly reduces the uncertainties of the kink parameters. This is due to the fact that both mother and daughter tracks are in this case reconstructed over a large length and so with a better precision. The results are shown in Table 5.2 and Fig. 5.3. The numbers shown in parentheses in Table 5.2 correspond to values averaged over the same p_T interval as the values shown in Table 5.1.

Table 5.2: Averaged over the interval $0< p_T <20$ GeV/c ($0< p_T <7$ GeV/c, in parentheses): The kink radial position resolution (σ_R), position resolution along the z-axis (σ_Z), kink angle resolution ($\sigma_{\theta_{\rm kink}}$), $q_{\rm T}$ resolution ($\sigma_{q_{\rm T}}$), momentum resolution of the decaying particle (σ_p), kink reconstruction efficiency, pion contamination ($\epsilon_{\rm good}$ and $\epsilon_{\rm fake}$), and the acceptance (A) obtained using the ITS, TPC and TRD combined together.

	σ_R (mm)	σ_Z (mm)	$\sigma_{\theta_{\rm kink}}$ (mrad)	$\sigma_{q_{\rm T}}$ (MeV/c)	σ_p (GeV/c)	$\epsilon_{\rm good}$ (%)	$\epsilon_{\rm fake}$ (%)	A (%)
pp	6.4 (2.9)	2.4 (1.0)	0.95 (1.2)	6.4 (4.4)	2.5 (1.9)	77.5 (77.5)	0 0	1.5
Pb–Pb	9.8 (4.8)	3.9 (1.8)	1.6 (1.8)	11.5 (7.)	2.9 (2.2)	48.8 (52.8)	2.1 (2.8)	1.5

One can see that including the TRD the q_T resolution improves by about a factor of 2. Similarly, for particle densities expected in central Pb–Pb collisions, the momentum resolution of the decaying kaon is improved almost by a factor 2 if we add the ITS into the reconstruction. We found that in a very high track-density environment, the momentum range over which we can use kink reconstruction to identify kaons with momentum resolution better than 10% extends well above 20 GeV/c compared to about 6 GeV/c, respectively 12 GeV/c if we restrict the fiducial zone to $160 < R < 220$ cm, when only the TPC information is used. Likewise, in a low-multiplicity environment, we can extend this momentum range from about 15 GeV/c, respectively 20 GeV/c when $160 < R < 220$ cm, to p_T above 20 GeV/c by using the combined tracking information. The kink reconstruction efficiency increases only slightly, about 4%.

For convenience, the p_T -dependence of the kink finding efficiency for combined tracking will be presented in Section 5.2.3. Here, we only discuss the overall intrinsic efficiency of the kink finder for the TPC stand-alone and show the dependence on the position of the decay (left panel of Fig. 5.4), and on the kink angle (right panel of Fig. 5.4) for low-multiplicity environment. The dependence on the position of the decay is rather weak as expected; a slight loss in efficiency, however, can be observed towards both ends of the detector. As function of the kink angle, the efficiency rises steeply from zero and attains the maximum at a value of about 20 mrad.

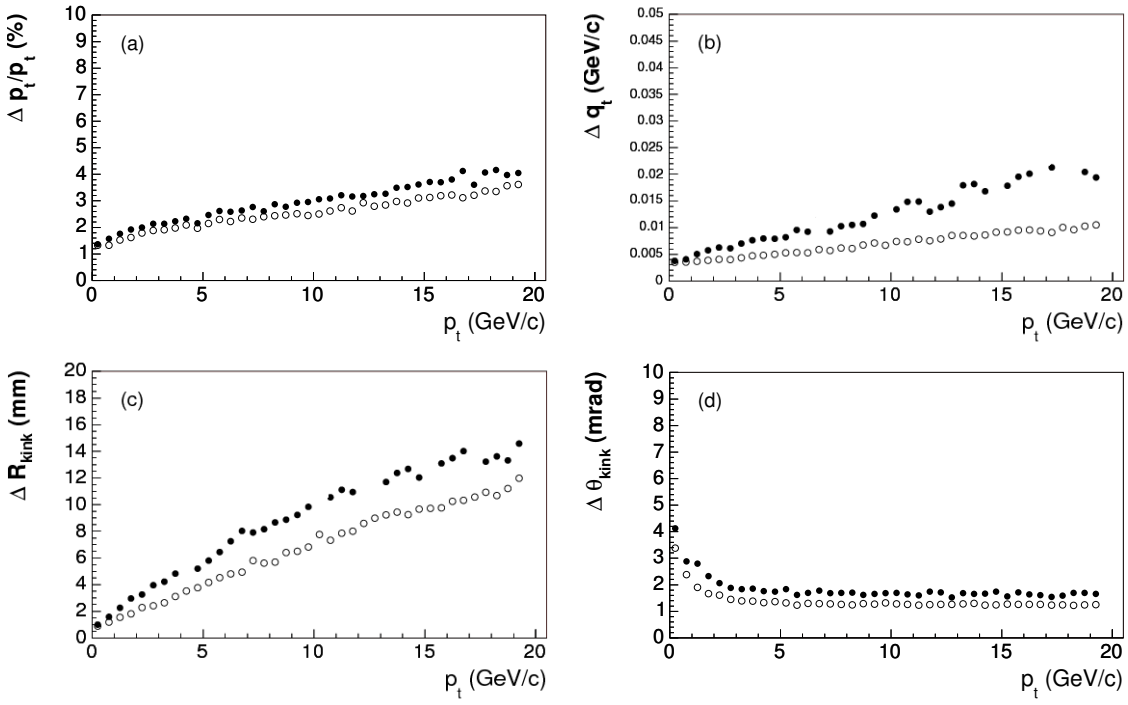

Figure 5.3: Resolutions of different kink parameters reconstructed with the ITS, TPC and TRD combined together: (a) momentum resolution of the decaying particle; (b) momentum resolution of the charged daughter in the rest system of the decay; (c) kink radial position resolution; (d) kink angle resolution. Full circles: central Pb–Pb collisions ($\mathrm{d}N_{\mathrm{ch}}/\mathrm{d}\eta = 6000$). Empty circles: pp collisions.

As a kink can be reconstructed only if its two track segments are found by the tracking, the maximum kink finding efficiency we may hope to get is given by the combined tracking efficiencies for the secondary track and the primary track in the pair. The probability to track both tracks of the pair is shown in Fig. 5.5 (left) as a function of p_T of the decaying kaon. The right panel of Fig. 5.5 shows the intrinsic efficiency for the kink reconstruction algorithm. The latter is obtained by dividing the kink reconstruction efficiency to the efficiency to track both tracks of the pair. From Fig. 5.5 one can see that for low particle densities the intrinsic efficiency of the kink reconstruction method is around 98%. This value is a bit lower, about 90%, for very high particle densities.

This is largely due to higher uncertainties of the track parameters of both track segments caused by cluster overlaps.

Summing up, using the kink finder with TPC alone the momentum range over which we can use the kink reconstruction to identify kaons is limited by the poor momentum resolution of the kaons, particularly in a high-multiplicity environment. However, by using the information from the other two tracking detectors, ITS and

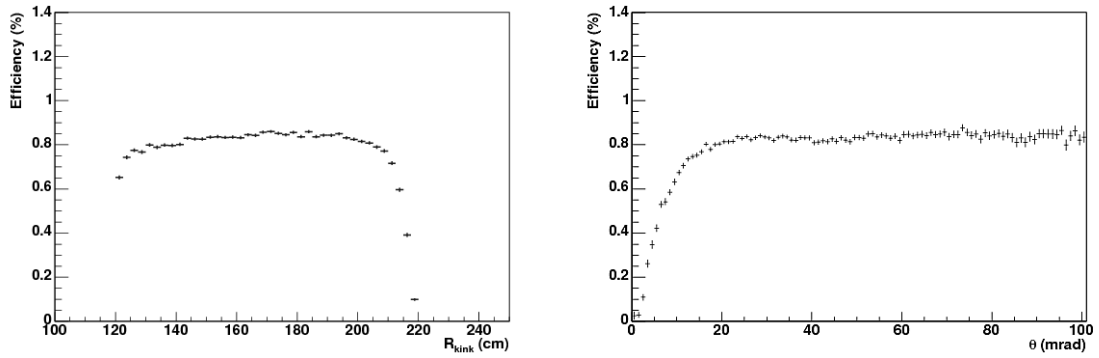

Figure 5.4: pp collisions: Left: Reconstruction efficiency for as a function of the decay vertex. Right: Reconstruction efficiency as a function of the decay angle.

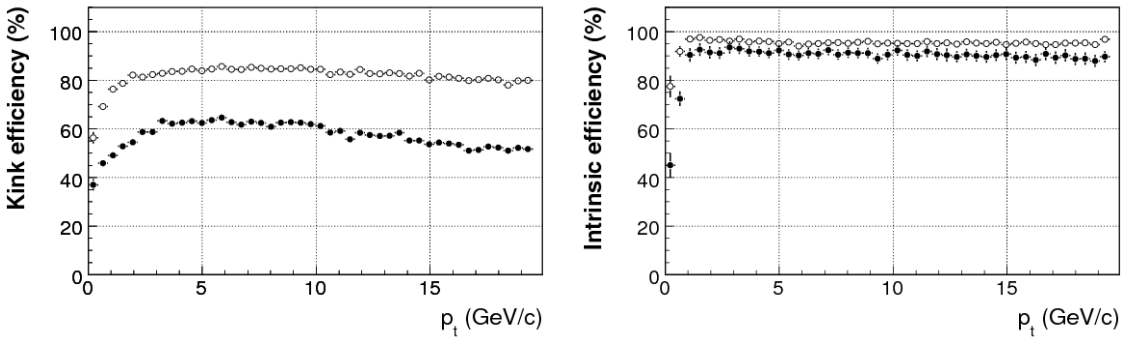

Figure 5.5: Left: Tracking efficiency for the pair of tracks associated to a 'good' generated kink in TPC stand-alone. Right: Intrinsic kink reconstruction efficiency in TPC stand-alone. Full circles: central Pb–Pb collisions ($\mathrm{d}N_{\mathrm{ch}}/\mathrm{d}\eta = 6000$). Empty circles: pp collisions.

TRD, the performance improves considerably due to the fact that the track parameters of both track segments are reconstructed with better precision. In this case, the p_T-range over which we can identify on a track-by-track basis statistically significant numbers of charged kaons is limited practically by the available statistics as we shall show in the next section.

5.2 Yields of reconstructed kaon decays at LHC

Having the estimates for the momentum resolution of the kaon as function of p_T we aim now to evaluate the expected yields and background contamination in pp and Pb–Pb collisions at LHC, and implicitly the range of the transverse momenta over

which significant statistics of kaons identified via their decay topology will be available after the first year of data taking at the LHC.

5.2.1 Estimation of the kaon yields

In order to evaluate the expected yields of kaons identified via their kink topology, we have to account for reconstruction (in)efficiency, detector acceptance for the reconstruction chain, hadronic interactions and particle misidentification. All these corrections not only depend on the transverse momentum, but also on rapidity, on the event multiplicity and track quality criteria. However, their functional dependence on p_T is the most important and we will obtain the inclusive spectrum of identified kaons via their kink topologies by convoluting the transverse momentum distribution predicted for kaon production at LHC, the acceptance profile and the reconstruction efficiency function. Thus, in each p_T bin, the expected yield is given by:

$$N_{\mathrm{K}}{}^{rec}(p_T) = N_{\mathrm{K}}{}^{prod}(p_T) \times ACC(p_T) \times EFF(p_T) \tag{5.1}$$

where $N_{\mathrm{K}}{}^{rec}$ is the number of reconstructed kaons in the p_T bin, $N_{\mathrm{K}}{}^{prod}$ is the number of kaons produced, ACC is the acceptance of the reconstruction chain and EFF is the reconstruction efficiency.

5.2.2 Kaon production at LHC and acceptance

PYTHIA [220, 221, 222] version 6.214 with CTEQ5L as parton distribution functions and multiple interactions switched on, was used to generate 2.5×10^6 minimum-bias pp events at $\sqrt{s} = 14$ TeV (see Appendix A.2 for the main settings used for PYTHIA). The p_T distribution of kaons emerging from collisions as generated with PYTHIA in this configuration was extrapolated to one year of LHC pp data taking (10^9 pp events). An overall event trigger efficiency of about 82% (see Section 3.15.2 of [53]) was taken into account and a pseudo-rapidity η cut, $|\eta| < 0.9$, corresponding to the TPC geometrical acceptance was applied. The extrapolated distribution is shown in the left panel of Fig. 5.6. The right panel of Fig. 5.6 shows the p_T distribution of kaons produced in 10^7 central Pb–Pb collisions at LHC energy, generated using a HIJING parametrisation model (for details, see [245] and Section 4.2 of [53]). Here, we only point out that the η distribution was scaled to a charged particle multiplicity of $\mathrm{d}N_{\mathrm{ch}}/\mathrm{d}\eta = 6000$ (expected to correspond to most central collisions at LHC) in the pseudo-rapidity interval $|\eta| < 0.5$ and the kaon p_T-distribution was obtained from the pion distribution by m_{t}-scaling. For Pb–Pb collisions, the event trigger efficiency is close to 100% (see [53, 206]). A η cut, $|\eta| < 0.9$, corresponding to the TPC geometrical acceptance was applied as well.

The acceptance for the reconstruction chain, see Fig. 5.7, is a product of several factors: geometrical acceptance, decay probability, the effect due to the fiducial volume restriction and quality criteria of tracks. Hence, we calculate it in each p_T-bin as the fraction of initially generated kaons resulting in 'findable' generated kinks

(see Section 5.1.1 for definitions). In order to calculate the acceptance, we generated 3.5×10^6 single particle events (50% K^+, 50% K^-) with flat p_T and η distributions, and transported them through the ALICE set-up using the GEANT transport code incorporated in the AliRoot framework. Note that the predicted η dependence was already taken into account when we obtained the transverse momentum distributions shown in Fig. 5.6. We recall that kaons have a $c\tau$ of 371.3 cm and we concentrate on the search for kinks inside the volume of the TPC. To maximize the acceptance, the fiducial region is extended as much as the track precision and tracking efficiency allow it. Figure 4.7 of Chapter 4 shows that the fiducial area can hardly be extended outside the $R = 120 - 220$ cm range.

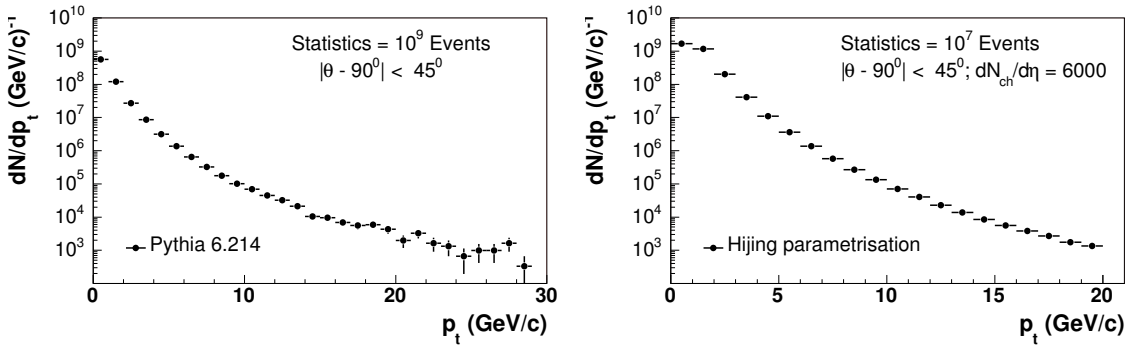

Figure 5.6: Left: PYTHIA 6.214 prediction for p_T distribution of charged kaons in 10^9 pp collisions at $\sqrt{s} = 14$TeV in the central barrel. An overall event trigger efficiency of about 82% was taken into account. Right: HIJING parametrisation prediction for 10^7 central Pb–Pb collisions with $\mathrm{d}N_{\mathrm{ch}}/\mathrm{d}\eta = 6000$ at $\sqrt{s} = 5.5$TeV.

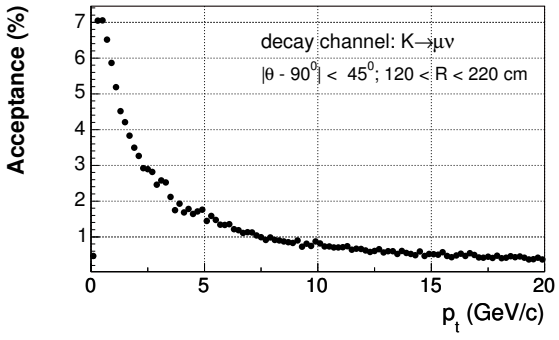

Figure 5.7: The p_T-dependence of the acceptance of the reconstruction chain for the $K \to \mu\nu$ decays.

5.2.3 Yields of reconstructed kaon decays, contamination and p_T range of identified kaon decays

In this section we will summarize the current results only for pp and central Pb–Pb ($b < 3$ fm) event multiplicities when we use full combined tracking information (ITS+TPC+TRD). Some 60 central Pb–Pb ($b < 3$ fm) background events at $\sqrt{s} = 5.5$ TeV generated using the HIJING 1.36 generator with jet quenching and nuclear shadowing switched on, and a total of about 250 enriched signal events with a charged particle density $\mathrm{d}N_{\mathrm{ch}}/\mathrm{d}\eta \approx 6200$ at mid-rapidity have been considered for this study. The magnetic field was set to 0.5 T.

The reconstruction efficiency was evaluated as the fraction of the findable generated kaon decays that can be associated to reconstructed kaon decays. The left and right panels of Fig. 5.8 show the results for pp and central Pb–Pb multiplicities respectively, as a function of p_T. Compared to pp, there is a significant drop in the reconstruction efficiency for central Pb–Pb events due to cluster overlaps, which lead to lower tracking efficiencies for the two track segments associated to a kink and higher uncertainties for the track parameters. At high p_T ($p_T > 10$ GeV/c) both efficiency functions decrease gradually with the increase of p_T. This behavior is consistent with a decrease in the decay angle (see Fig. 4.5) and consequently, with the fact that more kinks have decay angles which fall below the angular resolution of our detector. In addition, the parameters of small decay angle kinks are determined with less precision and fewer candidates meet our quality selection criteria. One of the cuts introduced to reduce the background level is a p_T -dependent selection on the decay angle. Here, we require that the kink angle is not smaller than a certain critical angle parametrised in terms of the decay angle reconstruction error. The main selection parameters and their cut values are listed in Tab. 4.1 of Chapter 4. We recall that the cuts have been optimized to minimize the level of background contamination while preserving the signal. The overall efficiencies for pp and central Pb–Pb events with a charged-particle density $\mathrm{d}N_{\mathrm{ch}}/\mathrm{d}\eta \approx 6000$ is about 77% and 49% respectively.

Considering the existing uncertainties in the prediction of the charged-particle density, we also calculated the efficiencies (not shown here) for central Pb–Pb events with different charged-particle densities. For $\mathrm{d}N_{\mathrm{ch}}/\mathrm{d}\eta = 4000$, the overall efficiency is about 55%, while for $\mathrm{d}N_{\mathrm{ch}}/\mathrm{d}\eta = 2000$ is around 68%. As expected, the background contamination in these cases is lower.

As already mentioned, the main source of contamination is background due to random association of tracks, mostly low-p_T tracks, and to a much lesser extent track splitting, pion decays, and decays of kaons coming from secondary interactions. The level of background contamination in central Pb–Pb events is shown as a function of p_T in Fig. 5.9. It is noteworthy that starting with $p_T > 2$ GeV/c the background level drops practically to zero. In pp events the overall background is negligible (well below the 1% level).

The yields of reconstructed kaon decays as a function of p_T are obtained by convoluting the distributions shown in Figs 5.6, 5.7 and 5.8, namely the predicted momen-

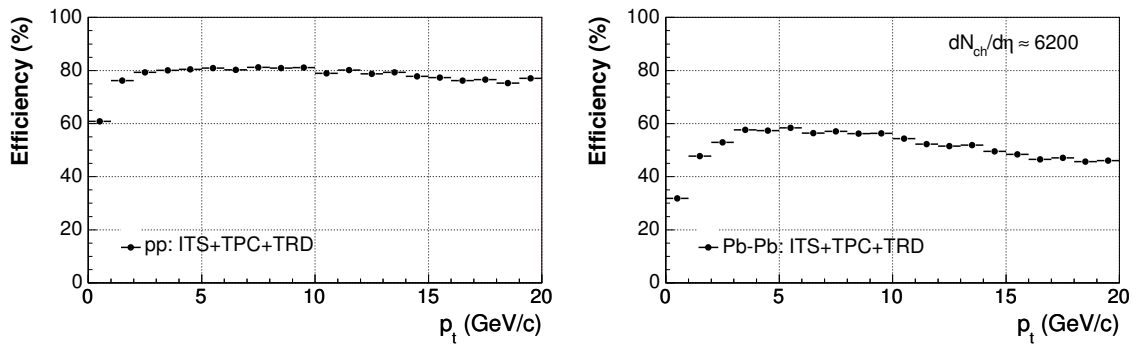

Figure 5.8: Left: Reconstruction efficiency as a function of p_T for pp multiplicities. Right: Reconstruction efficiency as a function of p_T for central Pb–Pb ($b < 3$ fm) with $\mathrm{d}N_{\mathrm{ch}}/\mathrm{d}\eta \approx 6200$.

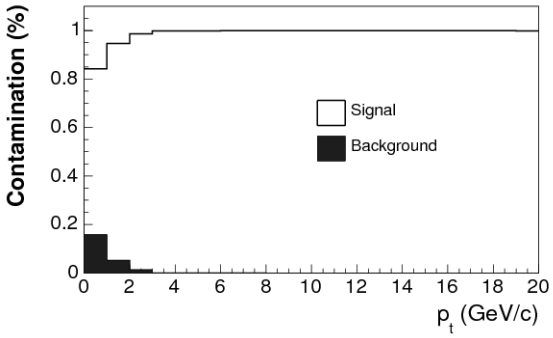

Figure 5.9: Background contamination (dark area) for central Pb–Pb ($b < 3$ fm) with $\mathrm{d}N_{\mathrm{ch}}/\mathrm{d}\eta \approx 6200$. The hashed area represents the reconstructed signal. Note that the reconstructed signal includes also kaons from the $\mathrm{K} \rightarrow \pi\pi^0$ decay channel.

tum distribution for kaons at LHC, the acceptance of the reconstruction chain and the efficiency. The yields are illustrated in Fig. 5.10.

Using the left panel of Fig. 5.10 we see that for a total sample of 10^9 pp events, usable statistics of kaons can be obtained up to $p_T = 17$ GeV/c. For 10^7 central Pb–Pb events with $\mathrm{d}N_{\mathrm{ch}}/\mathrm{d}\eta = 6000$, see right panel of Fig. 5.10, this range extends up to at least $p_T = 13$ GeV/c, far beyond the scope of soft physics. Note that the p_T-range over which we can identify kaons via their decay topology is limited by the available statistics, which can always be redressed by more beam time, and not by the momentum resolution (see Fig. 5.3).

The results depend strongly on factors which are poorly known, and it is possible that the shapes, notably the inverse slope parameter, T, of the real spectra will differ from the ones we used in this simulation. The fit value for the exponential distribution slope parameter we have used for kaons was found to be $T \approx 610$ MeV in the

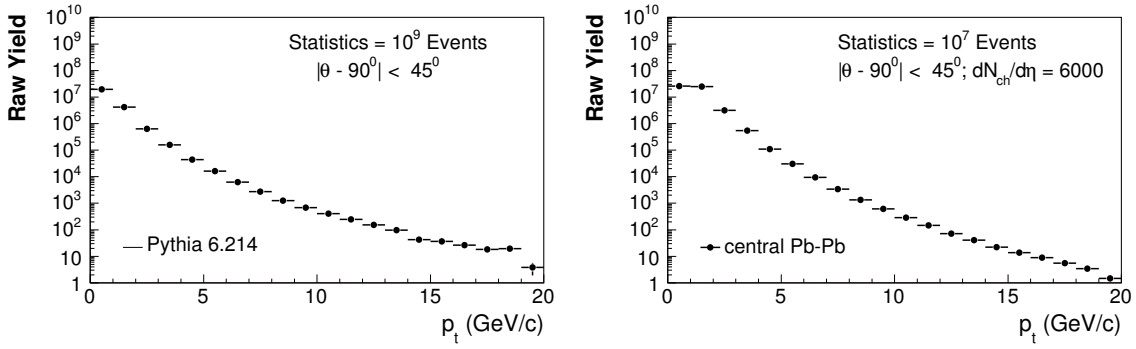

Figure 5.10: Left: Transverse momentum distribution of reconstructed K as expected for 10^9 pp events. Right: Transverse momentum distribution of reconstructed K as expected in 10^7 central Pb–Pb events.

intermediate-p_T region $1 \leq p_T \leq 5$ GeV/c integrated over the whole pseudo-rapidity range of $|\eta| < 8$.

It is noteworthy that statistically significant numbers of identified hyperons will also be available up to transverse momenta dominated by hard scattering of partons from the incoming nuclei (see Sections 6.2.3 and 6.2.4 of [186]).

Finally, we recall that in the transverse momentum range $0.1 \leq p_T \leq 3$ GeV/c, the kink reconstruction technique is complementary to the combined particle identification technique described in Section 5.4.6 of [186]. This allows us to perform systematic comparisons between the methods.

Chapter 6

Conclusions

In this work, we study the performance of the ALICE detector for kaon identification on a track-by-track basis using the decay topology.

In our approach, kinks (i.e. pion or kaon decays) are reconstructed inside the TPC in the fiducial region, $120 < R < 220$ cm, with a kink finding algorithm which associates pairs of track candidates that intersect in space, and searches for breakpoints in high-p_T tracks. The performance of the reconstruction algorithm depends mainly on the efficiency of the seeding and track finding algorithms, on the choice of configuration of tracking detectors, and on the track density.

Our analysis addresses different configurations of tracking detectors and both the low and the very high track density environment specific to pp and central Pb–Pb collisions, respectively. We found that using the kink finder with TPC stand-alone the momentum range over which we can use the kink reconstruction to identify kaons is limited by the momentum resolution of the kaons, particularly in a high-multiplicity environment. However, by including the information from the other two tracking detectors in the central part of the detector, the ITS and the TRD, momentum resolution improves considerably (better than 4% at $p_T = 20$ GeV/c), and the p_T-range over which we can identify on a track-by-track basis statistically significant numbers of charged kaons is limited practically only by the available statistics. We found that on average only about 2% of the kaons produced decay in the fiducial zone of the TPC. The kink reconstruction efficiency for charged kaons is about 78% for pp collisions and about 43% for central Pb–Pb collisions at $p_T \sim 20$ GeV/c. The level of background contamination in central Pb–Pb events is low; starting with $p_T > 2$ GeV/c it drops practically to zero. In pp events the overall background is negligible.

We found that statistically significant numbers of identified kaons will be available up to transverse momenta dominated by hard scattering of partons from the incoming nuclei (p_T up to 13 GeV/c in central Pb–Pb events). Owing to the access to a higher-p_T range than that available to the RHIC experiments and given that statistically significant numbers of identified hyperons will also be available up to transverse momenta dominated by hard scattering of partons from the incoming nuclei, we can conclude that we will be able to investigate more definitively the quark scaling be-

haviour expected from coalescence models and the effects of the traversed matter on hard probes, i.e., the origin of the observed meson-baryon differences in flow and yield in the intermediate-p_T region, and also the influence of parton-medium interactions on jet properties. On the same footing, the broad-p_T range (p_T up to 17 GeV/c) we found to be statistically accessible in pp collisions will allow us not only to provide references for the heavy-ion collision data but also to gain insight into possible deconfinement in pp collisions and poorly understood properties (e.g. the mean transfer momentum) via the measured strangeness content.

Appendix A

Appendix

A.1 Definitions

A.1.1 Elliptic flow

In non-zero impact parameter heavy ion collisions, the matter which overlaps has an asymmetry in density relative to the reaction plane. The initial overlap region has an almond shape (see Fig. A.1).

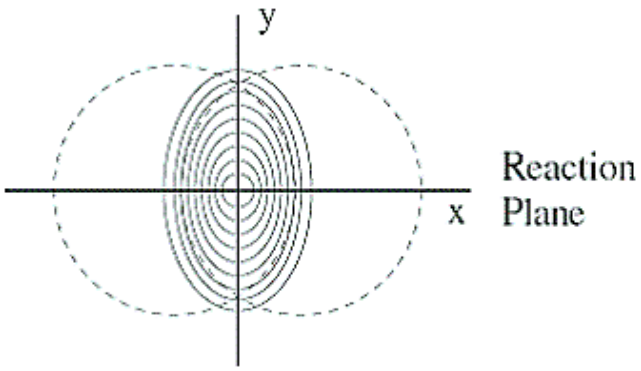

Figure A.1: Initial overlap in a non-central collision. The beam direction is perpendicular to the page.

If the produced matter thermalizes quickly, pressure builds up inside and the spatial deformation results in anisotropic pressure gradients that generate stronger collective flow in the shorter direction than in the longer one and the p_T distribution becomes anisotropic. This anisotropy in momentum will reduce the initial spatial

anisotropy as the source evolves with time. This phenomenon is called *elliptic flow* and is measured by the second coefficient v_2 of the Fourier expansion [246] of the p_T spectrum:

$$E\frac{d^3N}{d^3p} = \frac{1}{2\pi}\frac{d^2N}{p_T dp_T dy}(1 + \sum 2v_n \cos(n(\varphi - \Phi_r))), \tag{A.1}$$

where Φ_r is the reaction plane angle and φ the azimuthal angle of the particle.

A.1.2 m_t-scaling

Identified particles spectra have been succesfully described by a 'universal' parameterization of the form shown in equation

$$E\frac{d^3N}{d^3p} = A\frac{e^{-m_t/T}}{m_t^\lambda}, \tag{A.2}$$

where m_t is the transverse mass ($\sqrt{p_T^2 + m^2}$). This phenomenon is known as m_t-scaling and would seem to suggest that over a given range of m_t, spectra of particles with different masses would have similar slopes.

A.2 Settings for the event generators

A.2.1 PYTHIA parameters

In table A.2.1, we give the list of parameters, which we use for the creation of non-diffractive pp events with the PYTHIA event generator [220, 221, 222], version 6.214, which is packaged in AliRoot (classes AliPythia and AliGenPythia).

A.2.2 HIJING parameters

In table A.2.2, we give the list of parameters, which we use for the creation of Pb–Pb (background) events with the HIJING event generator [216, 217], version 1.36, which is packaged in AliRoot (classes AliGenHijing and THijing).

A.3 Mathematical formalism of the Kalman filter

The conditions for the applicability of the Kalman filter are as follows. A certain 'system' is determined at any time moment t_k by a state vector x_k. The state vector varies with time according to an evolution equation

$$x_k = f_k(x_{k-1}) + \epsilon_k.$$

It is supposed that f_k is a known determenistic function and ϵ_k is a random vector of intrinsic 'process noise' which has a zero mean value ($< \epsilon_k >= 0$) and a known

Description	Parameter	Value
Process types	MSEL	1
	MSUB(92)	1
	MSUB(93)	1
	MSUB(95)	1
	MSUB(95)	1
CTEQ5L parameterization	MSTP(51)	4046
Proton PDF	MSTP(52)	2
Switch on resonance decays	MSTP(41)	1
Switch on multiple interactions	MSTP(81)	1
	MSTP(82)	4
	PARP(82)	1.8 GeV
	PARP(83)	0.3
	PARP(84)	0.5
Initial/final state radiation on	MSTP(61)	1
	PARP(67)	1
Intrinsic k_t from Gaussian	MSTP(91)	1
	PARP(91)	1

Table A.1: PYTHIA parameter setting for the generation of non-diffractive pp collisions at $\sqrt{s}$=14 TeV. Remaining parameters are left to PYTHIA 6.214 default settings.

Description	Parameter	Value
Switch on jet quenching	IHPR2(4)	1
(hijing default)	IHPR2(50)	0
Initial/final state radiation on	IHPR2(2)	3
Switch off resonance decays	IHPR2(12)	1
Switch on shadowing	IHPR2(6)	1

Table A.2: HIJING parameter setting for the generation of Pb–Pb collisions at $\sqrt{s}$=5.5 TeV. Remaining parameters are left to HIJING 1.36 default settings.

covariance matrix ($cov\epsilon_k = Q_k$). Generally, only some function h_k of the state vector can be observed, and the result of the observation m_k is corrupted by a 'measurement noise' δ_k:

$$m_k = h_k(x_k) + \delta_k$$

The measurement noise is supposed to be unbiased ($< \delta_k >= 0$) and having a definite covariance matrix ($cov\delta_k = V_k$). In many cases, the measurement function h_k can be represented by a certain matrix H_k:

$$m_k = H_k x_k + \delta_k$$

If, at a certain time t_{k-1}, we are given some estimates of the state vector $\tilde{x}_{k-1}$ and of the its covariance matrix $\tilde{C}_{k-1} = cov(\tilde{x}_{k-1} - x_{k-1})$, we can extrapolate these estimates to the next time slot t_k by means of formulas (this is called 'prediction'):

$$\begin{aligned} \tilde{x}_k^{k-1} &= f_k(\tilde{x}_{k-1}) \\ \tilde{C}_k^{k-1} &= F_k \tilde{C}_{k-1} F_k^T + Q_k, \quad F_k = \frac{\partial f_k}{\partial x_{k-1}} \end{aligned} \tag{A.3}$$

The value of the predicted χ^2-increment can be also calculated:

$$(\chi^2)_k^{k-1} = (r_k^{k-1})^T (R_k^{k-1})^{-1} r_k^{k-1}, \quad r_k^{k-1} = m_k - H_k \tilde{x}_k^{k-1}, \quad R_k^{k-1} = V_k + H_k \tilde{C}_k^{k-1} H_k^T$$

The number of degrees of freedom is equal to the dimension of the vector m_k.

If at the moment t_k, together with the results of prediction, we have also the results of the state vector measurement, this additional information can be combined with the prediction results (this is called 'filtering'). As the result, the estimation of the state vector improves:

$$\tilde{x}_k = \tilde{x}_k^{k-1} + K_k(m_k - H_k \tilde{x}_k^{k-1}) \tag{A.4}$$

$$\tilde{C}_k = \tilde{C}_k^{k-1} - K_k H_k \tilde{C}_k^{k-1}, \tag{A.5}$$

where K_k is the Kalman gain matrix $K_k = \tilde{C}_k^{k-1} H_k^T (V_k + H_k \tilde{C}_k^{k-1} H_k^T)^{-1}$.

At last, the next formula gives us the value of filtered χ^2-increment:

$$\chi_k^2 = (r_k)^T (R_k)^{-1} r_k, \quad r_k = m_k - H_k \tilde{x}_k, \quad R_k = V_k - H_k \tilde{C}_k H_k^T$$

It can be shown that the predicted χ^2 value is equal to the filtered one:

$$(\chi^2)_k^{k-1} = \chi_k^2$$

The 'prediction' and 'filtering' steps are repeated as many times as many measurents of the state vector we have.

A.4 Transport

The transport is divided into two steps, the first being simply a change of variables. If a track is described by a set of track parameters, x_k, at a particular point (reference surface), it will be described by another set of parameters, $x_{k+1} = f(x_k)$, at another point on the track. It is then easy to express the variance matrix at a new point by a simple change of variables. The second part of the transport is to 'update' the track parameters and the error matrix taking into account effects from interactions with the material the particle passes through. The interactions can be divided into two categories. The first one, the multiple Coulomb scattering, as it will be shown in Appendix A.4.3 does not affect the estimated track parameters after transport, it only contributes to the error matrix. The second category is energy loss and changes the track parameters. This also affects the error matrix, not only from the effect of straggling in the energy loss, but also by a more subtle effect which occurs when the curvature is changed.

A.4.1 Extrapolation

If we already got the information of a candidate track on the k-th pad row, then the Kalman state $x_{k|k}$ and the covariance matrix $C_{k|k}$ are extrapolated to the next, i.e. (k+1)-th, pad row according to the Kalman equations given in Appendix A.3 by means of track model described by equations 3.3 and by error propagation respectively:

$$C_{k|k} \rightarrow C_{k|k+1} = FC_{k|k}F^T, \quad \text{where} \quad \mathrm{F} = \frac{\delta(\mathrm{x_{k|k+1}})}{\delta(\mathrm{x_{k|k}})}. \tag{A.6}$$

The extrapolation has to be computed precisely since this is the first crucial step for the method.

To get the matrix of the derivatives, F above, and thus the extrapolation of the covariance matrix, one should first express the state vector $x_{k|k+1}$ as function of the state vector $x_{k|k}$, defining the location of $x_{k|k}$ as the intersection of the helix with the plane (yz) at $x = x_k$. To simplify the calculations we assume that the curvature C and the dip angle λ are constant over the elementary extrapolation step. This is a valid assumption since the extrapolation is always going from one measurement plane to the next one and the distance between two consecutive measurement planes varies from 1 cm to 1.5 cm.

According to Eq. (3.3)

$$y_k = y_0 - \frac{1}{C}\sqrt{1-(Cx_k-\eta)^2} \tag{A.7}$$

$$y_{k+1} = y_0 - \frac{1}{C}\sqrt{1-(Cx_{k+1}-\eta)^2} \tag{A.8}$$

Introducing

$$dx = x_{k+1} - x_k,\ dy = y_{k+1} - y_k,\ c_1 = Cx_k - \eta,\ c_2 = Cx_{k+1} - \eta \tag{A.9}$$

and

$$r_1 = 1 - {c_1}^2,\ r_2 = 1 - {c_2}^2$$

we can rewrite Eq. (A.9) as

$$dy = \frac{1}{C} \cdot \frac{{r_1}^2 - {r_2}^2}{r_1 - r_2}.$$

Working out the nominator we find that

$${r_1}^2 - {r_2}^2 = C \cdot dx(c_1 + c_2)$$

and thus

$$y_{k+1} = y_k + dx \cdot (c_1 + c_2)/(r_1 + r_2). \tag{A.10}$$

Similarly, one can write

$$\tan\lambda = \frac{dz}{\sqrt{dx^2 + dy^2}}, \quad \text{where} \quad \mathrm{dz = z_{k+1} - z_k}$$

and thereby

$$z_{k+1} = z_k + (\sqrt{dx^2 + dy^2}) \cdot \tan\lambda.$$

Taking into account that the dip angle λ can be considered constant for an elementary step and using the expression calculated above for dy, one finds

$$z_{k+1} = z_k + dx \cdot \frac{c_1 + c_2}{c_1 r_1 + c_2 r_2} \cdot \tan\lambda. \tag{A.11}$$

For completeness we write the other parameters of the Kalman state at $x = x_{k+1}$:

$$\sin\phi_{k+1} = Cx_{k+1} - \eta \tag{A.12}$$
$$\tan\lambda_{k+1} = \tan\lambda_k. \tag{A.13}$$
$$C_{k+1} = C_k \tag{A.14}$$

A.4.2 Matrix of derivatives (F)

For a helix, the transport matrix F of the extrapolated state vector $x_{k|k+1}$ with respect to the starting values $x_{k|k}$ can be calculated analytically starting from the set of equations A.10- A.12 of the track parameters at the new position. The non-vanishing off-diagonal derivatives then read:

$$\begin{aligned}
&\frac{\delta y_{k+1}}{\delta(\sin\phi_k)} = -dx \cdot \frac{2 \cdot rr + cc \cdot (\frac{c_1}{r_1} + \frac{c_2}{r_2})}{rr^2} \\
&\frac{\delta y_{k+1}}{\delta C} = dx \cdot \frac{rr \cdot xx + cc \cdot \frac{c_1 x_k}{r_1} + \frac{c_2 x_{k+1}}{r_2}}{rr^2} \\
&\frac{\delta z_{k+1}}{\delta(\sin\phi_k)} = -dx \cdot \tan\lambda \cdot \frac{(2 \cdot cr + cc \cdot (\frac{c_2 c_1}{r_1} - r_1 + \frac{c_1 c_2}{r_2} - r_2))}{cr^2} \\
&\frac{\delta z_{k+1}}{\delta(\tan\lambda)} = dx \cdot \frac{cc}{cr} \\
&\frac{\delta z_{k+1}}{\delta C} = dx \cdot \tan\lambda \cdot \frac{(cr \cdot xx - cc \cdot (r_1 x_{k+1} - \frac{c_2 c_1 x_k}{r_1} + r_2 x_k - \frac{c_1 c_2 x_{k+1}}{r_2}))}{cr^2},
\end{aligned}$$

where

$$rr = r_1 + r_2, \quad cc = c_1 + c_2, \quad xx = x_k + x_{k+1}, \quad cr = c_1 r_2 + c_2 r_1.$$

This allows us to compute the extrapolated error matrix according to Eq. (A.6). To render the algorithm faster, as $C_{k|k}$ is a symmetric matrix, we write Eq. (A.6) as:

$$FC_{k|k}F^T = (F - I + I)C_{k|k}(F - I + I)^T = C_{k|k} + fC_{k|k}f^T + fC_{k|k} + C_{k|k}f^T,$$

where $f = F - I$, and I is the identity matrix.

A.4.3 Multiple scattering

Multiple scattering results in a random deflection of the charged particle from the trajectory, as evaluated by the equations of motion in vacuum refeq:Lorentz, by elastic scattering off the electrons or the nuclei of the matter traversed by the particle. If the material traversed is sufficiently thick, there will be a random offset in the position of the particle as well. The relevant properties of the material can be summarized in a single constant, the radiation length X_0. The actual length x of the material traversed by particle depends on the angle of incidence. For our TPC, which is a highly homogeneous gaseous detector, the ratio $d = x/X_0$ is $d \ll 1$. As the variance of the offset in the position of the track is $\sim d^3$ [235], the offset can be fully neglected. Thus, we can safely assume that multiple scattering affects only the track directions leaving the track position unchanged. Using this approximation and letting θ_1 and θ_2 be the projected scattering angles in two directions orthogonal to each other and to the tangent of the trajectory we can write the general formula for the covariance matrix of the multiple scattering:

$$Q_k = \frac{\delta(y_k, z_k, \sin\phi_k, \tan\lambda_k, C_k)}{\delta(\theta_1, \theta_2)} \begin{pmatrix} \langle {\theta_1}^2 \rangle & 0 \\ 0 & \langle {\theta_1}^2 \rangle \end{pmatrix} \left[\frac{\delta(y_k, z_k, \sin\phi_k, \tan\lambda_k, C_k)}{\delta(\theta_1, \theta_2)} \right]^T$$

where the index k denotes the detector surface (pad row) at which the track is propagated. After few trivial calculations one can find the relations between the two angles, λ and ϕ, which describe the direction of the track and the multiple scattering angles (θ_1 and θ_2):

$$\delta\lambda = \theta_1, \quad \delta\phi = \frac{\theta_2}{\cos\lambda}.$$

These relations can be obtained through the following calculations. Let us define two orthogonal unitary vectors

$$\vec{e_1} = \begin{pmatrix} \cos\phi\cos\lambda \\ \sin\phi\cos\lambda \\ \sin\lambda \end{pmatrix} \quad \text{and} \quad \vec{e_2} = \begin{pmatrix} -\sin\phi \\ \cos\phi \\ 0 \end{pmatrix}.$$

The third vector can be constructed via

$$\vec{e_3} = \vec{e_1} \times \vec{e_2} = \begin{pmatrix} -\cos\phi\sin\lambda \\ -\sin\phi\sin\lambda \\ \cos\lambda \end{pmatrix}$$

The effect of multiple scattering will change the vector $\vec{e_1}$ to:

$$\vec{e_1}' = \vec{e_1} + \theta_2 \cdot \vec{e_2} + \theta_1 \cdot \vec{e_3}$$

If we write down the last two components of this vector and expand them in Taylor series around λ and ϕ respectively, from

$$\sin\lambda' = \sin\lambda + \theta_1 \cdot \cos\lambda$$

it becomes obvious that

$$\delta\lambda = \theta_1.$$

Analogously, from

$$\sin\phi^{'}\cos\lambda^{'} = \sin\phi\cos\lambda + \theta_2 \cdot \cos\phi - \theta_1 \cdot \sin\phi\sin\lambda$$

and

$$\begin{aligned}\sin\phi^{'}\cos\lambda^{'} &= \sin\phi^{'}\cos\lambda - \sin\phi^{'}\sin\lambda\cdot\delta\lambda \\ &= \sin\phi\cos\lambda + \cos\lambda\cdot\delta\phi\cdot\cos\phi - \theta_1\cdot\sin\phi\sin\lambda + \cdots\end{aligned}$$

it becomes obvious that

$$\delta\phi = \frac{\theta_2}{\cos\lambda}.$$

Because of symmetry, θ_1 and θ_2 are uncorrelated (although not fully independent) and their distribution is identical. The central limit theorem allows us to approximate this distribution by a Gaussian distribution with zero mean, again because of symmetry, and with the variance as given by the Rossi-Greisen formula

$$\langle\theta_1^2\rangle = \langle\theta_2^2\rangle = \langle\theta^2\rangle = kd(m^2+p^2)/p^4, \quad k = (0.0141\ \mathrm{GeV})^2$$

where m and p are the mass and respective momentum of the particle which crosses the material, and $d = x/X_0$ is the number of radiation lengths actually traversed by the particle. In fact, there is a further logarithmic correction to the variance (see for instance [247, 248]) which violates the additivity of variance for independent stochastic variables. Given the fact that the continuous matter between two consecutive pad rows in TPC can be approximated with an infinitely thin scatterer and in gas the effect of multiple scattering between two rows is small we therefore neglect this correction here[1].

Under the assumptions we made, the formula for Q_k becomes:

$$\begin{aligned}Q_k &= \langle\theta^2\rangle\frac{\delta(y_k,z_k,\sin\phi_k,\tan\lambda_k,C_k)}{\delta(\lambda_k,\phi_k)}\frac{\delta(\lambda_k,\phi_k)}{\delta(\theta_1,\theta_2)}\left[\frac{\delta(\lambda_k,\phi_k)}{\delta(\theta_1,\theta_2)}\right]^T\left[\frac{\delta(y_k,z_k,\sin\phi_k,\tan\lambda_k,C_k)}{\delta(\lambda_k,\phi_k)}\right]^T \\ &= \langle\theta^2\rangle J_k\begin{pmatrix}1 & 0\\ 0 & \frac{1}{\cos^2\lambda_k}\end{pmatrix}{J_k}^T,\end{aligned}$$

where

$$J_k = \frac{\delta(y_k,z_k,\sin\phi_k,\tan\lambda_k,C_k)}{\delta(\lambda_k,\phi_k)}.$$

[1] It should be noted though that the distribution of the multiple scattering angle is non-Gaussian, having long tails outside a more or less Gaussian core. These tails have their origin in the form of single scattering distribution, and persist also for rather thick scatterers. For media with thickness above X_0 the tails are dominated by hadronic scattering

Using

$$\frac{\delta C_k}{\delta \lambda_k} = \frac{\delta C_k}{\delta p_T}\frac{\delta p_T}{\delta \lambda_k} = \frac{const}{{p_T}^2} p \sin\lambda_k = C_k \frac{p_L}{p_T} = C_k \tan\lambda_k,$$
$$\frac{\delta(\tan\lambda_k)}{\delta\lambda_k} = 1 + \tan^2\lambda_k,\ \frac{\delta(\sin\phi_k)}{\delta\lambda_k} = \frac{\delta(\sin\phi_k)}{\delta C_k}\frac{\delta C_k}{\delta\lambda_k} = x_k C_k \tan\lambda_k,$$
$$\frac{\delta(\tan\lambda_k)}{\delta\phi_k} = 0,\ \frac{\delta C_k}{\delta\phi_k} = 0,\ \frac{1}{\cos^2\lambda_k} = 1 + \tan^2\lambda_k,$$
$$\cos^2\phi_k = 1 - (C_k x_k - \eta)^2$$

and keeping in mind that track position is unchanged by multiple scattering in our case, we calculate the covariance matrix elements which need to be updated:

$$\begin{aligned}
C_{\sin\phi_k|\sin\phi_k} &= \\
&\quad C_{\sin\phi_k|\sin\phi_k} + \langle\theta^2\rangle \cdot (2\eta\sin\phi_k \cdot \tan^2\lambda_k + 1 - \sin^2\phi_k + \tan^2\lambda_k + \eta^2\tan^2\lambda_k) \\
C_{\sin\phi_k|\tan\lambda_k} &= C_{\sin\phi_k|\tan\lambda_k} + \langle\theta^2\rangle \cdot \left[x_k C_k \tan\lambda_k \cdot (1 + \tan^2\lambda_k)\right] \\
C_{\sin\phi_k|C_k} &= C_{\sin\phi_k|C_k} + \langle\theta^2\rangle \cdot x_k {C^2}_k \tan^2\lambda_k \\
C_{\tan\lambda_k|\tan\lambda_k} &= C_{\tan\lambda_k|\tan\lambda_k} + \langle\theta^2\rangle \cdot (1 + \tan^2\lambda_k) \\
C_{\tan\lambda_k|C_k} &= C_{\tan\lambda_k|C_k} + \langle\theta^2\rangle \cdot C_k \tan\lambda_k \cdot (1 + tan^2\lambda_k) \\
C_{C_k|C_k} &= C_{C_k|C_k} + \langle\theta^2\rangle \cdot {C^2}_k \cdot \tan^2\lambda_k.
\end{aligned}$$

A.4.4 Energy loss

The effect of energy loss is implemented as a change of curvature C for a given step according to the following formula:

$$C_{new} = C_{old}(1 - \frac{\Delta C}{C_{old}}) = C_{old}(1 - \frac{E}{p^2}\Delta E) \tag{A.15}$$

where C_{new} and C_{old} are track curvature before and after a pad row crossing, E and p are particle energy and momentum, and the energy loss ΔE is calculated with a simplified Bethe-Bloch formula reduced to the case of pions:

$$\Delta E = \frac{0.153}{\beta^2}(\ln\frac{5940\cdot\beta^2}{1-\beta^2})\Delta X$$

with β being the particle's velocity and ΔX the path length of particle expressed in g/cm^2.

The relation A.15 can be obtained in the following way. Let E_{new} and p_{new} be particle's energy, respective momentum after pad row crossing

$$E_{new} = E + \Delta E, \qquad p_{new} = \frac{K}{C_{new}}\sqrt{1 + \tan^2\lambda}.$$

With

$$p_{old} = \frac{K}{C_{old}}\sqrt{1+\tan^2\lambda}$$

and using $E_{new}^2 = p_{new}^2 + m^2$ and the above relations, it is easy to see that C_{new} can be written as

$$C_{new} = C_{old}\cdot\frac{p^2}{\sqrt{(E^2+m^2)(p^2+2E\Delta E+\Delta E^2)}} = C_{old}\cdot p^2(\frac{1}{p^2} - \frac{E\Delta E}{p^4} + \cdots) = C_{old}(1-\frac{E}{p^2}\Delta E).$$

Bibliography

[1] Ulrich W. Heinz. The little bang: Searching for quark-gluon matter in relativistic heavy-ion collisions. *Nucl. Phys.*, A685:414–431, 2001.

[2] P. Giubellino. *SPS* experiments with the lead beam. *Nucl. Phys.*, A699:103–113, 2002.

[3] Johann Rafelski and Berndt Muller. Strangeness production in the quark - gluon plasma. *Phys. Rev. Lett.*, 48:1066, 1982.

[4] K. Fanebust et al. Results on hyperon production from $NA57$. *J. Phys.*, G28:1607–1614, 2002.

[5] F. Antinori et al. Production of strange and multistrange hadrons in nucleus nucleus collisions at the *SPS*. *Nucl. Phys.*, A661:130–139, 1999.

[6] E. Andersen et al. Strangeness enhancement at mid-rapidity in Pb+Pb collisions at $158 - A\cdot$ GeV/c. *Phys. Lett.*, B449:401–406, 1999.

[7] T. Matsui and H. Satz. J/ψ suppression by quark - gluon plasma formation. *Phys. Lett.*, B178:416, 1986.

[8] M. C. Abreu et al. Anomalous J/ψ suppression in $Pb + Pb$ interactions at 158 GeV/c per nucleon. *Phys. Lett.*, B410:337–343, 1997.

[9] M. C. Abreu et al. Observation of a threshold effect in the anomalous J/ψ suppression. *Phys. Lett.*, B450:456–466, 1999.

[10] R. Rapp and J. Wambach. Chiral symmetry restoration and dileptons in relativistic heavy-ion collisions. *Adv. Nucl. Phys.*, 25:1, 2000.

[11] A. Cherlin and S. Yurevich. Preliminary results from the 2000 run of *CERES* on low-mass e^+e^- pair production in $Pb + Au$ collisions at $158 - A\cdot$ GeV. *J. Phys.*, G30:S1007–S1011, 2004.

[12] S. Damjanovic. First measurement of the ρ spectral function in nuclear collisions. To appear in the proceedings of 18th International Conference on Ultrarelativistic Nucleus-Nucleus Collisions: Quark Matter 2005 (QM 2005), Budapest, Hungary, 4-9 Aug 2005.

[13] S. S. Adler et al. Elliptic flow of identified hadrons in $Au + Au$ collisions at $\sqrt{s_{NN}} = 200$ GeV. *Phys. Rev. Lett.*, 91:182301, 2003.

[14] S. A. Voloshin. Anisotropic flow. *Nucl. Phys.*, A715:379–388, 2003.

[15] M. Csanad et al. Universal scaling of the elliptic flow and the perfect hydro picture at $RHIC$. *nucl-th/0512078*, 2005.

[16] Paul Sorensen. Particle dependence of elliptic flow in $Au + Au$ collisions at $\sqrt{s_{NN}} = 200$ GeV. *J. Phys.*, G30:S217–S222, 2004.

[17] K. Adcox et al. Suppression of hadrons with large transverse momentum in central $Au + Au$ collisions at $\sqrt{s_{NN}} = 130$ GeV. *Phys. Rev. Lett.*, 88:022301, 2002.

[18] S. S. Adler et al. Suppressed π^0 production at large transverse momentum in central $Au + Au$ collisions at $\sqrt{s_{NN}} = 200$ GeV. *Phys. Rev. Lett.*, 91:072301, 2003.

[19] J. Adams et al. Transverse momentum and collision energy dependence of high p_T hadron suppression in $Au + Au$ collisions at ultrarelativistic energies. *Phys. Rev. Lett.*, 91:172302, 2003.

[20] J. Adams et al. Evidence from $d + Au$ measurements for final-state suppression of high p_T hadrons in $Au + Au$ collisions at $RHIC$. *Phys. Rev. Lett.*, 91:072304, 2003.

[21] C. Adler et al. Disappearance of back-to-back high p_T hadron correlations in central $Au + Au$ collisions at $\sqrt{s_{NN}} = 200$ GeV. *Phys. Rev. Lett.*, 90:082302, 2003.

[22] Carlos A. Salgado and Urs Achim Wiedemann. Medium modification of jet shapes and jet multiplicities. *Phys. Rev. Lett.*, 93:042301, 2004.

[23] Nestor Armesto, Carlos A. Salgado, and Urs Achim Wiedemann. Low-p_T collective flow induces high-p_T jet quenching. *Phys. Rev.*, C72:064910, 2005.

[24] Jorg Ruppert and Berndt Muller. Waking the colored plasma. *Phys. Lett.*, B618:123–130, 2005.

[25] N. N. Ajitanand. Two and three particle flavor dependent correlations. *nucl-ex/0510040*, 2005.

[26] W. G. Holzmann et al. Multiparticle angular correlations: A probe for the sQGP at $RHIC$. *J. Phys. Conf. Ser.*, 27:80–87, 2005.

[27] S. S. Adler et al. Jet structure of baryon excess in $Au+Au$ collisions at $\sqrt{s_{NN}} = 200$ GeV. *Phys. Rev.*, C71:051902, 2005.

[28] S. S. Adler et al. Jet structure from dihadron correlations in $d + Au$ collisions at $\sqrt{s_{NN}} = 200$ GeV. *nucl-ex/0510021*, 2005.

[29] Roy A. Lacey. Elliptic flow measurements with the $PHENIX$ detector. *Nucl. Phys.*, A698:559–563, 2002.

[30] Pasi Huovinen. Hydrodynamical description of collective flow. *nucl-th/0305064*, 2003.

[31] Edward V. Shuryak. What $RHIC$ experiments and theory tell us about properties of quark-gluon plasma? *Nucl. Phys.*, A750:64–83, 2005.

[32] Roy A. Lacey. The role of elliptic flow correlations in the discovery of the sQGP at $RHIC$. *nucl-ex/0510029*, 2005.

[33] Miklos Gyulassy and Larry McLerran. New forms of QCD matter discovered at $RHIC$. *Nucl. Phys.*, A750:30–63, 2005.

[34] Ulrich W. Heinz. Equation of state and collective dynamics. *nucl-th/0504011*, 2005.

[35] Ulrich W. Heinz. Thermalization at $RHIC$. *AIP Conf. Proc.*, 739:163–180, 2005.

[36] J. Breitweg et al. $ZEUS$ results on the measurement and phenomenology of $F2$ at low x and low Q^2. *Eur. Phys. J.*, C7:609–630, 1999.

[37] Edmond Iancu. The colour glass condensate. *Nucl. Phys.*, A715:219–232, 2003.

[38] Edmond Iancu and Larry D. McLerran. Saturation and universality in QCD at small x. *Phys. Lett.*, B510:145–154, 2001.

[39] I. Arsene et al. Quark gluon plasma and color glass condensate at $RHIC$?: The perspective from the $BRAHMS$ experiment. *Nucl. Phys.*, A757:1–27, 2005.

[40] Larry McLerran. What is the evidence for the color glass condensate? *hep-ph/0402137*, 2004.

[41] Larry McLerran. $RHIC$ physics: The quark gluon plasma and the color glass condensate: 4 lectures. *hep-ph/0311028*, 2003.

[42] J. Adams et al. Experimental and theoretical challenges in the search for the quark gluon plasma: The $STAR$ collaboration's critical assessment of the evidence from $RHIC$ collisions. *Nucl. Phys.*, A757:102–183, 2005.

[43] K. Adcox et al. Formation of dense partonic matter in relativistic nucleus-nucleus collisions at $RHIC$: Experimental evaluation by the $PHENIX$ collaboration. *Nucl. Phys.*, A757:184–283, 2005.

[44] B. B. Back et al. The *PHOBOS* perspective on discoveries at *RHIC*. *Nucl. Phys.*, A757:28–101, 2005.

[45] K. J. Eskola, K. Kajantie, P. V. Ruuskanen, and K. Tuominen. Scaling of transverse energies and multiplicities with atomic number and energy in ultra-relativistic nuclear collisions. *Nucl. Phys.*, B570:379–389, 2000.

[46] Ivan Vitev. Jet tomography. *J. Phys.*, G30:S791–S800, 2004.

[47] Alberto Accardi et al. Hard probes in heavy ion collisions at the *LHC*: Jet physics. *hep-ph/0310274*, 2003.

[48] M. Bedjidian et al. Hard probes in heavy ion collisions at the *LHC*: Heavy flavour physics. *hep-ph/031104*, 2003.

[49] R. Vogt. Heavy ion physics at the *LHC*. *Nucl. Phys.*, A752:447c–456c, 2005.

[50] Carlos A. Salgado and Urs Achim Wiedemann. *RHIC* results from *LHC* perspectives. To appear in the proceedings of 18th International Conference on Ultrarelativistic Nucleus-Nucleus Collisions: Quark Matter 2005 (QM 2005), Budapest, Hungary, 4-9 Aug 2005.

[51] Nestor Armesto, Andrea Dainese, Carlos A. Salgado, and Urs Achim Wiedemann. Testing the color charge and mass dependence of parton energy loss with heavy-to-light ratios at *RHIC* and *LHC*. *Phys. Rev.*, D71:054027, 2005.

[52] Berndt Muller. Heavy ions: Prospects at the *LHC*. *hep-ph/0410115*, 2004.

[53] (ed.) Carminati, F. et al. *ALICE* Physics performance report, volume I. *J. Phys.*, G30:1517–1763, 2004.

[54] Edward V. Shuryak. Two stage equilibration in high-energy heavy ion collisions. *Phys. Rev. Lett.*, 68:3270–3272, 1992.

[55] P. Koch, B. Muller, and J. Rafelski. Strangeness production and evolution in quark gluon plasma. *Z. Phys.*, A324:453–463, 1986.

[56] Johann Rafelski and Jean Letessier. Strangeness and quark gluon plasma. *J. Phys.*, G30:S1–S28, 2004.

[57] Johann Rafelski and Jean Letessier. Hadronization of expanding *QGP*. *nucl-th/0511016*, 2005.

[58] J Rafelski. Strangeness and quark gluon plasma. *Phys. Rep.*, 88:331, 1982.

[59] Carsten Greiner. Strangeness in strongly interacting matter. *J. Phys.*, G28:1631–1648, 2002.

[60] K. Hagiwara et al. Review of particle physics. *Phys. Rev.*, D66:010001, 2002.

[61] M. Gluck and E. Reya. Duality predictions for the production of heavy quark systems in QCD. *Phys. Lett.*, B79:453, 1978.

[62] Johann Rafelski and Jean Letessier. Expected production of strange baryons and antibaryons in baryon-poor QGP. *Phys. Lett.*, B469:12–18, 1999.

[63] T. Biro and J. Zimanyi. Quarkochemistry in relativistic heavy ion collisions. *Phys. Lett.*, B113:6, 1982.

[64] J. Rafelski. Strangeness production in quark gluon plasma. *Nucl. Phys.*, A418:215c, 1984.

[65] P. Koch, B. Muller, and J. Rafelski. Strangeness in relativistic heavy ion collisions. *Phys. Rep.*, 142:167, 1986.

[66] J. Kapusta and A. Mekjian. How much strangeness production is there in ultrarelativistic nucleus-nucleus collisions? *Phys. Rev.*, D33:1304, 1986.

[67] J Schaffner-Bielich. What is so special about strangeness in hot matter? *J. Phys.*, G30:R245–R262, 2004.

[68] Duncan M. Elliott and Dirk H. Rischke. Chemical equilibration of quarks and gluons at $RHIC$ and LHC energies. *Nucl. Phys.*, A671:583–608, 2000.

[69] Josef Sollfrank and Ulrich W. Heinz. The role of strangeness in ultrarelativistic nuclear collisions. *nucl-th/9505004*, 1995.

[70] (ed.) Hallman, T., D. Karzeev, J. Mitchell, and T. Ulrich. Quark matter 2001. *Elsevier*, 2002.

[71] (ed.) Gutbrod, H., J. Aichelin, and K. Werner. Quark matter 2002. *Elsevier*, 2003.

[72] (ed.) Antinori, F. et al. Hot quarks. *J. Phys.*, G31, 2005. Proceedings, Workshop for Young Scientists on the Physics of Ultrarelativistic Nucleus Nucleus Collisions, HQ'04, Snakedance, Taos Valley, USA, July 18- 24, 2004.

[73] Proceedings of 18th International Conference on Ultrarelativistic Nucleus-Nucleus Collisions: Quark Matter 2005 (QM 2005), Budapest, Hungary, 4-9 Aug 2005. To be published.

[74] J. Cleymans and K. Redlich. Unified description of freeze-out parameters in relativistic heavy ion collisions. *Phys. Rev. Lett.*, 81:5284–5286, 1998.

[75] R. Hagedorn. Thermodynamics of strong interactions. CERN-71-12.

[76] A. Wroblewski. On the strange quark suppression factor in high-energy collisions. *Acta Phys. Polon.*, B16:379–392, 1985.

[77] P. Braun-Munzinger, J. Cleymans, H. Oeschler, and K. Redlich. Maximum relative strangeness content in heavy ion collisions around $30 - A\cdot$ GeV. *Nucl. Phys.*, A697:902–912, 2002.

[78] Rajiv V. Gavai and Sourendu Gupta. The continuum limit of quark number susceptibilities. *Phys. Rev.*, D65:094515, 2002.

[79] S. V. Afanasev et al. New results from $NA49$. *Nucl. Phys.*, A698:104–111, 2002.

[80] C. Blume. Energy dependence of hadronic observables. *J. Phys.*, G31:S57–S68, 2005.

[81] C. Adler et al. Results from the $STAR$ experiment. *Nucl. Phys.*, A698:64–77, 2002.

[82] W. Cassing. Excitation function of strangeness in $A + A$ reactions from SIS to $RHIC$ energies. *Nucl. Phys.*, A661:468–471, 1999.

[83] Carsten Greiner. Collective effects in microscopic transport models. *Nucl. Phys.*, A715:75–84, 2003.

[84] H. Weber, E. L. Bratkovskaya, W. Cassing, and Horst Stoecker. Hadronic observables from SIS to SPS energies: Anything strange with strangeness? *Phys. Rev.*, C67:014904, 2003.

[85] F. Becattini, J. Cleymans, A. Keranen, E Suhonen, and K. Redlich. Features of particle multiplicities and strangeness production in central heavy ion collisions between $1.7 - A\cdot$ GeV/c and $158 - A\cdot$ GeV/c. *Phys. Rev.*, C64:024901, 2001.

[86] Jean Letessier and Johann Rafelski. Hadron production and phase changes in relativistic heavy ion collisions. *nucl-th/0504028*, 2005.

[87] N. Cabibbo and G. Parisi. Exponential hadronic spectrum and quark liberation. *Phys. Lett.*, B59:67, 1975.

[88] S. D. Katz. Equation of state from lattice QCD. *hep-ph/0511166*, 2005.

[89] F. Karsch, E. Laermann, and A. Peikert. The pressure in 2, 2+1 and 3 flavour QCD. *Phys. Lett.*, B478:447–455, 2000.

[90] Z. Fodor and S. D. Katz. Lattice determination of the critical point of QCD at finite T and μ. *JHEP*, 03:014, 2002.

[91] Z. Fodor, S. D. Katz, and K. K. Szabo. The QCD equation of state at nonzero densities: Lattice result. *Phys. Lett.*, B568:73–77, 2003.

[92] Z. Fodor and S. D. Katz. Critical point of QCD at finite T and μ, lattice results for physical quark masses. *JHEP*, 04:050, 2004.

[93] K. Tuominen. Deconfinement and chiral symmetry: Competing orders. *hep-ph/0408330*, 2004.

[94] Agnes Mocsy, Francesco Sannino, and Kimmo Tuominen. Effective lagrangians for QCD: Deconfinement and chiral symmetry restoration. *hep-ph/0401149*, 2004.

[95] Frithjof Karsch. Lattice QCD at non-zero chemical potential and the resonance gas model. *Prog. Theor. Phys. Suppl.*, 153:106–117, 2004.

[96] John B. Kogut et al. Studies of chiral symmetry breaking in $SU(2)$ lattice gauge theory. *Nucl. Phys.*, B225:326, 1983.

[97] J. B. Kogut, D. K. Sinclair, and K. C. Wang. Towards the continuum limit of the thermodynamics of lattice QCD with a realistic quark spectrum. *Phys. Lett.*, B263:101–106, 1991.

[98] Kieran Holland and Uwe-Jens Wiese. The center symmetry and its spontaneous breakdown at high temperatures. *hep-ph/0011193*, 2000.

[99] Janos Polonyi. Physics of the quark-gluon plasma. *Heavy Ion Phys.*, 2:123, 1995.

[100] Jurgen Schaffner-Bielich. Effective restoration of the $U(1)A$ symmetry in the $SU(3)$ linear sigma model. *Phys. Rev. Lett.*, 84:3261, 2000.

[101] Johann Rafelski and Jean Letessier. Strangeness and the discovery of quark-gluon plasma. *hep-ph/0506011*, 2005.

[102] Jean Letessier, Ahmed Tounsi, Ulrich W. Heinz, Josef Sollfrank, and Johann Rafelski. Strangeness conservation in hot nuclear fireballs. *Phys. Rev.*, D51:3408–3435, 1995.

[103] Robert D. Pisarski and Frank Wilczek. Remarks on the chiral phase transition in chromodynamics. *Phys. Rev.*, D29:338–341, 1984.

[104] Ping Chen et al. Toward the chiral limit of QCD: Quenched and dynamical domain wall fermions. *hep-lat/9812011*, 1998.

[105] Steven A. Gottlieb et al. Thermodynamics of lattice QCD with two light quark flavours on a 16**3 x 8 lattice. II. *Phys. Rev.*, D55:6852–6860, 1997.

[106] E. V. Shuryak and G. E. Brown. Matter-induced modification of resonances at $RHIC$ freeze-out. *Nucl. Phys.*, A717:322–335, 2003.

[107] Ralf Rapp. $\pi^+\pi^-$ emission in high-energy nuclear collisions. *Nucl. Phys.*, A725:254–268, 2003.

[108] G. E. Brown and Mannque Rho. Scaling effective lagrangians in a dense medium. *Phys. Rev. Lett.*, 66:2720–2723, 1991.

[109] Subrata Pal, C. M. Ko, and Zi-wei Lin. ϕ meson production in relativistic heavy ion collisions. *Nucl. Phys.*, A707:525–539, 2002.

[110] E. Oset and A. Ramos. ϕ decay in nuclei. *Nucl. Phys.*, A679:616–628, 2001.

[111] A. Mishra, E. L. Bratkovskaya, J. Schaffner-Bielich, S. Schramm, and Horst Stoecker. Kaons and antikaons in hot and dense hadronic matter. *Phys. Rev.*, C70:044904, 2004.

[112] Edward V. Shuryak and V. Thorsson. Kaon modification in hot hadronic matter. *Nucl. Phys.*, A536:739–749, 1992.

[113] Laura Holt and Kevin Haglin. Short-lived ϕ mesons. *J. Phys.*, G31:S245–S251, 2005.

[114] Stephen C. Johnson, Barbara V. Jacak, and Axel Drees. Rescattering of vector meson daughters in high-energy heavy ion collisions. *Eur. Phys. J.*, C18:645–649, 2001.

[115] M. Asakawa and C. M. Ko. Secondary ϕ meson peak as a indicator of QCD phase transition in ultrarelativistic heavy ion collisions. *Phys. Rev.*, C50:3064–3068, 1994.

[116] M. Asakawa and C. M. Ko. ϕ meson mass in hot and dense matter. *Nucl. Phys.*, A572:732–748, 1994.

[117] Pin-zhen Bi and Johann Rafelski. Decay of ϕ in hot matter. *Phys. Lett.*, B262:485–491, 1991.

[118] D. Cabrera and M. J. Vicente Vacas. ϕ meson mass and decay width in nuclear matter. *Phys. Rev.*, C67:045203, 2003.

[119] Wade Smith and Kevin L. Haglin. Collision broadening of the ϕ meson in baryon rich hadronic matter. *Phys. Rev.*, C57:1449–1453, 1998.

[120] D. Lissauer and Edward V. Shuryak. K meson modification in hot hadronic matter may be detected via ϕ meson decays. *Phys. Lett.*, B253:15–18, 1991.

[121] S. V. Afanasev et al. Production of ϕ mesons in $p+p$ $p+Pb$ and central $Pb+Pb$ collisions at $158 - A\cdot$ GeV. *Phys. Lett.*, B491:59–66, 2000.

[122] Zhang-bu Xu. Resonance studies at $STAR$. *Nucl. Phys.*, A698:607–610, 2002.

[123] S. S. Adler et al. Production of ϕ mesons at mid-rapidity in $\sqrt{s_{NN}} = 200$ GeV $Au + Au$ collisions at $RHIC$. *Phys. Rev.*, C72:014903, 2005.

[124] J. Adams et al. ϕ meson production in $Au+Au$ and $p+p$ collisions at $\sqrt{s_{NN}} =$ 200 GeV. *Phys. Lett.*, B612:181–189, 2005.

[125] D. Adamova et al. Leptonic and charged kaon decay modes of the ϕ meson measured in heavy-ion collisions at the $CERN\ SPS$. *nucl-ex/0512007*, 2005.

[126] Alexander Kozlov. ϕ production as seen in e^+e^- and $K^+\ K^-$ decay channels in $Au+Au$ collisions by $PHENIX$ at $\sqrt{s_{NN}} = 200$ GeV. *nucl-ex/0510016*, 2005.

[127] V. Friese. Production of strange resonances in $C + C$ and $Pb + Pb$ collisions at $158 - A\cdot$ GeV. *Nucl. Phys.*, A698:487–490, 2002.

[128] C. M. Ko and M. Asakawa. Double ϕ peaks as a signature for the QCD phase transition. *Nucl. Phys.*, A566:447c–450c, 1994.

[129] M. Asakawa and C. M. Ko. Seeing the QCD phase transition with ϕ mesons. *Phys. Lett.*, B322:33–37, 1994.

[130] Johann Rafelski, Jean Letessier, and Giorgio Torrieri. Strange hadrons and their resonances: A diagnostic tool of QGP freeze-out dynamics. *Phys. Rev.*, C64:054907, 2001.

[131] Johann Rafelski and Jean Letessier. Probing dense matter with strange hadrons. *hep-ph/0111467*, 2001.

[132] R Bellwied. Strangeness at $RHIC$ recent results from $STAR$. *J. Phys.*, G31:S675–S684, 2005.

[133] R Bellwied. Strange hard probes to characterize the partonic medium at $RHIC$. *Nucl. Phys.*, A749:257c–267c, 2005.

[134] K. Geiger. QCD based space-time description of high-energy nuclear collisions. *Nucl. Phys.*, A566:257c–268c, 1994.

[135] E. Shuryak. A strongly coupled quark-gluon plasma. *J. Phys.*, G30:1221–1224, 2004.

[136] Miklos Gyulassy. The QGP discovered at $RHIC$. *nucl-th/0403032*, 2004.

[137] G. Torrieri and J. Rafelski. Strange hadron resonances and QGP freeze-out. *J. Phys.*, G28:1911–1920, 2002.

[138] Giorgio Torrieri and Johann Rafelski. Statistical hadronization probed by resonances. *Phys. Rev.*, C68:034912, 2003.

[139] C. Markert, G. Torrieri, and J. Rafelski. Strange hadron resonances: Freeze-out probes in heavy-ion collisions. *hep-ph/0206260*, 2002.

[140] J. Letessier, G. Torrieri, S. Hamieh, and J. Rafelski. *QGP* fireball explosion. *J. Phys.*, G27:427–438, 2001.

[141] J. Adams et al. K*(892) resonance production in $Au + Au$ and $p + p$ collisions at $\sqrt{s_{NN}} = 200$ GeVat *STAR*. *Phys. Rev.*, C71:064902, 2005.

[142] Olga Barannikova. Freeze-out dynamics at *RHIC*. *Acta Phys. Hung.*, A24:39–44, 2005.

[143] P. Braun-Munzinger, D. Magestro, K. Redlich, and J. Stachel. Hadron production in $Au + Au$ collisions at *RHIC*. *Phys. Lett.*, B518:41–46, 2001.

[144] Huan Z. Huang and Johann Rafelski. Hadronization and quark probes of deconfinement at *RHIC*. *AIP Conf. Proc.*, 756:210–227, 2005.

[145] Sevil Salur. System and energy dependence of strangeness production with *STAR*. *nucl-ex/0509036*, 2005.

[146] G. E. Bruno. New results from the *NA*57 experiment. *J. Phys.*, G30:S717–S724, 2004.

[147] Pasi Huovinen. Anisotropy of flow and the order of phase transition in relativistic heavy ion collisions. *Nucl. Phys.*, A761:296–312, 2005.

[148] P. Huovinen, P. F. Kolb, Ulrich W. Heinz, P. V. Ruuskanen, and S. A. Voloshin. Radial and elliptic flow at *RHIC*: Further predictions. *Phys. Lett.*, B503:58–64, 2001.

[149] D. Teaney, J. Lauret, and Edward V. Shuryak. Hydro + cascade, flow, the equation of state, predictions and data. *Nucl. Phys.*, A698:479–482, 2002.

[150] D. Teaney, J. Lauret, and E. V. Shuryak. A hydrodynamic description of heavy ion collisions at the *SPS* and *RHIC*. *nucl-th/011003*, 2001.

[151] J. Adams et al. Azimuthal anisotropy at *RHIC*: The first and fourth harmonics. *Phys. Rev. Lett.*, 92:062301, 2004.

[152] J. Adams et al. Particle dependence of azimuthal anisotropy and nuclear modification of particle production at moderate p_T in $Au + Au$ collisions at $\sqrt{s_{NN}} = 200$ GeV. *Phys. Rev. Lett.*, 92:052302, 2004.

[153] C. Adler et al. Elliptic flow from two- and four-particle correlations in $Au + Au$ collisions at $\sqrt{s_{NN}} = 130$ GeV. *Phys. Rev.*, C66:034904, 2002.

[154] M. Oldenburg. Azimuthal anisotropy of identified hadrons in 200 GeVau+au collisions. To appear in the proceedings of 18th International Conference on Ultrarelativistic Nucleus-Nucleus Collisions: Quark Matter 2005 (QM 2005), Budapest, Hungary, 4-9 Aug 2005.

[155] H. Masui. Anisotropic flow in 200 GeV $Cu + Cu$ and $Au + Au$ collisions at $PHENIX$. To appear in the proceedings of 18th International Conference on Ultrarelativistic Nucleus-Nucleus Collisions: Quark Matter 2005 (QM 2005), Budapest, Hungary, 4-9 Aug 2005.

[156] Denes Molnar and Miklos Gyulassy. Saturation of elliptic flow at $RHIC$: Results from the covariant elastic parton cascade model MPC. *Nucl. Phys.*, A697:495–520, 2002.

[157] M. Gyulassy, I. Vitev, and X. N. Wang. High p_T azimuthal asymmetry in noncentral $A + A$ at $RHIC$. *Phys. Rev. Lett.*, 86:2537–2540, 2001.

[158] Miklos Gyulassy, Ivan Vitev, Xin-Nian Wang, and Pasi Huovinen. Transverse expansion and high p_T azimuthal asymmetry at $RHIC$. *Phys. Lett.*, B526:301–308, 2002.

[159] Ivan Vitev and Miklos Gyulassy. Jet quenching and the $\bar{p} \geq \pi^-$ anomaly at $RHIC$. *Phys. Rev.*, C65:041902, 2002.

[160] S. S. Adler et al. Mid-rapidity neutral pion production in proton proton collisions at $\sqrt{s_{NN}} = 200$ GeV. *Phys. Rev. Lett.*, 91:241803, 2003.

[161] Miklos Gyulassy, Ivan Vitev, Xin-Nian Wang, and Ben-Wei Zhang. Jet quenching and radiative energy loss in dense nuclear matter. *nucl-th/0302077*, 2003.

[162] Xin-Nian Wang. Why the observed jet quenching at $RHIC$ is due to parton energy loss. *Phys. Lett.*, B579:299–308, 2004.

[163] Xin-Nian Wang and Miklos Gyulassy. Gluon shadowing and jet quenching in $A + A$ collisions at $\sqrt{s_{NN}} = 200$ GeV. *Phys. Rev. Lett.*, 68:1480–1483, 1992.

[164] Miklos Gyulassy and Michael Plumer. Jet quenching as a probe of dense matter. *Nucl. Phys.*, A527:641–644, 1991.

[165] R. J. Fries, B. Muller, C. Nonaka, and S. A. Bass. Hadronization in heavy ion collisions: Recombination and fragmentation of partons. *Phys. Rev. Lett.*, 90:202303, 2003.

[166] Rudolph C. Hwa and C. B. Yang. Recombination model for fragmentation: Parton shower distributions. *Phys. Rev.*, C70:024904, 2004.

[167] Zi-wei Lin and C. M. Ko. Partonic effects on the elliptic flow at $RHIC$. *Phys. Rev.*, C65:034904, 2002.

[168] A. Peshier and W. Cassing. The hot non-perturbative gluon plasma is an almost ideal colored liquid. *Phys. Rev. Lett.*, 94:172301, 2005.

[169] Edward V. Shuryak and Ismail Zahed. Towards a theory of binary bound states in the quark gluon plasma. *Phys. Rev.*, D70:054507, 2004.

[170] Hendrik van Hees and Ralf Rapp. Thermalization of heavy quarks in the quark-gluon plasma. *Phys. Rev.*, C71:034907, 2005.

[171] V. Greco, C. M. Ko, and P. Levai. Parton coalescence and antiproton/pion anomaly at *RHIC*. *Phys. Rev. Lett.*, 90:202302, 2003.

[172] David Hardtke. Jets and dijets in $Au + Au$ and $p + p$ collisions at *RHIC*. *Nucl. Phys.*, A715:272–279, 2003.

[173] M. Gyulassy, P. Levai, and I. Vitev. Non-abelian energy loss at finite opacity. *Phys. Rev. Lett.*, 85:5535–5538, 2000.

[174] Miklos Gyulassy, Peter Levai, and Ivan Vitev. Jet quenching in thin quark-gluon plasmas. I: Formalism. *Nucl. Phys.*, B571:197–233, 2000.

[175] P. Sorensen. Identified particle spectra and jet interactions with the medium. To appear in the proceedings of 18th International Conference on Ultrarelativistic Nucleus-Nucleus Collisions: Quark Matter 2005 (QM 2005), Budapest, Hungary, 4-9 Aug 2005.

[176] Ying Guo. Identified high p_T particle correlation studies in central $Au + Au$ collisions at $\sqrt{s_{NN}} = 200$ GeV. *hep-ex/0403018*, 2004.

[177] (ed.) Morsch, A. et al. *LHC* experimental conditions, ALICE-INT-2002-034, 2002.

[178] C. M. Hung and Edward V. Shuryak. Hydrodynamics near the *QCD* phase transition: Looking for the longest lived fireball. *Phys. Rev. Lett.*, 75:4003–4006, 1995.

[179] Peter F. Kolb and Ulrich W. Heinz. Hydrodynamic description of ultrarelativistic heavy-ion collisions. *nucl-th/0305084*, 2003.

[180] K. J. Eskola, H. Honkanen, H. Niemi, P. V. Ruuskanen, and S. S. Rasanen. *RHIC*-tested predictions for low-p_T and high-p_T hadron spectra in nearly central $Pb + Pb$ collisions at the *LHC*. *Phys. Rev.*, C72:044904, 2005.

[181] B. Muller, R. J. Fries, and S. A. Bass. Thermal recombination: Beyond the valence quark approximation. *Phys. Lett.*, B618:77–83, 2005.

[182] S. A. Bass, R. J. Fries, and B. Muller. Correlations in the parton recombination model. *nucl-th/0510084*. To appear in the proceedings of 18th International Conference on Ultrarelativistic Nucleus-Nucleus Collisions: Quark Matter 2005 (QM 2005), Budapest, Hungary, 4-9 Aug 2005.

[183] V. Greco and C. M. Ko. Quark coalescence and the scaling of hadron elliptic flow. *nucl-th/0505061*, 2005.

[184] R. J. Fries and B. Muller. Heavy ions at *LHC* Theoretical issues. *Eur. Phys. J.*, C34:s279–s285, 2004.

[185] P. Abreu et al. Identified charged particles in quark and gluon jets. *Eur. Phys. J.*, C17:207–222, 2000.

[186] (ed.) Alessandro, B. et al. *ALICE* Physics performance report, volume II. *CERN/LHCC 2005-030*, 5 December 2005.

[187] P. Braun-Munzinger, I. Heppe, and J. Stachel. Chemical equilibration in $Pb+Pb$ collisions at the SPS. *Phys. Lett.*, B465:15–20, 1999.

[188] Jean Letessier and Johann Rafelski. Centrality dependence of strangeness and (anti)hyperon production at $RHIC$. *nucl-th/0506044*, 2005.

[189] Johann Rafelski and Jean Letessier. Non-equilibrium hadrochemistry in QGP hadronization. *hep-ph/0206145*, 2002.

[190] Johann Rafelski and Jean Letessier. Soft hadron relative multiplicities at LHC. *Eur. Phys. J.*, C45:61–72, 2006.

[191] Johann Rafelski and Jean Letessier. Strangeness and thresholds of phase changes in relativistic heavy ion collisions. *hep-ph/0512265*, 2005.

[192] K. J. Eskola, P. V. Ruuskanen, S. S. Rasanen, and K. Tuominen. Multiplicities and transverse energies in central a a collisions at $RHIC$ and LHC from pQCD, saturation and hydrodynamics. *Nucl. Phys.*, A696:715–728, 2001.

[193] Dmitri Kharzeev, Eugene Levin, and Marzia Nardi. Color glass condensate at the LHC: Hadron multiplicities in $p + p$, $p + A$ and $A + A$ collisions. *Nucl. Phys.*, A747:609–629, 2005.

[194] Constantinos A. Loizides. Jet physics in $ALICE$: Ph.D thesis. *nucl-ex/0501017*, 2005.

[195] ALICE Collaboration. *ALICE* Technical Design Report of the Inner Tracking System (ITS), CERN-LHCC-99-12, 1999.

[196] ALICE Collaboration. *ALICE* Technical Design Report of the Time Projection Chamber, CERN-OPEN-2000-183, 2000.

[197] ALICE Collaboration. *ALICE* Technical Design Report of the Transition Radiation Detector, CERN/LHCC/2001-021, 2001.

[198] ALICE Collaboration. *ALICE* Technical Design Report of the Time of Flight System (TOF), CERN-LHCC-2000-012, 2000.

[199] ALICE Collaboration. Addendum to the Technical Design Report of the Time of Flight system (TOF), CERN-LHCC-2002-016, 2002.

[200] ALICE Collaboration. *ALICE* Technical Design Report: Detector for High Momentum PID, CERN-LHCC-98-19, 1998.

[201] ALICE Collaboration. *ALICE* Technical Design Report of the Photon Spectrometer (PHOS), CERN-LHCC-99-4, 1999.

[202] ALICE Collaboration. *ALICE* Technical Design Report of the Dimuon Forward Spectrometer, CERN-LHCC-99-22, 1999.

[203] ALICE Collaboration. Addendum to the *ALICE* Technical Design Report of the Dimuon Forward Spectrometer, CERN-LHCC-2000-046, 2000.

[204] ALICE Collaboration. *ALICE* Technical Design Report of the Photon Multiplicity Detector (PMD), CERN-LHCC-99-32, 1999.

[205] ALICE Collaboration. Addendum to the Technical Design Report of the Photon Multiplicity Detector (PMD), CERN-LHCC-2003-038, 2003.

[206] ALICE Collaboration. *ALICE* Technical Design Report on forward detectors: FMD, T0 and V0, CERN-LHCC-2004-025, 2004.

[207] M. Bondila et al. *ALICE* T0 detector. *IEEE Trans. Nucl. Sci.*, 52:1705–1711, 2005.

[208] ALICE Collaboration. *ALICE* Technical Design Rport of the Zero Degree Calorimeter (ZDC), CERN-LHCC-99-5, 1999.

[209] ALICE-USA Collaboration. A proposal to study relativistic heavy ion physiscs with the *ALICE* experiment at the *LHC*. 2002.

[210] W. W. M. Allison and J. H. Cobb. Relativistic charged particle identification by energy loss. *Ann. Rev. Nucl. Part. Sci.*, 30:253–298, 1980.

[211] R. Bramm. ALTRO and TPC performance of *ALICE*, Ph.D thesis, University of Frankfurt, see arXiv:physics/0501052.

[212] Y. Belikov, M. Ivanov, K. Safarik, and J. Bracinik. TPC tracking and particle identification in high-density environment. *ECONF*, C0303241:TULT011, 2003.

[213] *ALICE* off-line project. http://aliweb.cern.ch/offline.

[214] ROOT: An Object-Oriented Data Analysis Framework. http://root.cern.ch.

[215] Federico Carminati. *ALICE* Off-line: Talk given at the *ALICE* Clubs and Progress Reports. http://agenda.cern.ch/fullAgenda.php?ida=a042865.

[216] Xin-Nian Wang and Miklos Gyulassy. Hijing: A Monte Carlo model for multiple jet production in $p+p$, $p+A$ and $A+A$ collisions. *Phys. Rev.*, D44:3501–3516, 1991.

[217] Miklos Gyulassy and Xin-Nian Wang. Hijing 1.0: A Monte Carlo program for parton and particle production in high-energy hadronic and nuclear collisions. *Comput. Phys. Commun.*, 83:307, 1994.

[218] N. van Eijndhoven et al. The *ALICE* event generator pool. *ALICE* Internal Note ALICE/GEN 95-32, 1995.

[219] Open Standard Code And Routins. http://nt3.phys.columbia.edu/OSCAR.

[220] Hans-Uno Bengtsson and Torbjorn Sjostrand. The Lund Monte Carlo for hadronic processes: Pythia version 4.8. *Comput. Phys. Commun.*, 46:43, 1987.

[221] Torbjorn Sjostrand. High-energy physics event generation with Pythia 5.7 and Jetset 7.4. *Comput. Phys. Commun.*, 82:74–90, 1994.

[222] Torbjorn Sjostrand, Leif Lonnblad, and Stephen Mrenna. Pythia 6.2: Physics and manual. *hep-ph/0108264*, 2001.

[223] *ALICE* Technical Proposal for a Large Ion Collider Experiment at the *CERN LHC*, CERN-LHCC-95-71, 1995.

[224] M. Regler and R. Fruhwirth. Reconstruction of charged tracks. 1988. In *St. Croix 1988, Proceedings, Techniques and concepts of high-energy physics* 407-499.

[225] R. K. Bock, H. Grote, D. Notz, M. Regler, and (ed.) Regler, M. Data analysis techniques for high-energy physics experiments. *Camb. Monogr. Part. Phys. Nucl. Phys. Cosmol.*, 11:1–434, 2000.

[226] Are Strandlie. Adaptive methods for the reconstruction of charged tracks in a noisy environment. Ph.D thesis, University of Oslo, 2002.

[227] R. Kalman. A new approach to linear filtering and prediction problems. 1960. Trans. of the ASME-J. of Basic Engineering, March 1960, 35.

[228] R. Fruhwirth. Application of filter methods to the reconstruction of tracks and vertices in events of experimental high-energy physics. 1989. Wien Inst. Hochenergiephys. - HEPHY-PUB-88-516 (88, REC.JAN.89) 160p.

[229] P. Billoir and S. Qian. Simultaneous pattern recognition and track fitting by the Kalman filtering method. *Nucl. Instrum. Meth.*, A294:219–228, 1990.

[230] Rudolf Fruhwirth. Track fitting with long tailed noise: A Bayesian approach. *Comput. Phys. Commun.*, 85:189–199, 1995.

[231] R. Fruhwirth. Track fitting with non-Gaussian noise. *Comput. Phys. Commun.*, 100:1–16, 1997.

[232] W. Adam, R. Fruhwirth, A. Strandlie, and T. Todorov. Reconstruction of electrons with the Gaussian-sum filter in the CMS tracker at LHC˙ *ECONF*, C0303241:TULT009, 2003.

[233] A. Badala et al. Full 3d event-by-event vertex reconstruction in $ALICE$ by pixel layers. Alice Internal Note ALICE-INT-2001-26, 2001.

[234] A. Dainese and M. Masera. Reconstruction of the interaction vertex in pp collisions at LHC with $ALICE$. ALICE Internal Note ALICE-INT-2003-27, 2003.

[235] R. L. Gluckstern. Uncertainties in track momentum and direction, due to multiple scattering and measurement errors. *Nucl. Instrum. Meth.*, 24:381–389, 1963.

[236] A. Strandlie, J. Wroldsen, and R. Fruhwirth. Treatment of multiple scattering with the generalized Riemann sphere track fit. *Nucl. Instrum. Meth.*, A488:332–341, 2002.

[237] A. Strandlie and R. Fruhwirth. Error analysis of the track fit on the Riemann sphere. *Nucl. Instrum. Meth.*, A480:734–740, 2002.

[238] A. Pulvirenti et al. Neural tracking in $ALICE$ high transverse momentum pattern recognition in the ITS stand alone. ALICE Internal Note ALICE-INT-2002-12, 2002.

[239] G. Chabratova et al. Development of the Kalman filter for tracking in the forward muon spectrometer of $ALICE$, ALICE Internal Note ALICE-INT-2003-002, 2003.

[240] R. Brun, F. Bruyant, M. Maire, A. C. McPherson, and P. Zanarini. Geant3. 1984. CERN-DD/EE/84-1.

[241] S. Agostinelli et al. Geant4: A simulation toolkit. *Nucl. Instrum. Meth.*, A506:250–303, 2003.

[242] M. Ivanov. *ALICE* Internal Note ALICE-INT-2005-036, in preparation.

[243] Joram Christian. Particle detectors. *CERN Summer Student Lectures 2002.* http://joram.home.cern.ch/Joram/lectures.htm.

[244] Pierre Astier et al. Kalman filter track fits and track breakpoint analysis. *Nucl. Instrum. Meth.*, A450:138–154, 2000.

[245] Andreas Morsch. http://morsch.home.cern.ch/morsch/generator.html.

[246] S. Voloshin and Y. Zhang. Flow study in relativistic nuclear collisions by fourier expansion of azimuthal particle distributions. *Z. Phys.*, C70:665–672, 1996.

[247] Virgil L. Highland. Some practical remarks on multiple scattering. *Nucl. Instr. Meth.*, 129:497, 1975.

[248] (Ed.) Bock, R. K., (Ed.) Bos, K., (Ed.) Brandt, S., (Ed.) Myrheim, J., and (Ed.) Regler, M. Formulae and methods in experimental data evaluation with emphasis on high-energy physics. vol. 1: General glossary, glossary group theory. 1984. Petit Lancy, Switzerland: Eps (1984) 312p.

Acknowledgements

This thesis would have never been written without the sustained effort invested over years by so many people who tried real hard to persuade me that swimming against the stream is not always a bright idea. They could have given up, yet they never did. A heartfelt thank you to Marek and Karel who made it a mission to see this thesis written.

I wish to express my gratitude to Prof. Vesa Ruuskanen for his support and his inspiring warm humanity paired with a great intellectual insight. He is someone I look up to not only on scientific level but also as a person. I am greatly indebted to Dr. Wladek Trzaska for his warm friendship and constant encouragement, for putting up, for all the years I spent in Jyväskylä, with my unorthodox views and my reluctance to wrap some of the work I have done into a thesis. Jan's Rak energy, enthusiasm and passion for physics and life has brought freshness and more life to this place. His professionalism, advices and help with the manuscript are greatly appreciated. Many thanks to Kari Eskola who gave me the opportunity of a great experience.

It is a pleasure to thank Dr. Kenneth Österberg and Dr. Marek Kowalski for their useful suggestions that improved this write-up and taught me valuable things.

I would like to thank the staff of the Physics Department, Marjut, Soili and Anna-Liisa in particular, for their friendly help over years.

Many friends accompanied me during years. They made my life richer and I feel priviledged to have met them: Yuri, Teddy, Dobrin, Karel, Marek, Marian, Andreas, Federico, Richard, Sorina, Paolo, Serghei who is like a brother to me, Liuda, Volodja, Vera, Kostea, Shadyar, Laila, Antoaneta, Flavio, Victoria, Piero, Grigori, Maxim, Galina, Sasha and Tonya Belkov, Dana, Rodica, Dana, Brigitte and Nino.

Above all, I thank my family who loves me for who I am. The love and hard work of my parents allowed me to pursue my dreams. My sisters and brothers, Rodica and the other members of my extended family have always been my road companions, encouraged and stood by me. A special thought to my father who showed me the way and taught me all the important things I need to know.